FACULTY OF ENGINEERING AND APPLIED SCIENCE
DEPARTMENT OF ELECTRONICS AND COMPUTER SCIENCE

MICROFLUIDIC DEVICES FOR INTEGRATED BIO/CHEMICAL SYSTEMS

by

Christian Georg Johann Schabmüller

A thesis submitted for the degree of

Doctor of Philosophy

University of Southampton

September 2001

UNIVERSITY OF SOUTHAMPTON

ABSTRACT

FACULTY OF ENGINEERING AND APPLIED SCIENCE

DEPARTMENT OF ELECTRONICS AND COMPUTER SCIENCE

Doctor of Philosophy

MICROFLUIDIC DEVICES FOR INTEGRATED BIO/CHEMICAL SYSTEMS

by *Christian Georg Johann Schabmüller*

Microsystems technology has become an established field with a rapidly increasing number of commercially available products. Most of the applications are in the automotive, the biomedical/pharmaceutical and the information technology industries. Furthermore, microsystems technology is of great interest for specialised areas in which its advantages justify the high costs incurred for development and fabrication for a small number of devices.

This project contributes to the area of microfluidics and BioMEMS (Micro-Electro-Mechanical-Systems) by developing and improving discrete fluidic devices, realising an interconnection method to obtain entire microfluidic systems and by combining microfluidics with BioMEMS.

Bubbles severely degrade most micropumps and gases cannot be pumped at all in many cases. A novel self-aligning micropump, which is able to pump gas and liquid was developed. It is also tolerant to gas bubbles of up to three times the pump chamber volume. The pump rate for ethanol is 1500 µl/min with a maximum backpressure of 1000 Pa and the pump rate for air is 700 µl/min.

To realise fluidic systems a flow sensor measuring and controlling the output of the micropump was most desirable. Technical problems experienced with a previous attempt are specified and solutions for obtaining a working flow sensor are presented. Initial experiments for water are described where flow rates of up to 30 µl/min were measured.

With the novel approach of a microfluidic circuitboard the aspect of interconnection by adapting the principle of the printed electrical circuitboard has been addressed. The concept has been proven functional with tests comprising a micropump and by a system consisting of various devices.

A system combining biotechnology with microfluidics results in a micromachined chip for the polymerase chain reaction (PCR). Integrated aspects of this device are incorporated heaters, temperature sensors and novel optical detection approaches. Optical fibres and pn-diodes have been included in the design for light input and fluorescent detection rendering the system immune from ambient light and eliminating the need for bulk optical components. Experiments show that the water filled chip with 1 µl volume can be cycled 30 times stepping through three temperature levels in 2.2 min. This makes it the smallest and fastest silicon micromachined PCR chip presented so far. Furthermore, this device could be used in connection with a system formed by the earlier described micromachined devices realised on the fluidic circuitboard, e.g. mixing the various chemicals for the PCR.

Acknowledgements

I would like to thank my supervisor Prof. Alan G. R. Evans for his support and understanding throughout the last years, for the opportunity to study for the PhD and for the possibility to attend so many conferences.

Special thanks to Dr. Michael Koch for getting me started, for his continuous support and interest of the project and mostly for his friendship.

Many thanks to the academic staff for the professional but friendly environment, especially to Dr. Arthur Brunnschweiler for his advice throughout the project. Thanks to Prof. James Wilkinson for the co-operation for some of the work and for his advice after the Mini-thesis and to Prof. Peter Ashburn for the interchange of ideas about football.

Thanks to Dr. Graham Ensell for his advice and proof reading of this thesis, which was invaluable and greatly appreciated, but most of all for his friendship. Furthermore, it was a great honour for me to play sometimes for his glorious football team 'Aged and Infirm'. Who says English and Germans cannot play football together?

My gratitude to Michele and Paul Routley for their friendship. Not to forget Paul's ability to fix my computer and to be really quick with fabricating my lithography masks. I am very happy for both of you and good luck in Cambridge (or wherever you might end up).

Special thanks to my 'landlady' Audrey Ashford-Smith, who gave me shelter and looked after me during the last months of this thesis.

I really appreciated the atmosphere at work to which my fellow PhD students Trevor Niblock, Dominik Kunz, Luca 'broken leg' Plattner, Mir Mokhtari, Ruth Houlihan, Majd Zoorob, Becky Neal, Mircea Gindila, Khairil Osman, Minqiang Bu, Huda El-Mubarek, Jim Benson, Ketan Mistry, Stefanos Stefanou, Nele D'Halleweyen, Urs Straube, Naiara Elejalde and some of the older ones such as Dr. Jochen Schiz, Dr. Martin Charlton, Dr. Yue Tang, Dr. Iain Anteney, Dr. Sam Rottich and Craig Easson greatly contributed and also the secretaries Glenys Howe, Jilly Searle and Lucia Hewett.

A special mention goes to Harald 'Harry fahr den Wagen vor' Sehr for his friendship, for the 'Bavarian-talk' in our office corner, for the company at some of the conference trips and for letting me watch the F1 races on his telly.

There are many people from the Microelctronics cleanroom who helped along the way, especially Brian Ault and Tony Blackburn, who were always up for a laugh and for good advice. Richard Bayly for his evaporations, sawings and wire bonds, which were always preceded by some sort of comment such as – 'aah, not you again'. It was quite funny once you got to know him. Also thanks to Jean Humphry, Corry Kratochvila, Mike Josey, Dr. Nasser Afshar, Paul Marchese, Elaine Bayly, Naomi Townsend, Angela MacManus and the 'men from the back', Alan Purdy, Alan Walker, Ted Meech, Dave Dawkins, John Amy and Pinder Sant. Not to forget Ken Frampton and his team from the mechanical workshop and Robert 'hot oven' Lambert.

Thanks also to Dr. Michael Kraft, Dr. Stephan Weiss and Dr. Steve 'football' Beeby for their friendship and advice, to Dr. Martin Lee and Dr. Dario Leslie from DERA Porton Down (now DSTL) for initiating the PCR chip project and the teaching of molecular biology, and to Jonathan Pollard for his excellent work during his final year project.

I very much enjoyed working with all of you guys and I tried not to forget anyone. But if I did, it was either on purpose or by accident – the choice is yours.

Finally, very special thanks to my parents and to my sister and her family for their continuous support and friendship. It is greatly appreciated! *Spezieller Dank geht an meine Eltern und an meine Schwester mit Familie für ihre stetige Unterstützung und ihre Freundschaft. Ich stehe in euerer Schuld!*

Contents

List of Figures

List of Tables

List of Symbols and Terms

Symbol	Unit	Explanation
α	[°]	taper angle of valve cone
α	[K^{-1}]	temperature coefficient
X_{GC}, X_{GE}	[-]	dimensionless head loss factor for gradual contraction and gradual expansion
X_{SC}, X_{SE}	[-]	dimensionless head loss factor for sudden contraction and sudden expansion
δ_{max}	[m]	maximum deflection at centre of pump membrane
δ_U	[m^3 V^{-1}]	coefficient for maximum volume displacement of a membrane for a given voltage
Δp_{diff}	[Pa]	pressure difference between inlet and outlet for diffuser
Δp_{nozzle}	[Pa]	pressure difference between inlet and outlet for nozzle
ε	[-]	compression ratio
Φ_V	[m^3 s^{-1}]	flow rate
γ_p	[m^3 Pa^{-1}]	coefficient for maximum volume displacement of a membrane for a given pressure
η	[-]	quantum efficiency
κ	[m^{-1}]	second derivative of deflection
κ_f	[W m^{-1} K^{-1}]	fluid thermal conductivity
λ	[m]	wavelength of light
μ	[Pa s]	dynamic viscosity
ν	[s^{-1}]	photon frequency
θ	[K W^{-1}]	thermal resistance
ρ	[kg m^{-3}]	density of material
ρ_r	[Ohm m]	specific electrical resistance
τ	[s]	time constant
A	[m^2]	area
c	[J kg^{-1} K^{-1}]	specific heat capacity
C_{fr}	[-]	friction coefficient

C_s	[m^{-2}]	ions impinging on unit area of surface
C_{th}	[W s K-1]	thermal capacitance
D_0	[m]	smaller diameter of valve cone
d_{31}	[C N^{-1}]	piezoelectric coefficient
D_h	[m]	hydraulic diameter
E_{el}	[V m^{-1}]	electrical field
E_s, E_p	[Pa]	Young's modulus of silicon or PZT
f	[Hz]	frequency
h_p	[m]	height of PZT
h_s	[m]	height of silicon
I	[m^4]	second moment of cross sectional area
I_p	[A]	photogenerated current
k	[W m^{-1} K^{-1}]	thermal conductivity
L	[m]	length
l, b, d	[m]	length, width and thickness of electrode
L_m	[m]	length of shorter side of membrane
l_y	[m]	width of flow sensor bridge
l_z	[m]	distance from bridge to channel wall
M	[N m]	bending moment
N	[m^{-3}]	doping concentration
p	[Pa]	pressure
P	[W]	power
p_{inlet}	[Pa]	pressure at valve inlet
P_{opt}	[W]	optical power
p_{outlet}	[Pa]	pressure at valve outlet
Q	[m^3 s^{-1}]	volume flow
R	[Ohm]	resistance
R_e	[-]	Reynold's number
R_p	[m]	projected ion range
s	[m]	distance of PZT layer to fixed end of silicon membrane
S	[A W^{-1}]	sensitivity of photodiode
t	[s]	time
T	[degC]	temperature
U	[V]	voltage
V	[m^3]	volume
v	[m s^{-1}]	velocity
x	[m]	distance

CHAPTER 1

Introduction

Research into silicon micromachining started in the 1960's when researchers realised that silicon could be used to fabricate not only discrete and integrated electronic circuits, but also transducers and other devices with new properties due to the materials used and their miniature size. The resulting devices are often referred to as MEMS, for micro-electro-mechanical-systems, although the term is misleading since many micromachined devices are not mechanical in any sense.

The first micromachined devices were pressure sensors [Tuft62]. The palette of MEMS devices nowadays is rather large including applications in micromechanics, microoptics (MOEMS: microoptical-electromechanical systems), microfluidics, biology (BioMEMS), chemistry and aerospace, to name but a few. However, integration is not as far advanced. Owing to the diversification of microtechnology, no standard libraries as in microelectronics have been created so far.

MEMS is now an established field and more and more commercially available products can be seen on the market. The main drives for the developments and commercialisation of micromachined products are the automotive, the biomedical/pharmaceutical and the information technology industries. In new car models many a micromachined sensor is incorporated in the engine compartment and for safety issues. The best-known sensor in a car is the accelerometer used in the airbag system, often a suspended mass with piezoresistive readout.

Drug development, DNA analysis and many other applications with numerous advantages such as speed, safety and the use of fewer chemicals have awoken the interest and the money from the biomedical and pharmaceutical industries.

Within the information technology industry the need for optical switching led to great research interest, where the main focus at present seems to be on movable micromirrors. Nevertheless, there are many other research areas such as microlenses, waveguides, etc.

Also the entertainment industry is becoming increasingly interested in cheap, mass-producible micromachined devices, where one of the keywords is virtual reality, with accelerometers and gyroscopes determining positions for playing games in the third dimension.

However, MEMS technology is as well of great interest for specialised areas where the advantages far exceed the high costs for development and fabrication. Such advantages are low power consumption, fewer reagents for chemical analysis and lower mass. This is especially true where lifetime, size and weight play an important role as it would be the case in aerospace or in long-term data collection, e.g. in oceanography, where devices are sealed in pressure compartments and left, inaccessible for a long periods of time in the open water.

The research in microfluidics started in the late 1970's. At Stanford University the research involved a gas chromatograph [Terr79], and at IBM ink jet printer nozzles were developed [Bass77, Pete79]. The follow-up on these early devices has been modest for a long time, but within the last 10 years a dramatic increase in research activities has taken place, and microfluidics has developed into a very interesting research topic with many an application.

Scientists miniaturised devices known from the 'macro' world, e.g. pumps, valves, chromatographs, particle counters and sorters, filters, reaction chambers and many more. However, apart from ink jet nozzles there were very few commercially available microfluidic products.

Only in recent years have many companies become interested in commercialising devices, mainly in the BioMEMS area. A keyword in the field is 'lab on a chip' or 'μTAS' (micro total analysis systems), where macroscopic analysis methods are being miniaturised. DNA analysis is one of the strongest fields in the BioMEMS area. It comprises the polymerase chain reaction (PCR) for the DNA amplification, DNA size analysis and DNA sequencing.

Whereas in the early years articles dealing with microfluidics published in conference proceedings and journals were only few, now entire conferences are dedicated to this topic, e.g. μTAS, BioMEMS, and leading MEMS journals have their own microfluidic sections, e.g. Sensors and Actuators B.

Although, as the above mentioned keywords 'lab on a chip' and 'μTAS' would suggest, complete microfluidic systems are still rare and very specific in their application, most of the developed devices are discrete.

To realise versatile microfluidic systems, some 'basic' components like pumps and flow sensors are necessary. Furthermore, in accordance to the printed circuitboard used in electronics, a similar approach for fluidic devices is desirable. Such a microfluidic circuitboard should allow discrete fluidic devices to be mounted in various and independent configurations forming complete systems.

To this 'basic' system, specific components can be added, e.g. a mixing/reacting chamber or a PCR chip, to form new and more complex integrated systems. During the development of the devices it is important to keep the focus on the integrated aspect, which means that the discrete components could have heaters, temperature sensors, optical readouts, etc.

In previous years, the Micorelectronics group at Southampton University has developed some discrete microfluidic devices. However, integration did not take place. To enhance and continue this work, devices have been used, improved and newly developed. Although, the devices have been characterised on their own, all of them were designed under the previously mentioned criteria of integration. Therefore, the aims of the work can be highlighted as:

- developing a microfluidic pump for liquids and gases
- developing a microfluidic flow sensor
- finding a method of interconnecting different fluidic devices
- assemble and characterise a fluidic system
- developing a micro PCR chip – biotechnology combined with microfluidics

At the beginning of this thesis an overview of microsystem technology, microfluidcs and BioMEMS is given with the focus on devices forming parts of the thesis and on integrated systems described in the literature.

In chapter three, a novel self-aligning micropump, which is able to pump gas and liquid is described. It is also tolerant to gas bubbles of up to three times the pump chamber volume. Chapter four explains the improvement of a micromachined flow sensor. Technical problems experienced with the previous fabrication are described and solutions for obtaining a working flow sensor are presented.

The aspect of integration and interconnection by adapting the principle of the printed electrical circuitboard is addressed in chapter five. The novel approach towards an integrated microfluidic system is given with an example of a chemical reaction system consisting of two pumps, two flow sensors and a micromixer/-reactor realised on the new microfluidic circuitboard.

A system combining biotechnology with microfluidics results in a micromachined chip for the polymerase chain reaction (PCR), which is explained in chapter six. This chip is intended to be used to amplify DNA. Integrated aspects of this device are incorporated heaters, temperature sensors and novel optical detection approaches. Furthermore, this device could be used in connection with a system formed by the earlier described micromachined devices realised on the fluidic circuitboard, e.g. mixing the various chemicals for the PCR.

The thesis concludes with a discussion on results and performances of the devices and systems and gives an outlook towards future developments.

CHAPTER 2

Microfluidics and BioMEMS – A Review

2.1 Introduction to MEMS- Micro Electro Mechanical Systems

The area of MEMS – micro electro mechanical systems or, as named in Europe, MST – micro system technology, is an established field similar to microelectronics, although the turnover in microelectronics is still significantly higher than in the MST field. According to a study by the System Planning Corporation the market forecast for the year 2000 was a total of 13.9 B$ for MEMS products, whereas for comparison the world semiconductor market in 1996 was already 144 B$ [Lang99].

Several books have been published explaining the processes and technologies used in micromachining and giving numerous examples of the many devices realised to date [Koch00, Malu00, Kova98, Elwe98, Menz97, Buet94]. In figure 2.1, the basic principle of patterning a wafer, which is employed in the vast majority of micromachining processes, is depicted. A photoresist layer is spun on and soft-baked (figure 2.1a) and then exposed to ultraviolet light through a mask, normally a quartz plate with patterned chromium (figure 2.1b). The exposed photoresist (positive resist shown) is then dissolved in a developer solution, leaving only the non-exposed regions behind and then hard-baked (figure 2.1c). Now using the photoresist as a mask, the wafer can be patterned by a dry or wet etching method (figure 2.1d).

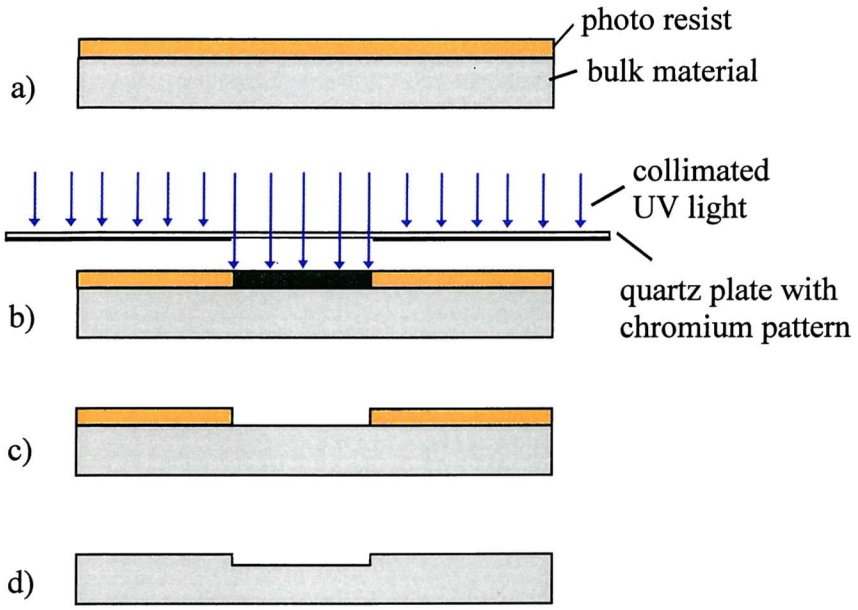

Figure 2.1: Schematic of a basic photolithography and etch process.

Many processes are used to create micromachined devices, most of which are derived from microelectronics fabrication. However, as micromachining has grown in popularity, several specific processes have been developed. Silicon is still the substrate material used most often due to the large variety of standard processes available and because of its outstanding material properties. It has a Young's modulus, hardness and tensile yield strength that approach those of many commonly used metals such as stainless steel (table 2.1). However, other materials have entered the MEMS area. Glasses like pyrex, quartz and borosilicate are used. They are especially popular in the BioMEMS field because of their transparency and electrical insulation properties, e.g. high voltages applied in capillary electophoresis or a large variety of surface modifications are possible [Baba99]. Such surface modifications are for example immobilisation layers made of antibodies to catch cells or immobilised single stranded DNA fragments to catch DNA fragments with complementary sequence out of solution. Transparency is a very useful property for fluorescent detection methods, e.g. labelling of DNA with fluorescein or rhodamine B [Manz97].

Other devices are based on polymers as described by Schomburg [Scho94], Urban [Urba99], Rong [Rong99], Barker [Bark00], Ekstrand [Ekst00] and Boone [Boon00] or made by electroplated metal [Doep97]. Gallium-Arsenide (GaAs) is often used in micro optics but only a few micromachined devices have been created in it [Buri98, Lali00]. One reference to germanium was found. This was used as a substrate in the creation of a micromachined pressure sensor, a thermistor and a capacitive microphone [Li99].

Material	Yield Strength (10^9 N/m^2)	Knoop Hardness (kg/mm^2)	Young's Modulus (GPa) (110)	Density (g/cm^3)	Thermal Conductivity (W/cm·K)	Thermal Expansion Coefficient (10^6/K)
Silicon	7	850	190	2.3	1.57	2.33
Stainless Steel	2.1	660	200	7.9	0.329	17.3

Table 2.1: Mechanical properties of silicon and stainless steel. From [Kova98].

The two major types of processing are subtractive, e.g. etching, laser machining or milling and additive, e.g. deposition of dielectrics or metals. Table 2.2 gives an overview of processes and lists examples used for MEMS microfabrication. The list does not claim to be exhaustive as new processes are continually being developed.

Process Type	Example
common (from microelectronics fabrication)	
lithography	photolithography, electron-beam lithography, ion-lithography
thin-film deposition	chemical vapour deposition (CVD), plasma-enhanced chemical vapour deposition (PECVD), epitaxy, sputtering, evaporation, pulsed laser deposition
etching	plasma etching, reactive-ion etching (RIE), wet chemical etching, laser-assisted chemical etching (LACE)
annealing	thermal annealing, laser annealing
implantation	ion implantation
MEMS specific	
lithography	x-ray lithography, liquid-phase photopolymerisation
thick-film deposition	screen printing, spin-on application, electroplating
etching	wet bulk etching, deep reactive ion etching (DRIE), electrochemical etching
machining	drilling, milling, electric discharge machining (EMD), diamond turning, sawing, powder blasting
bonding	fusion bonding, anodic bonding, eutectic bonding
surface modification	wet chemical modification, plasma modification

Table 2.2: Example processes used in micromachining.

In most cases MEMS fabrication falls into one of two categories, bulk or surface micromachining. In figure 2.2 the difference between the two is depicted. In bulk micromachining, part of the 'bulk' substrate is removed, i.e. large pits or holes are formed in the front or back of the wafer. Whereas surface micromachining is processing above the

substrate, i.e. the substrate is mainly used as a base to build upon. It often involves the removal of a sacrificial layer to create free standing structures.

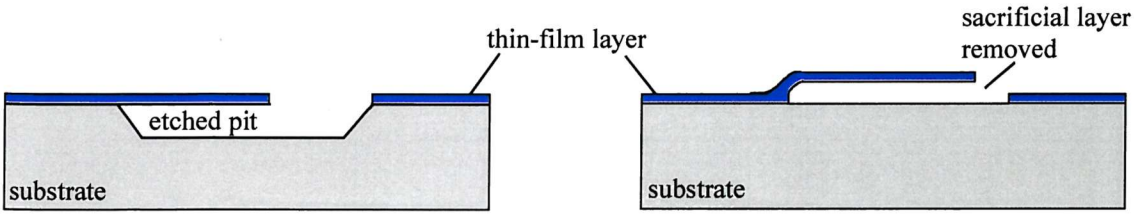

Figure 2.2: Schematic of bulk (left) and surface (right) micromachining.

2.2 Microfluidics and BioMEMS

Micromachining has numerous applications in fluidics, and its use in this area has become even more important as people strive to create complete fluidic systems in miniaturised formats. A broad variety of materials are available for fabricating the systems or their components, including glasses, plastics/polymers, metals, ceramics and semiconductors. Thus techniques currently exist for generating a wide variety of structures and functions, and system concepts are evolving.

The number and variety of microfluidic devices is so extensive, that only devices and concepts relevant to this thesis are reviewed. A broad range of devices and systems can be found in the recently published books 'Micromachined Transducers Sourcebook' [Kova98] and 'Microfluidic Technology and Applications' [Koch00] and in various review articles published [Dari00, Harr99, Abra99, Shoj94, Grav93].

2.2.1 Gas/Liquid Micropumps

To date, a large number of reports on micropumps have been published with many different actuation principles, such as electrostatic [Zeng94, Zeng95], shape memory alloy [Bena97], thermopneumatic [Gros99, Scho94], piezoelectric [Koch98a, Koch98b, Olss95], pneumatic [Zeng94], bimetallic [Zhan96], electromagnetic [Gong99] and peristaltic [Veen00, Gros99]. Usually, the pumps are mechanical and of the membrane type. Alternative actuation principles are electrohydrodynamic [Rich91a, Bart90], electroosmotic [Guen99, Jaco94, Manz91], magnetohydrodynamic [Lemo00, Lemo99], ultrasonic [Blac99], electrochemical [Boeh99a] or by using micro gears [Doep97, Dewa97].

A detailed description of the different principles can be found in 'Microfluidics Technology and Applications' [Koch00]. However, only a few of the micropumps published until now are suitable for pumping gas or are self-priming. Nevertheless, these issues are very important as gas bubbles severely deteriorate the performance of most pumps. The main difference in pumping gases compared to liquids is that to create the necessary pressures, the fluid has to

be compressed. Hence, the membrane micropump must secure a certain compression ratio, i.e., volume displacement induced by the membrane over mean pump chamber volume.

Two very similar attempts at fabricating a piezoelectrically driven gas/liquid micropump realised in silicon have been made by Gerlach [Gerl97] and Linnemann [Linn98]. One approach uses passive dynamic valves, the other passive cantilever valves (figure 2.3). In both cases, the silicon membrane wafer is micromachined so that the pump chamber volume is minimised. Both designs were able to pump air in the low ml/min range. Liquid pumping and tolerance towards gas bubbles has also been presented by Linnemann, with very high backpressures for liquid (100 kPa) and gas (60 kPa). Both pumps are unsuitable for mass production as the PZT needs to be manually glued on each pump, which can lead also to differences in performance due to miss-alignment or glue thickness variation.

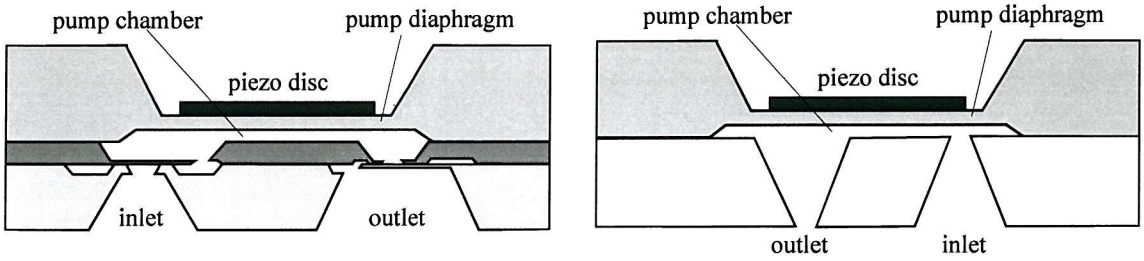

Figure 2.3: Schematic of silicon micromachined gas/liquid micropumps;
left: [Linn98], right: [Gerl97].

Another piezoelectrically driven silicon/plastic pump named VAMP (Valve And Micro Pump) has been presented by [Steh96]. It can be used either as an active microvalve or as a forward and reverse working micropump. The layout of the device can be seen in figure 2.4a. The VAMP consists of a base plate containing two fluid ports, a diaphragm fabricated by micromachining silicon, and a piezo actuator driving the diaphragm. By applying a DC-voltage, the device operates in the valve mode and by applying a square wave voltage, the device operates in the pump mode. The direction of fluid transport can be changed by the driving frequency due to a dynamic effect of fluid oscillation in the tubing. The pump had a maximum water pump rate of 1.6 ml/min in forward direction (200 V, 190 Hz) with a maximum backpressure of 17 kPa and a pump rate of 1.2 ml/min in reverse direction (200 V, -). The air pump rate was 8 ml/min in both directions (100 V, 1650 Hz forward, 1150 Hz backward), but no backpressure has been measured.

Boehm [Boeh99b] (figure 2.4b) and Kaemper [Kaem98] (figure 2.4c) used injection moulding of polymers for the creation of their micropumps. Both can be actuated piezoelectrically and in addition Boehm developed an electromagnetic actuator consisting of a magnet placed in a coil on top of the membrane. In both cases the pump membrane and the passive valve membranes were also made from thin polymers by injection moulding. The mould for Boehm's pump is made of aluminium by conventional workshop equipment. Kaemper

used a mould made by LIGA technology and the through holes in the plastic parts were drilled by a Nd:YAG laser. Kaemper achieved a water pump rate of 400 µl/min with a very high backpressure of 210 kPa and air pumping with a rate of 3.5 ml/min and high backpressure of 50 kPa. The pump by Boehm had a water pump rate for both actuation types of around 2 ml/min with a maximum backpressure of around 10 kPa. An air pump rate was only given for the electromagnetically actuated membrane, which was 40 ml/min.

In contrast to that, Rapp [Rapp94] developed a LIGA based micropump covered by a glass plate (figure 2.4d). The titanium membrane is actuated by an external pneumatic drive. The passive valves are made of polyimide sitting on the titanium membrane. Due to the different stiffness in the materials the polyimide bends more under pressure than the titanium and therefore the valve opens. The same principle is true for closing the valve. The membrane pump had a pump rate for air of 86 µl/min with a maximum backpressure of 4.7 kPa. No liquid pump rate or backpressure has been given. The pump was assembled out of many parts, which would make mass fabrication not attractive.

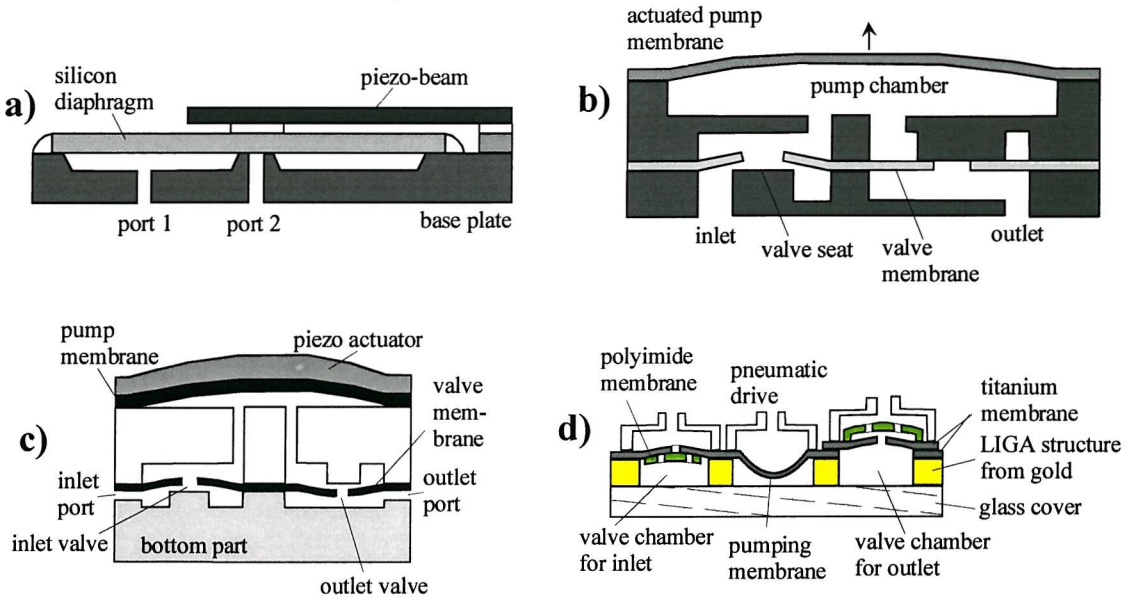

Figure 2.4: Schematic of micromachined pumps;
a) [Steh96], b) [Boeh99b], c) [Kaem98], d) [Rapp94].

A rather different pump principle has been published by Doepper [Doep97]. He used LIGA fabricated nickel-iron gear wheels driven externally by electromagnetic stepping motors (figure 2.5a). This technique allowed him to pump even high viscosity fluids such as oil. Another gear pump has been presented by Dewa [Dewa97]. The magnetically actuated two-gear plastic pump was formed by LIGA processing. One of the gears, the driving gear, has a central permalloy bar (Ni/Fe). The magnetic drive mechanism was fabricated in carbon steel to which the permanent magnets were bonded. The outside diameter of the pump is 3.2 mm, including the two 24 tooth gears, each gear with a diameter of 1.4 mm. Both gear pumps are self-filling

and bubble tolerant, but no gas pump rates were given. Doepper stated a maximum backpressure for air of 2.5 kPa.

A self-priming and bubble-tolerant peristaltic micropump has been presented by Veenstra [Veen00]. The device was created by powder jet micromachining a silicon base wafer and the anodic bonding of a pyrex membrane wafer with glued on piezo discs (figure 2.5b). This semi-silicon pump could sustain a high backpressure of 50 kPa (ethanol), however, the pump rate of 9 µl/min (ethanol) was very small. Measurement results for pumping air have not been presented.

The above described gas/liquid micropumps are listed in table 2.3.

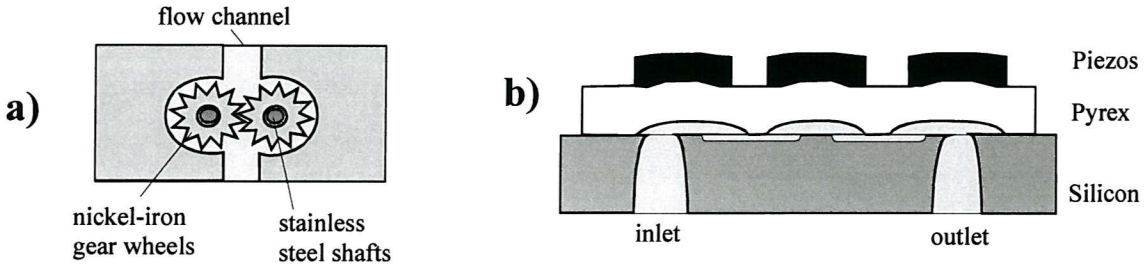

Figure 2.5: Schematic of a) gear-wheel pump [Doep97], [Dewa97] and b) peristaltic micropump [Veen00].

Author	pump mechanism; valve type	max. pump rate liquid; gas	max. backpressure liquid; gas	chip size [mm^3] self-filling
Rapp 1994	pneumatic (ext.) titanium membrane; passive polyimide membrane	- air: 86 µl/min at 50 kPa, 5 Hz	- air: 4.7 kPa at 50 kPa, 5 Hz	pump membrane diameter 5 mm yes
Stehr 1996	piezo silicon membrane; passive dynamic	water: 1.6 ml/min at 200 V, 190 Hz; air: 8 ml/min at 100 V, 1.15/1.65 kHz	water: 17 kPa -	- yes
Doepper 1997	electromagnetic motor (ext.) gear wheels; -	oil: 1 ml/min water: 55 µl/min at 296 rpm; air: -	oil: 120 kPa water: 7 kPa air: 2.5 kPa	10 x 10 x 30 yes
Gerlach 1997	piezo silicon membrane; passive dynamic	- air: 7.5 ml/min at 12 kHz	- air: 2.8 kPa at 12 kHz	membrane 11 x 11 mm^2 -
Dewa 1997	magnetic -	water: 350 µl/min at 5000 rpm; -	water: 13.7 kPa; -	∅ 3.2 mm yes
Kaemper 1998	piezo polycarbonate membrane; passive polycarbonate membrane	water: 400 µl/min, 70 Hz; air: 3.5 ml/min	water: 210 kPa, 70 Hz; air: 50 kPa	12 x 12 x 3.5 yes
Linnemann 1998	piezo silicon membrane; passive cantilever	water: 1.4 ml/min at 220 Hz, *; air: 3 ml/min at 220 Hz, *	water: 100 kPa at 220 Hz, *; air: 60 kPa at 220 Hz, *	7 x 7 x 1.1 yes
Boehm 1999 (b)	electromagnetic polymer membrane; passive polymer membrane	water: 2.1 ml/min at 100 mA, 50 Hz; air: 40 ml/min at 400 Hz	water: 10 kPa at 100 mA, 50 Hz; air: -	10 x 10 x 8 yes
Boehm 1999 (b)	piezo polymer membrane; passive polymer membrane	water: 2 ml/min at 350 V_{pp}, 50 Hz; air: -	water: 12.5 kPa at 350 V_{pp}, 50 Hz; air: -	12 x 12 x 2 yes
Veenstra 2000	piezo pyrex membrane; -	ethanol: 9 µl/min, >300 Hz; -	ethanol: 50 kPa -	- yes

(* asymmetrical rectangular signal from – 40 Volts to 120 Volts)
(ext. ≡ external, max. ≡ maximum)

Table 2.3: Gas/liquid micropumps published up to date.

Several materials for the creation of the pumps have been used. Silicon, silicon combined with plastic or pyrex, plastic or plated metal was used. Six out of the ten presented pumps were actuated piezoelectrically. PZT is a powerful and easy to apply actuator. Eight pumps used a membrane as the active moving part and two in-line gear wheel pumps were fabricated. This shows that for micromachined devices the membrane pump is easiest to realise.

The pump rate for air was below 8 ml/min where it was measured apart from the pump by Boehm, which had a pump rate of 40 ml/min for the electromagnetically actuated membrane. The pump rates for air as fluid were always higher for a given pump than the liquid pump rate. Very high backpressures for air were measured by Kaemper (50 kPa) and Linnemann (60 kPa). The rest of the measured backpressures for air were below 5 kPa.

The highest pump rate for liquid (water: 2 ml/min) was achieved by the pumps presented by Boehm and the lowest pump rate was measured by Veenstra (ethanol: 9 µl/min). The highest backpressure for liquid (water: 210 kPa) was measured by Kaemper, with the rest of the measured backpressures ranging between 7 kPa and 120 kPa.

All of the above listed pumps were self-priming. Therefore, even if no air pump rate was given for some of the pumps, they were still considered as being gas pumps. Some of the pumps are difficult to manufacture as for example LIGA technology uses synchrotron radiation for the lithography step, which is available only at very few specialised places in Europe. The plastic pumps were made by injection moulding. Those moulding machines are not present in most cleanrooms for microfabrication. Therefore, one has to choose to most appropriate pump for a given application and also the possibility of fabrication needs to be considered.

2.2.2 Micromachined Flow Sensors

Several principles of flow measurement using micromachined sensors have been described so far. In the following the various principles are listed and examples are given.

- Pressure difference: This flow sensing principle relies on the measurement of the differential pressure in a flowing liquid. Pressure sensors can be used to measure flow by sampling the pressure drop along a flow channel with known fluidic resistance, R_f, and calculating the flow from the fluidic equivalent to Ohm's law: $Q = \frac{\Delta p}{R_f}$. The sensor presented by Cho [Cho91] uses a fixed membrane with capacitive readout (figure 2.6a). The measurement window is between 0.001 and 4 Torr with a sensitivity of 200 ppm per mTorr. Capacitive Pressure sensors are also used by the device presented by Oosterbroek [Oost97, Oost99] (figure 2.6b). Flow rates between 0 and 270 µl/min have been measured with a capacitance change from 2.63 to 2.67 pF.

- Drag force (figure 2.6c): This type of flow sensor consists of a cantilever beam with an integrated strain gauge resistor. When the cantilever is immersed in a flowing fluid, a drag-

force is exerted on the beam resulting in a deflection of the cantilever, which can be detected by piezoresistive elements incorporated in the beam. The sensor from Gass [Gass93a] measures water flow rates of 5 to 500 µl/min at a sensitivity of 4.3 µV V^{-1}/µl min^{-1}. Other drag force based flow sensors have been presented by Nishimoto [Nish94] and Su [Su96].

- Electrohydrodynamic (figure 2.6d): The principle of such a sensor is the injection of charge at one electrode grid and the subsequent detection of a charge pulse at a second grid. This charge is carried along by the ionic species. The publications from Richter [Rich91a, Rich91b] state measured flow rates for DI water from 8 – 1700 µl/min and flow rates for ethanol from 8 – 50 µl/min.

- High-speed x-ray micro imaging: This technique uses high-speed x-ray micro imaging of the steady state flow in micro pipes [Leu97]. The setup for the measurement consists of a x-ray monochromator and a high frame rate CCD camera. Flow images of vortices are collected and the flow pattern is reconstructed with the help of a flow recovery algorithm.

- Lift force (figure 2.6e): The device presented by Svedin [Sved97] consists of a pair of bulk micromachined torsional airfoils, mounted at an angle in a flow channel. In operation, the torque on the upstream airfoil plate is greater than that on the downstream plate, and signals from piezoresistive strain gauges on each airfoil are measured. With this device a flow sensitivity of 7.4 µV/V/$(m/s)^2$ has been measured in both flow directions. The measured flow velocity range was between 0 and 7 m/s.

- Thermal flow (figure 2.6f): Most micro flow sensors described so far work in the thermal domain. Convection cools a heater and disturbs the temperature distribution close to the heater. There are three main flow sensing techniques:

  - Constant power mode: In the constant power mode, the temperature difference T2-T1 is measured for the flow. The device presented by Lammerink [Lamm93] measures water flow in the range 0 – 2 · 10^{-3} m s^{-1} and 0 – 60 µl/min. A very similar device has been presented by Kohl [Kohl94].
  - Constant temperature mode: The temperature of the heater is directly measured and kept constant. The electrical power needed to maintain a constant temperature is a measure of the flow. In this mode, the flow sensor is very fast. Stemme [Stem86] reported a flowsensor based on this principle with a measurement window of 0.8 – 30 m/s, a response time of 0.45 s and a sensitivity of 0.01 – 0.5 mW $(mW)^{-1}$/ m s^{-1}.
  - Time of flight mode [Elwe94]: The heater is continually pulsed with a certain amount of electrical energy. Downstream of the heater, a temperature sensor is used to measure the time delay between heat source and heat detection.

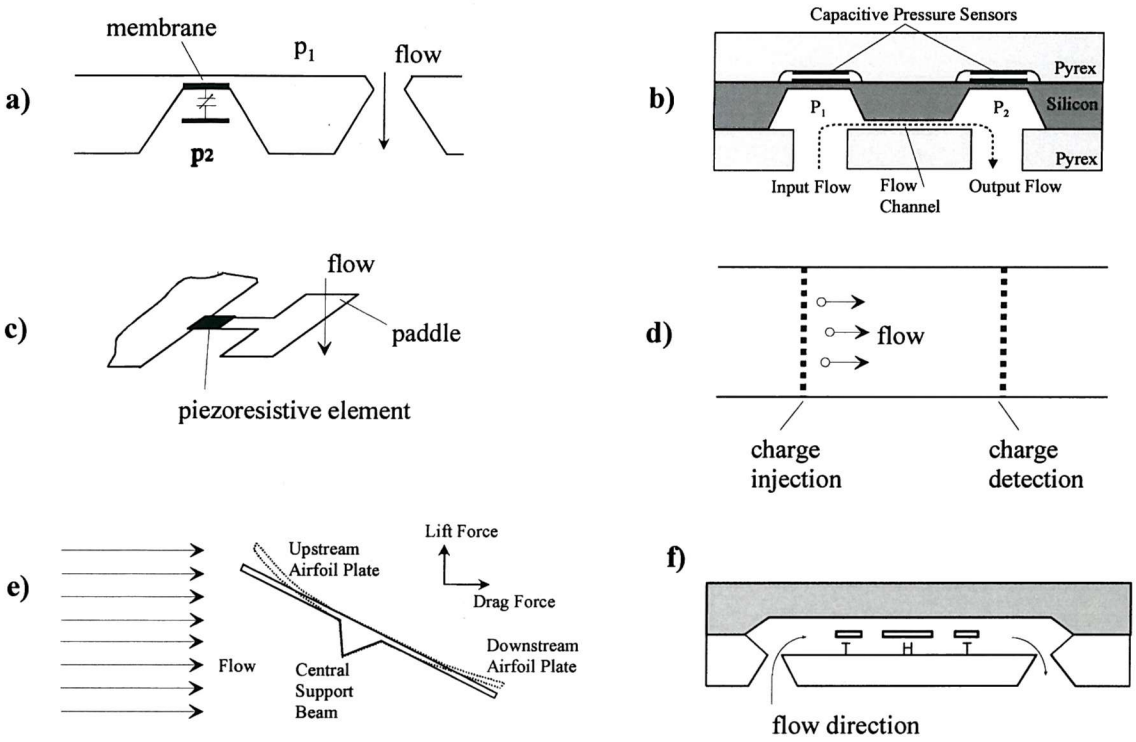

Figure 2.6: Different measurement principles for measuring fluid flow; a) and b) pressure difference, c) drag force, d) electrohydrodynamic, e) lift force and f) thermal.

2.2.3 Microchips for the Polymerase Chain Reaction (PCR)

As the reader might not be familiar with DNA amplification using PCR, a short introduction is given in Appendix A.

Several microchips for the polymerase chain reaction based on two distinct principles have been presented so far. In one principle, the PCR reaction is carried out in a chamber, which is heated and cooled in cycles (figure 2.7a). In the other principle, the PCR solution is led within a channel over three distinct temperature zones (figure 2.7b).

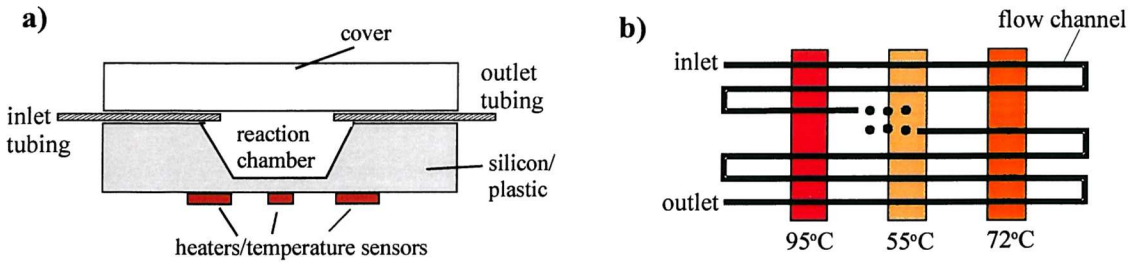

Figure 2.7: Principles of PCR-chips; a) reaction chamber, b) continuous flow.

2.2.3.1 Chamber PCR chips

The first micromachined PCR chip was presented by Northrup [Nort93] in 1993. It used a relatively large reagent volume of 25 – 50 µl and it needed the use of silicone adhesive for sealing the chambers. Polyethylene tubing was used for the inlet and outlet and the heaters were polysilicon on a nitride membrane underneath the reaction chamber. Another device developed by this group used two bonded silicon wafers with matching, anisotropically etched grooves to form a tunnel into which a plastic reaction tube was inserted [Wool96]. The plastic tube was heated via polysilicon resistors deposited onto the silicon. This setup was fixed on a glass board and connected to a capillary electrophoresis (CE) chip. Another PCR chip connected to capillary electrophoretic separation channels has been presented by Lagally [Laga00].

Poser [Pose97] proposed a silicon based PCR chip with very fast temperature rise and fall times. The chip was covered alternatively with a pyrex or silicon plate. The chip was heated by integrated thin film (NiCr, Pt) resistors and cooled by forced air (fan). The device comprises thermal insulation gaps and was connected to a copper heat sink. However, test series showed biocompatibility problems inhibiting the PCR by all materials used. Only covering the surfaces with polydimethylsiloxane (PDMS) led to successful DNA amplification.

Also very fast heating and cooling rates where achieved by Daniel [Dani98]. The silicon chip had integrated thin film heaters and was cooled via a heat sink. The reaction chamber was suspended on beams for thermal insulation. A significant disadvantage of this chip was the use of oil to seal the chamber, hence preventing evaporation of the PCR sample but also preventing the use of optical detection for evaluation purposes.

Other PCR chips have recently been presented by Kondo [Kond99], Lin [Lin00a, Lin00b], Lao [Lao00] and Nagai [Naga99], all based on the micromachining of silicon with glass covers. The PCR chambers by Nagai were arranged in an array. The smallest chambers had a capacity of 23 pl in a density of 10^4 chambers/cm^2. However, PCR was only successful in chambers whose volume was greater than 86 pl. Another array of 8 x 12 PCR wells was presented by Akahori [Akah00], but no DNA amplification has been performed.

Kellog [Kell00] and Eckersten [Ecke00] made PCR chambers on plastic compact discs, where the liquid was moved by rotating the disc. Around one hundred assays can be done in parallel.

Table 2.4 lists the different PCR-chips described above.

Author	chip size; chamber volume	temperature rise; temperature fall	DNA amplified; number of base pairs	total time; number of cycles	device material; power consumed
Northrup 1993	- 25 and 50 µl	resistive: 13 to 35 °C/sec; passive: 13 to 35 °C/sec	GAG gene of HIV virus; 142 bp	20 min; 20	silicon; 2.25 W
Northrup 1995	- -	resistive: 5 °C/sec; forced air: 2.5 °C/sec	β - globin; 268 bp	- 31	silicon; 1.2 W
Woolley 1996	tube: length 2 cm, ∅ 2 mm; 20 µl	resistive (ext.): 10 °C/sec; passive: 2.5 °C/sec	a) β - globin; 268 bp b) genomic Salmonella DNA; -	a) 15 min; 30 b) –; 35	poly-propylene tube; -
Poser 1997	20 mm x 18 mm; 5 – 10 µl	resistive: 80 °C/sec; forced air: 40 °C/sec	genomic yeast; 500 bp	- 30	silicon; 2.5 W
Daniel 1998	- 1.5 µl	resistive: 90 °C/sec; passive heat sink: 74 °C/sec	plasmid p-Bluescript; -	- 30	silicon; 2.0 W
Kondo 1999	30 mm x 16 mm; 30 µl	resistive: 20 °C/sec; passive: 2 °C/sec	λ DNA; 500 bp	35 min; 40 (two step)*	silicon; -
Nagai 1999	- 86 pl	- -	GFP gene; 200 bp	- 99 (two step)*	silicon; -
Lagally 2000	- 280 nl	external: - forced air: 10 °C/sec	- -	10 min; 20	glass; -
Lin 2000 (a)	32 mm x 32 mm; 50 µl	thermoelectric (ext.): 4 °C/sec; heat sink: 2.2 °C/sec	hepatitis C virus; 500 pb	30 min; 30	silicon; -
Lao 2000	18 mm x 12 mm; 8 µl	resistive: 5 °C/sec; - : 3.5 °C/sec	Fritillaria cirrhosa; 600 bp	- 35	silicon; 1.5 W
Kellogg 2000	- 25 µl	external: 2 °C/sec; heat sink : 2 °C/sec	Escherichia coli; -	- 35	plastics; -
Akahori 2000	- 1.4 µl	- -	- -	- -	silicon; -
Eckersten 2000	- 100 – 500 nl	- -	whole blood; 160 bp	7 min; 30	plastics; -
Yu 2000	- 1.5 µl	resistive (ext.): 2.4 °C/sec; thermoelectric: 2 °C/sec	Escherichia coli; 346 bp	- -	plastics; 0.12 W

(* only two temperature steps: 94 °C and 68 °C)

Table 2.4: Different chips for the polymerase chain reaction (PCR).

A number of PCR-chips for DNA amplification has been developed. The volume of the micro-chambers is below 50 µl, with three devices presented in the nano-litre range. The longest presented DNA amplified was 600 base pairs and the number of temperature cycles was with most devices 30 to 35.

A catchword for micromachined PCR chips is rapid temperature cycling and hence shortening the time for DNA amplification. Most of the presented heating and cooling rates are very small in the order of 2-5 degC/sec for heating and 2-4 degC/sec for cooling. Very fast heating and cooling of the reaction chamber has been only presented by Poser (heating: 80 degC/sec, cooling: 40 degC/sec) and Daniel (heating: 90 degC/sec, cooling: 74 degC/sec). The drawbacks of those devices are the large size of the chip presented by Poser (20 mm x 18 mm), which allows no high density of chips on a wafer during fabrication, and the non-compatibility of the chip by Daniel to optical detection of the reaction product. Optical detection of the DNA amplification products is a rapidly developing field and it is most advantageous to have an optical window within a PCR chip. An overview of optical detection methods for real-time quantitative PCR is given in Appendix B.

2.2.3.2 Continuous flow PCR chips

Instead of a micro-chamber, Kopp [Kopp98] and Koehler [Koeh98] employed capillaries on a glass or silicon chip, respectively, to construct a 'continuous flow PCR' device. Both showed that different DNA samples can be spatially separated by introducing a buffer solution or oil drops, respectively. Koehler did not carry out any specific DNA amplification, whereas Kopp amplified 176-base pair fragments from the DNA gyrase gene of Neisseria gonorrhoeae at different flow speeds ranging from 18.7 minutes to 90 seconds for 20 cycles. Results show that the fluorescent signals and hence the amount of amplified DNA is very weak at flow through times below 4 minutes. Table 2.5 summarises the data on the flow-through PCR-chips described. A potential problem with flow through devices is the contamination of the sample reaction with products of a previous reaction (product carryover) due to the capacity of the PCR to synthesise millions of DNA copies. For industrial applications single-shot PCR (chamber PCR chips) devices are still preferred.

Author	channel diameter	flow rate	DNA amplified; number base pairs	total time; number cycles	device material; power consumed
Koehler 1998	-	0.1 – 20 µl/min	-	- 16	silicon; 14.6 – 16.6 W
Kopp 1998	40 x 90 µm; 2.2 m long	5.8 – 72.9 nl/sec	DNA gyrase gene; 176 bp	90 sec – 18.7 min; 20	glass; 5 W

Table 2.5: Flow-through devices for the polymerase chain reaction (PCR).

2.2.4 Interconnects

Several types of interconnection for microfluidic devices have been published in the literature. This is an important part for the creation of microfluidic systems. In this section, the various types are described.

- vertical system integration: Here, different layers were mounted on top of each other as presented by van der Schoot [Scho93]. The layers were made of pyrex, silicon or plastic in which holes for the connections were drilled or etched.

- moulded connections: The demonstrator using this technique consisted of an epoxy printed circuit board containing the channels and through holes. This was attached to a transparent polycarbonate substrate and individual components were glued onto the PCB [Flui94, Lamm96].

- interlocking (figure 2.8): These Lego® like connectors use interlocking fins made by sawing silicon [Gonz98a, Gonz98b]. When two opposite sets of the structure are pushed into each other, the fingers on each structure tend to separate by a small distance to accommodate the insertion of the fins on the opposite structure. The friction between the side walls in contact, and the restoring force of the displaced fins, create a locking mechanism where both structures are held in place. The system proved to be water-tight up to pressures of 138 kPa.

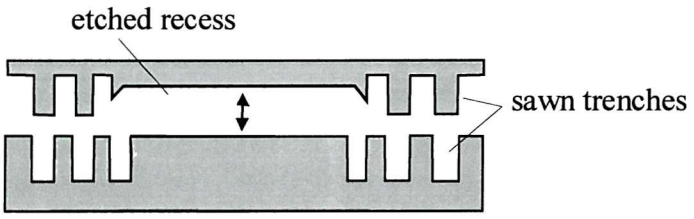

Figure 2.8: Schematic of a finger micro joint [Gonz98a, Gonz98b].

- silicon tubing (figure 2.9): The connection interface consists of two silicon wafers that were fusion bonded together. The wafers were etched so that a tube can be plugged horizontally in the chip or alternatively, two matching silicon tubes could be plugged into each other [Gonz98a, Gonz98b].

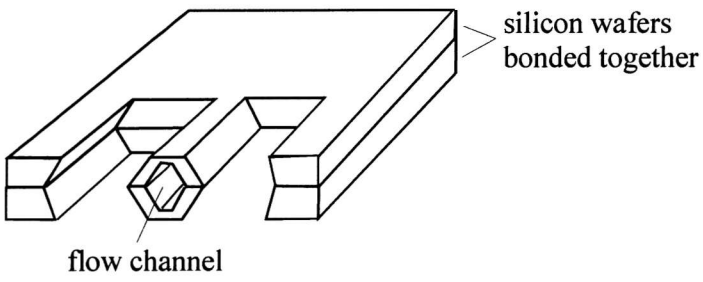

Figure 2.9: Schematic of a silicon tube connector [Gonz98a, Gonz98b].

- plug-in connection: Tubes were plugged vertically or horizontally into etched holes or trenches, respectively and held in place by epoxy glue. Often, two or more bonded layers of wafers were used [Gray99].

- pyrex/silicon circuitboard: Flow channels were etched anisotropically into silicon to connect the microfluidic devices and the microchannels were sealed with a pyrex cover by anodic bonding. The fluidic devices were glued onto the silicon [Rich97].

2.2.5 Integrated Microfluidic Systems

The area of integrated microfluidic systems has become a very extensive research field with numerous applications. Rather than presenting an exhaustive review of all of these applications for this review chapter, an overview on the basis of selected papers is given. Chapters on integrated microfluidic systems can be found in Koch [Koch00] and Kovacs [Kova98] and also in review articles [Harr00, Dari00, Shoj94]. The following classification of the various fluidic systems has been adapted from Koch [Koch00].

2.2.5.1 Dosing systems and drug delivery

In most cases, a dosing system consists of a micropump or an active valve in connection with a flowsensor. A monolithically assembled system has been presented by Elwenspoek [Elwe94]. The pump and the flow sensor were fabricated on the same silicon wafer sandwiched between two pyrex wafers and the operation of each device is based on a thermal principle (figure 2.10). The membrane of the pump is displaced by heating air in an enclosed chamber above the membrane and the flow sensor works by heating a resistor and measuring the temperature difference on resistors placed upstream and downstream. The net dose of the dosing system at 0.5 Hz and 5 W power input to the pump is about 0.7 µl/cycle. However, the pump output was not controlled by the output from the flowsensor.

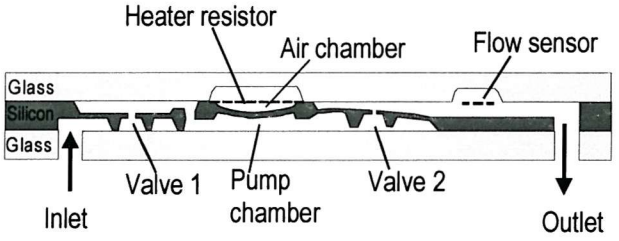

Figure 2.10: Schematic of monolithically assembled dosing system [Elwe94].

Other published dosing systems are hybrid assemblies. Nguyen [Nguy98] used a pump (9 mm x 9 mm) actuated either by a piezodisc or an alternating electrostatic force and a thermal flow sensor (6 mm x 12 mm). The pump and flow sensor were mounted on a perspex plate that contained milled connection channels and fluidic ports. The system is bidirectional and was tested for water within a flow range of –40 µl/min to 80 µl/min. Another example of a hybrid

silicon based dosing system has been presented by Gass [Gass93b]. A drag force flow sensor was mounted over a piezoelectrically actuated membrane pump outlet. A set output flowrate of 55 µl/min was obtained by regulating electronics controlling the actuation voltage of the piezo disc below 3.5 kPa. The response time of the regulated system was measured to be 200 msec and the overall size of the system was 15 mm x 28 mm x 28 mm (figure 2.11).

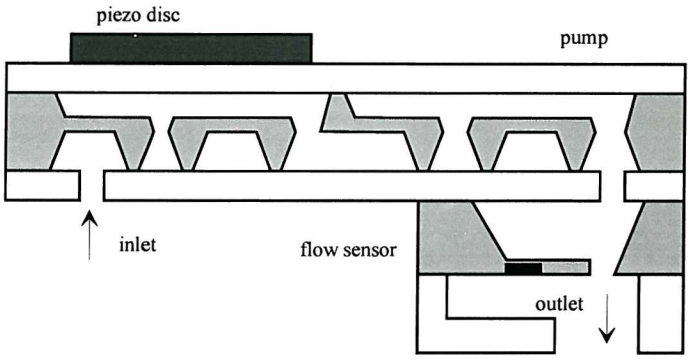

Figure 2.11: Hybrid dosing system [Gass93b].

A novel dosing system has recently been published by Boehm [Boeh00]. The applied driving force to dispense liquids originates from the electrochemical generation of gas bubbles by the electrolysis of water. By adopting an integrated electrode geometry, the electrodes can be used for electrochemical gas generation as well as for the simultaneous determination of the total gas bubble volume, via an impedance measurement of the gas/liquid mixture in the reservoir. The reference states that dosed volumes can be controlled within an error margin of ± 5 nl.

Madou [Mado00] proposed the use of hydrogels for controlled drug delivery. The hydrogel 'Poly(HEMA-co-acrylamide-co-acrylic acid)' swells and shrinks under chemical stimuli, i.e. different pH levels. The presented super-porous hydrogel with 200 – 500 µm diameter pores can swell by over 1000 % in 3 min. When the super porous gel was placed in a low pH level solution, it shrank by 62 % in 3 min. However, after 5 cycles (swelling and shrinking) the gel became fragile. The entrapment of glucose oxidase in the super porous hydrogel made it responsive to the glucose concentration in a phosphate buffer solution (pH = 7.3). Therefore, it could be used as both a sensor and an actuator at the same time. It was also reported that another hydrogel 'poly(2-hydroxyethyl)methacrylate combined with polyaniline displays significant swelling and shrinking upon applying an electrical potential from –0.2 V to +0.8 V. Beebe [Beeb00], van der Linden [Lind00] and Liu [Liu00] used hydrogels for in-channel processing of microvalves.

A silicon microchip for the controlled release of single or multiple chemical substances on demand was developed by Santini [Sant99]. The release mechanism is based on the electrochemical dissolution of a gold membrane covering the reservoirs. The chip contains 34 reservoirs connected one by one to an external power source. If the release of a reservoir is desired an electrical voltage, of approximately 1 V, is applied between the anode and cathode. The anode, the gold membrane that covers the reservoir, dissolves and the drug inside diffuses out into the surrounding fluid. Each reservoir can be activated individually.

2.2.5.2 Medical, chemical and environmental monitoring

An example for medical monitoring has been presented by Hediger [Hedi00]. He developed a microsystem for the electrical characterisation of epithelial cell layers for biomedical diagnostic purposes. Miniaturised cell culture devices have been realised by gluing nano-porous polycarbonate membranes in between two structured silicon wafers and by assembling glass wafers to provide integrated micro-fluidic channels (figure 2.12). The surface of a single culture site (determined by the area of the membrane) ranges between 1 and 4 mm^2. An epithelial cell layer was grown and its electrical behaviour using two and four point impedance measurements was characterised. The need for only a small amount of cells or biological fluids is just one of the advantages of miniaturisation. In a macrosystem, non-integrated and mechanically positioned electrodes are a source of uncertainty in determining the correct cell layer resistance, as the varying contact geometries can give rise to large resistances in the physiological cell medium. Therefore, the reproducibility and accuracy of the electrical characterisation is improved with a microsystem.

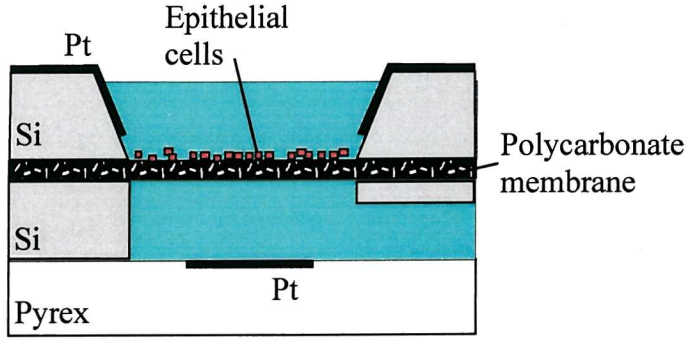

Figure 2.12: Schematic cross-section of the tissue measurement structure [Hedi00].

Krog [Krog00] presented a prototype continuous flow sensing-system for ammonia in water matrices based on colorimetric detection, which is given as an example for environmental monitoring (figure 2.13). This colorimetric reaction involves three reagents that were consecutively mixed with the sample, and the coloured reaction product was determined by optical absorption. The device is based on a hybrid principle where the mixing sections, reaction manifold and optical cuvette were integrated in an anodically bonded three-layer pyrex/silicon/pyrex chip. The cross section of the meandering channels is 40 x 210 μm^2. The three reagents (not stated), two calibration standards (0 and 20 mg N-NH_4Cl per litre), the carrier (not stated) and a cleaning solution (HCl) were dispensed to the microsystem through capillary tubes by the external pump/valve system. The optical detection consists of optical fibres guiding the light from a halogen lamp to the cuvette and from the cuvette to a spectrometer. To protect the silicon from corrosion by the alkaline reagents, it was coated with LPCVD silicon nitride. The system is operated at a flow rate of 0.2 µl/min, which results in a sampling time of 3.5 min. The detection limit for ammonia (NH_3, NH_4^+) is between 0.5 mg/l and 20 mg/l.

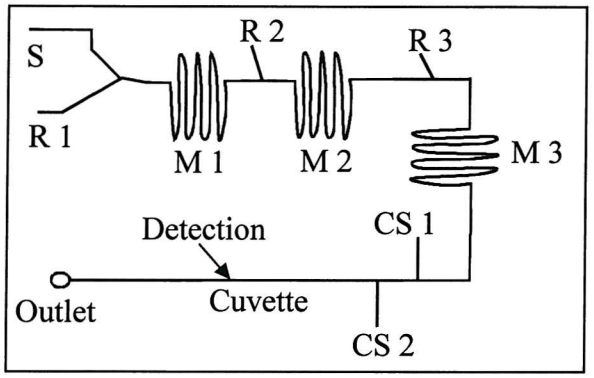

Figure 2.13: Schematic of an ammonia sensing system;
S, R, M, CS are sample, reagents, mixers and calibration standards.

A microanalysis system for the measurement of pressure, flow rate, temperature, conductivity, UV-absorption and fluorescence on a single chip has been described by Norlin [Norl98] and is given as an example for chemical monitoring. The intention is that it be used as a detector after liquid chromatography. The system was made of a quartz glass wafer containing sensors for pressure, temperature, conductivity and fluid flow, a silicon wafer used to define the measurement volume of the liquid and an optical fibre interfacing system for the UV-absorption and fluorescence measurements (figure 2.14). The channel dimensions were 9 x 1 x 0.5 mm^3, giving a cell volume of 5 µl. The pressure sensor consisted of a closed cavity under a poly-Si membrane. The pressure-induced strain in the membrane was measured with piezo-resistors of doped poly-Si. The thermal flow sensor was made of thin film layers of aluminium and poly-Si. The temperature monitoring was done by platinum thin-film thermistors with a nominal resistance of 500 Ω. The conductivity was measured with two adjacent planar platinum electrodes of 500 x 1000 µm, with a distance of 400 µm between them. Two laterally connected optical fibres enabled UV-light to be introduced into and collected from a volume of the liquid. The optical path length was 9 mm. The fluorescent measurement setup consisted of a bundle of seven optical fibres connected to the fluid channel from below. The excitation light (laser diode 1 mW, λ = 630 nm) was guided through the centre fibre and the outer six fibres transmitted the fluorescent signal back to a photodetector. All measurement principles have been individually characterised, but no detection after liquid chromatography has been presented.

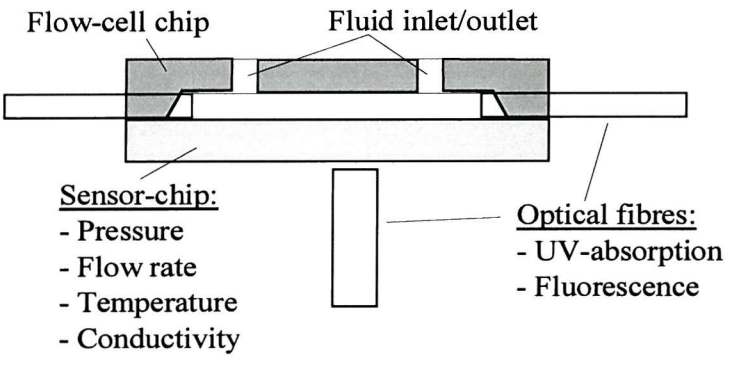

Figure 2.14: Schematic of the microanalysis system [Norl98].

2.2.5.3 Drug discovery and genetic diagnostics: DNA sequencing

Manz [Manz97] presented an electroosmotic drug discovery system. The microstructured glass chip contains one injection channel and 17 parallel channels and is controlled by four electrodes (figure 2.15). The system is capable of distributing an incoming serial sample stream to a set of multiple parallel channels, hence the term serial to parallel converter is used by the author. A separation can then be performed in each channel, leading to increased throughput. The diameter of the channels is 50 x 10 μm^2 and the distance between them is 500 μm. Sample introduction and parallel electrophoresis used voltages of 2 to 2.8 kV. Initial testing was carried out to visualise the flow of solutions in the chip. To do this, the sample solution consisted of fluorescein or rhodamine B at a high concentration (10 μM) to make it easy to observe the fluorescence either by eye or with a CCD camera. The buffer used was 100 mM borate at a pH of 9. An example of the application of this system would be to take a single sample of genomic DNA and analyse it in parallel with many different DNA probes or primers for PCR amplification resulting in different products. A very similar attempt has been published by Bousse [Bous97].

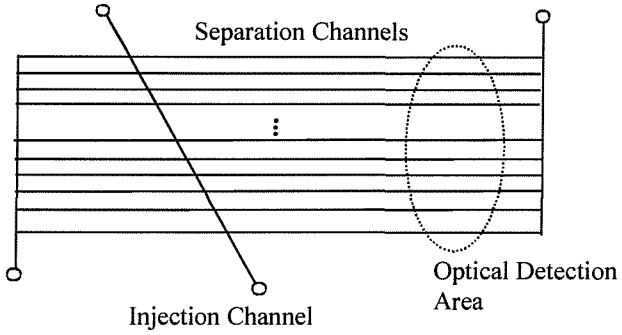

Figure 2.15: Schematic of a drug discovery system [Manz97].

Badal [Bada00] developed an integrated micro system for DNA analysis that has the potential to be used for clinical diagnostics or for detection of bacterial pathogens in the environment. The system performs on-chip mixing, reaction and separation using capillary electrophoresis (figure 2.16). Microchannels were etched in 4x4 inch glass and access holes for probe, enzyme and target DNA were drilled into a cover plate, which was thermally bonded to the glass plate. The reagents are mobilised electrokinetically to the reaction coil, which sits on an external aluminium heating block. After mixing and incubating (30 min at 60 °C) in the reaction coil, the products are then electrokinetically mobilised to the separation channel, where the products are separated and detected by laser induced fluorescence. To verify the system for clinical diagnostics, quantitative data was obtained with a methicillin resistant Staphylococcus aureus (MRSA) sample. To test the system for detection of bacteria in the environment, a genomic DNA sample derived from Erwinia herbicola was successfully used.

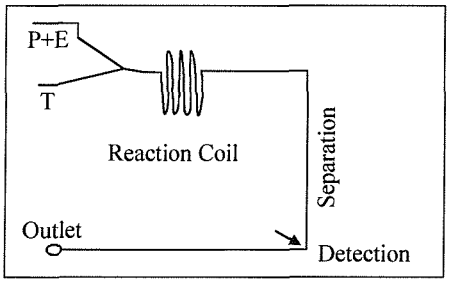

Figure 2.16: Schematic of a DNA analysis system [Bada00].
P, T and E are probe, target and enzyme.

2.3 Conclusion

The large variety of different devices with applications in various areas shows clearly, that microfluidics is a very interesting research field. Especially the BioMEMS field is promising for commercialising microfluidic devices and systems.

Commercialising however requires reliable devices and a library of components, which can be integrated into versatile systems. Only two micromachined silicon pumps able to pump gases and liquids, which are tolerant to gas bubbles have been presented so far. However, both are unsuitable for mass production. Therefore, it was the intention to address this point in the development of a gas/liquid micropump.

The integration of fluidic devices to systems requires control of the fluid flow. Therefore, a microflow sensor is very desirable. Several principles have been presented, whereupon the thermal measurement principle is the most often used. Thus, another aim of the project was to develop a microflow sensor, which is versatile and hence can be integrated in different fluidic systems.

A number of PCR-chips for DNA amplification has been developed. There are arrays and flow through devices for drug development and DNA screening and there are single shot PCR devices for the detection of DNA. For certain applications, e.g. environmental detection on site, it is advantageous to amplify the DNA sample in a very short time and have simultaneous optical detection. Only one device with high heating and cooling rates and the possibility of optical detection has been presented so far, however, the device was quite large (20 x 18 mm^2). For cheap production it is of advantage to have a small chip size, as the cost per wafer is the same. A major aim of this thesis was to develop a very fast and small PCR chip with the possibility for optical detection.

For the creation of complete microfluidic systems it was necessary to address the interconnection between devices, as there are no standards available. This interconnects should be easy to fabricate, be versatile, i.e. allow the creation of different fluidic devices, be reliable and leak-tight. Thus, a novel microfluidic circuitboard was planned to be developed and as a demonstrator a chemical microplant consisting of various different devices was intended to be realised.

CHAPTER 3

Self-Aligning Gas/Liquid Micropump

3.1 Introduction

Several micropumps have been developed up to now based on various principles for the actuator and valve units. The pumps are usually mechanical of the membrane type [Pol90, Smit90, Zeng94, Zhan96, Bena97, Koch97a, Koch98b] or alternatively the flow is induced by an electric field [Rich91a, Manz91, Jaco94]. Valves ranging from simple passive check valves [Esas89, Zeng92, Yang96] to electrostatically driven active diaphragm valves [Bosc93] have been presented.

Most of the micropumps described in the literature are extremely sensitive to the entrapment of gas bubbles inside the pump chamber, which severely deteriorates the pump performance. Moreover, gases cannot be pumped at all in many cases. However, the application of a micropump requires maximum reliability, which means that the device should be tolerant towards gas bubbles. The aim of the research described in this chapter was to develop such a micropump.

The miniaturised gas/liquid micropumps presented up to date are reviewed in chapter 2.2.1. Among the different working principles of micropumps, the concept of a diaphragm pump actuated piezoelectrically with passive dynamic valves was chosen for the pump described in this chapter. A schematic of the pump can be seen in figure 3.1. The overall size of the pump is 12 x 12 mm^2 with a height of 0.6 mm (without the PZT actuator). The liquid-only micropump previously characterised by our group [Koch97a, Koch98b, Koch00] is using the same actuation and valve principle and therefore experience in operating this devices has been gained.

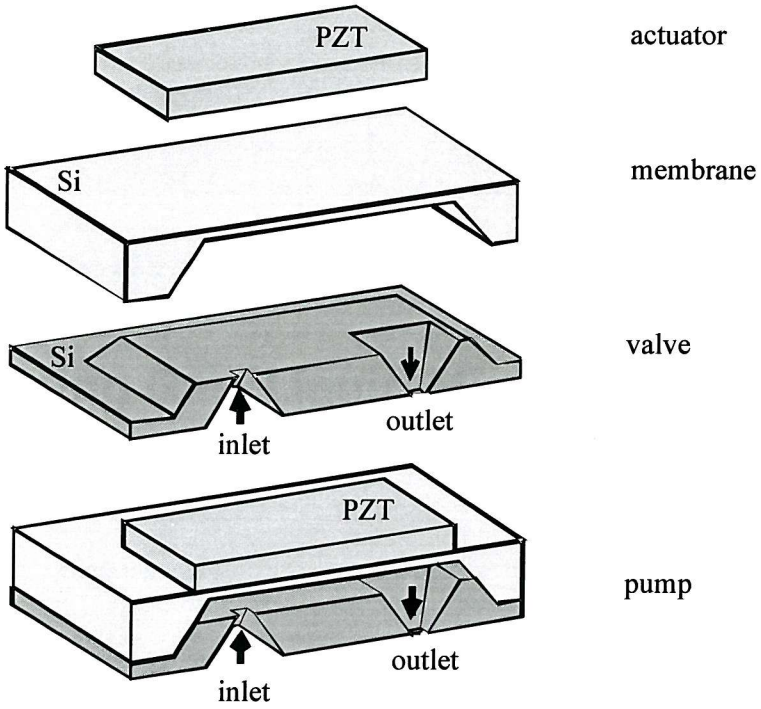

Figure 3.1. Schematic of the different units creating the micropump.

Gerlach [Gerl97] and Linnemann [Linn98] have made similar attempts to fabricate a piezoelectrically driven gas micropump in silicon. One approach uses passive dynamic valves, the other passive cantilever valves. However, both are not suitable for mass fabrication and are not self-aligning, which are novel features of the micropump developed here.

In the following, the design of the micropump minimising the dead volume and enabling self-alignment of the membrane to the valve unit is described along with the possibility of using thick-film screen-printing of PZT as a membrane actuator to enable mass production of the micropump. Then the fabrication is explained and the dependency of the pump rate on the actuation frequency is simulated. The test procedure used for demonstrating the pump performance is described and measurement results are compared to the simulated results.

3.2 Design

The main difference of pumping gases compared to liquids is that to create the necessary pressure, the gas has to be compressed. The membrane micropump must have a certain compression ratio ε, which is determined by the volume displacement ΔV and the pump chamber volume V_{ch} [Linn98]:

$$\varepsilon = \frac{\Delta V}{V_{ch}} \tag{3.1}$$

The ratio of the volume displacement induced by the membrane over the mean pump chamber volume needs to be as high as possible. This is achieved by minimising the dead volume of the pump chamber and by maximising the stroke volume of the pump diaphragm.

3.2.1 Minimising the Dead Volume and Self-Aligning

As can be seen in figure 3.1 the dead volume of the pump chamber described here is minimised by inserting the valve unit into the membrane unit. The valve unit is designed to slide into the opening of the membrane unit from the back, with the recess surrounding the projection sealing the pump. Both, the membrane and valve wafer are 500 µm thick. The membrane wafer is etched leaving a 70 µm thick diaphragm and the valve wafer is etched leaving a 100 µm thick recess. Thus, after sliding into each other, this gives a chamber height of only 30 µm. Furthermore, this technique allows self alignment of the pump during the assembly stage.

The micropump characterised by Koch [Koch97a, Koch98b, Koch00] has a chamber volume of V_{ch} = 15.4 µl. The volume displacement due to the piezoelectric actuation for the 8 mm x 4 mm membrane was simulated using ANSYS 5.4. An applied voltage of 300 V yields a displaced volume of ΔV = 41.2 nl. This gives a compression ratio of ε = 1:373.

The new micropump with the reduced chamber height has a volume of V_{ch} = 1.5 µl. The simulated displaced volume with the same applied voltage is ΔV = 150 nl with a 7 mm x 7 mm membrane. This gives a compression ratio of ε = 1:10, which is about 40 times larger than the previous design. Linnemann [Linn98] states a theoretical minimum compression ratio for his pump design of ε = 1:13.4 to achieve gas pumping. This ratio is deduced on the assumption of a valve unit consisting of cantilever valves and taking into account the specific pressure required to open the valve. We use this number as a rough guide for our pump and comparing this, we assume the new micropump will be able to pump gas. The compression ratio for the two pump designs versus applied voltage is depicted in figure 3.2.

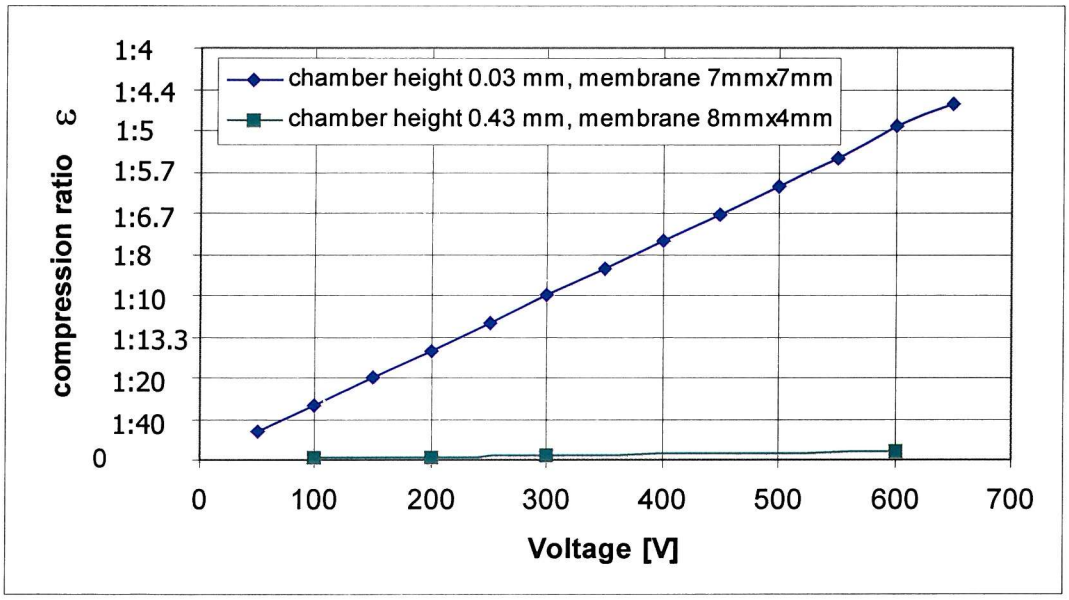

Figure 3.2: Compression ratio for the two pump designs versus applied voltage.

3.2.2 Maximising the Stroke Volume

In order to optimise the actuator unit, the diaphragm was changed from a rectangular shape of 8 x 4 mm^2 to a square shape of 7 x 7 mm^2. The PZT layer has been adapted from 7 x 3 mm^2 to 6 x 6 mm^2. The maximum deflection δ_{max} at the centre of the membrane has been calculated for both membrane types using the two-dimensional formulas derived by Koch [Koch00]:

$$\delta_{max} = \left(\kappa + \frac{M}{EI}\right)\left(-\frac{1}{8}L_m{}^2 + \frac{s}{2}L_m - \frac{1}{2}s^2\right) + \frac{1}{2}\frac{M}{E_S I_S}s^2 \tag{3.2}$$

with κ being the second derivative of the deflection per unit width calculated using:

$$\kappa = \frac{-d_{31}\cdot E_{el}}{\frac{h}{2} + \frac{2}{h}\cdot\left(\frac{1}{E_P h_p} + \frac{1}{E_S h_S}\right)(E_S I_S + E_P I_P)} \tag{3.3}$$

The bending moment M is given by:

$$M = \frac{1 - \frac{L_m}{2s}}{\frac{1}{E_S I_S} + \frac{1}{EI}\left(\frac{L_m}{2s} - 1\right)}\cdot\kappa \tag{3.4}$$

EI stands for the Young's modulus times the second moment of area for the compound beam of silicon and PZT and is calculated by:

$$EI = \frac{1}{12}\frac{h_P^4 E_P^2 + 4h_P^3 E_P h_S E_S + 6h_P^2 E_P h_S^2 E_S + 4h_P E_P h_S^3 E_S + h_S^4 E_S^2}{h_P E_P + h_S E_S} \tag{3.5}$$

E_P = 126·10^9 Pa is the Young's modulus of PZT, E_S = 168·10^9 Pa is the Young's modulus of silicon in <110> direction, L_m = 4 mm (7 mm) is the length of the shorter side of the membrane, s = 0.5 mm is the distance between the PZT layer to the fixed ends of the silicon membrane, d_{31} = -274·10^{-12} CN^{-1} is the piezoelectric coefficient for PZT-5H material, $E_{el} = \frac{U}{h_p}$ is the electrical field across the PZT layer with U as the applied voltage. The second moment of area for unit width is calculated from $I_i = \frac{h_i^3}{12}$ with h_i as height of the individual layer and h = h_S+h_P; h_S = 70 µm and h_P = 250 µm.

The results from the calculations have been verified using ANSYS 5.4. Comparing the results from the analytical calculations and the ANSYS simulations for the different membrane sizes, as shown in figure 3.3, a 2.4-times larger deflection of the 7 x 7 mm^2 membrane than the 8 x 4

mm^2 membrane for the same applied voltages to the PZT material is revealed, thus giving a larger stroke volume of the pump diaphragm as shown in figure 3.4.

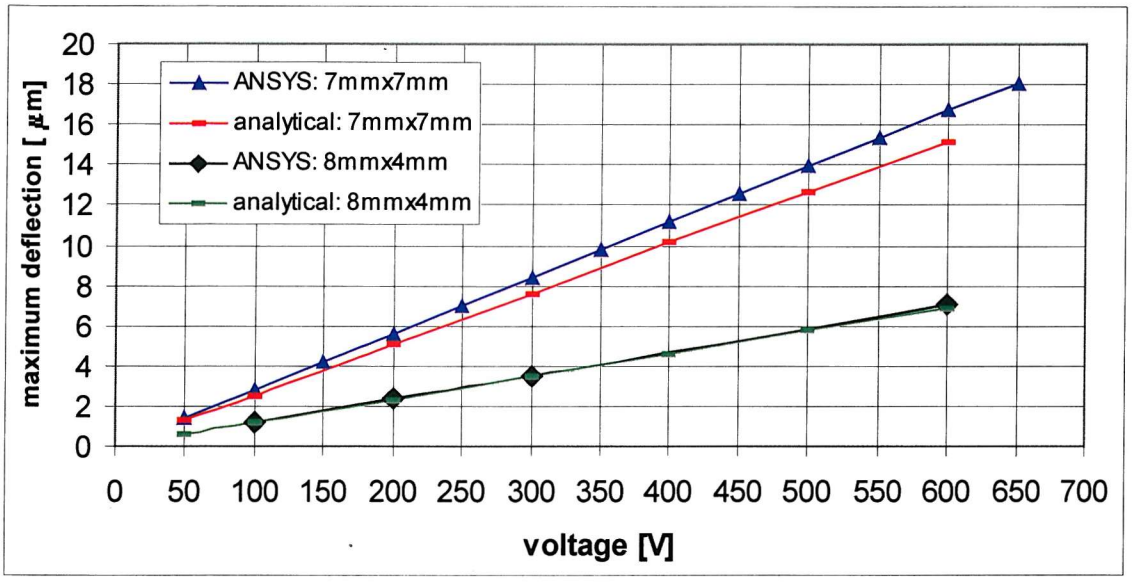

Figure 3.3: Analytical calculations and ANSYS 5.4 simulations of the maximum deflection of the pump membrane versus applied voltage to the PZT material.

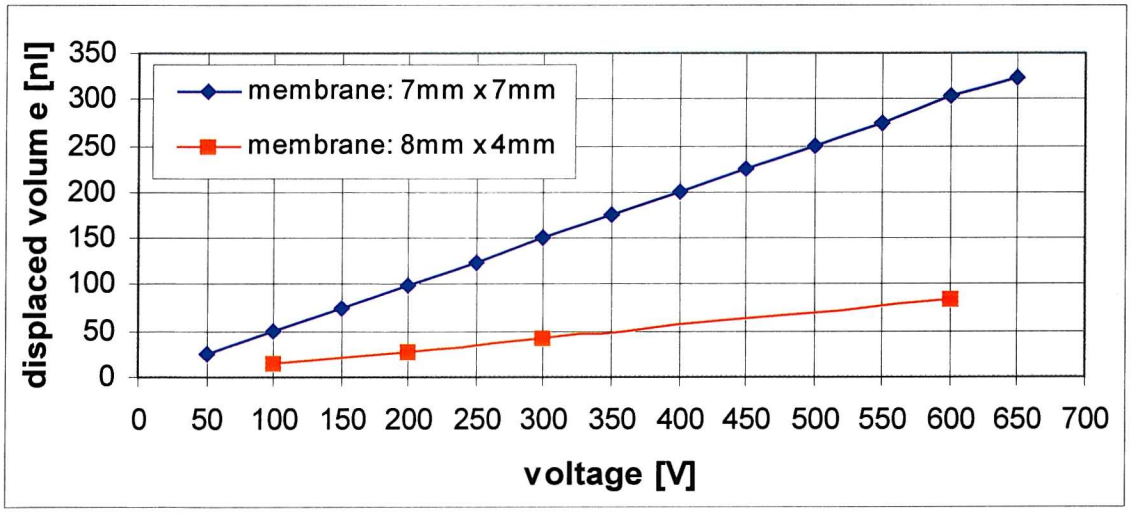

Figure 3.4: ANSYS 5.4 simulation of the displaced volume under the membrane versus applied voltage to the PZT-layer.

3.2.3 Dynamic Passive Valves

Unlike the passive cantilever valve, the dynamic passive valve does not rely on any moving parts. This valve is dependent on the difference in the flow rate through a duct in opposite directions where the same pressure difference is applied. To fulfil this attribute the duct is cone shaped, with the inlet area being of a different dimension than the outlet area. A schematic of the valve is shown in figure 3.5. The advantage of a valve without moving parts is its simple fabrication and it enables the handling of particle containing fluids. Furthermore it can operate at high frequencies, thus allowing the pump to run at its resonant frequency enabling the maximum deflection of the diaphragm. The valve only operates in dynamic mode, with a net flow in the nozzle direction (for $\alpha \approx 35°$). The forward to reverse flow rates are typically 10:9 and are small compared to cantilever valves (better than 100:1) [Koch00].

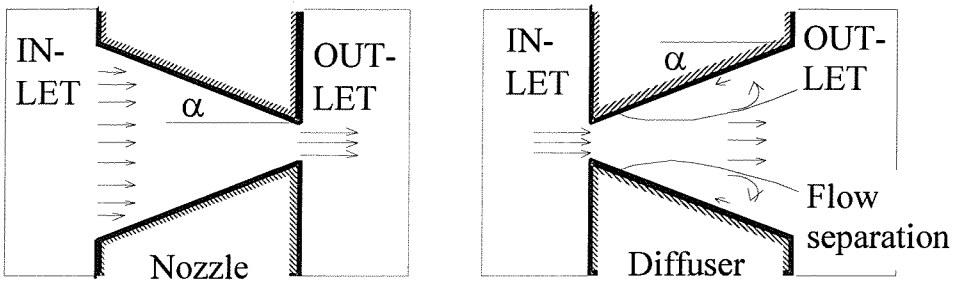

Figure 3.5: Principle of the diffuser/nozzle valves.

The valves used for the gas/liquid micropump have been characterised by Koch [Koch97a, Koch98b, Koch00]. The flow through the diffuser and nozzle is related to the pressure difference between the inlet and outlet and is given by:

$$\Delta p_{diff} = \frac{128 \cdot \mu \cdot \Phi_V}{3\pi \tan\alpha}\left(\frac{1}{D_0^3} + \frac{1}{(D_0 + L_c \tan\alpha)^3}\right) + \frac{8\rho \Phi_V^2}{\pi^2}\left(\chi_{sc}\frac{1}{D_0^4} + \chi_{ge}\frac{1}{D_0^4} + \chi_{se}\frac{1}{(D_0 + L_c \tan\alpha)^4}\right) \tag{3.6}$$

$$\Delta p_{nozzle} = \frac{128 \cdot \mu \cdot \Phi_V}{3\pi \tan\alpha}\left(\frac{1}{D_0^3} + \frac{1}{(D_0 + L_c \tan\alpha)^3}\right) + \frac{8\rho \Phi_V^2}{\pi^2}\left(\chi_{sc}\frac{1}{(D_0 + L_c \tan\alpha)^4} + \chi_{gc}\frac{1}{D_0^4} + \chi_{se}\frac{1}{D_0^4}\right) \tag{3.7}$$

where μ = 1.2·10^{-3} Pa·s and ρ = 789 kg·m^{-3} are the dynamic viscosity and density of ethanol, Φ_V is the volume flow through the diffuser/nozzle, α = 35.3° is the taper angle of the cone, D_0 = 130 µm is the smaller diameter of the cone, L_c = 500 µm is the length of the cone,

and χ_i are the head loss factors; χ_{sc} = 0.44 sudden contraction, χ_{se} = 1 sudden expansion, χ_{gc} = 0.1 gradual contraction, χ_{ge} = 1 gradual expansion. The head loss factors are determined by the taper angle rather than by the fluid as transitional losses (potential energy into kinetic energy) dominate over viscous losses and they are experimentally obtained data [Koch00].

The flow rate versus pressure difference for the diffuser and nozzle structure is depicted in figure 3.6. It can be seen that for a given pressure, the flow through the nozzle is larger than through the diffuser, hence resulting in a net flow rate in the nozzle direction.

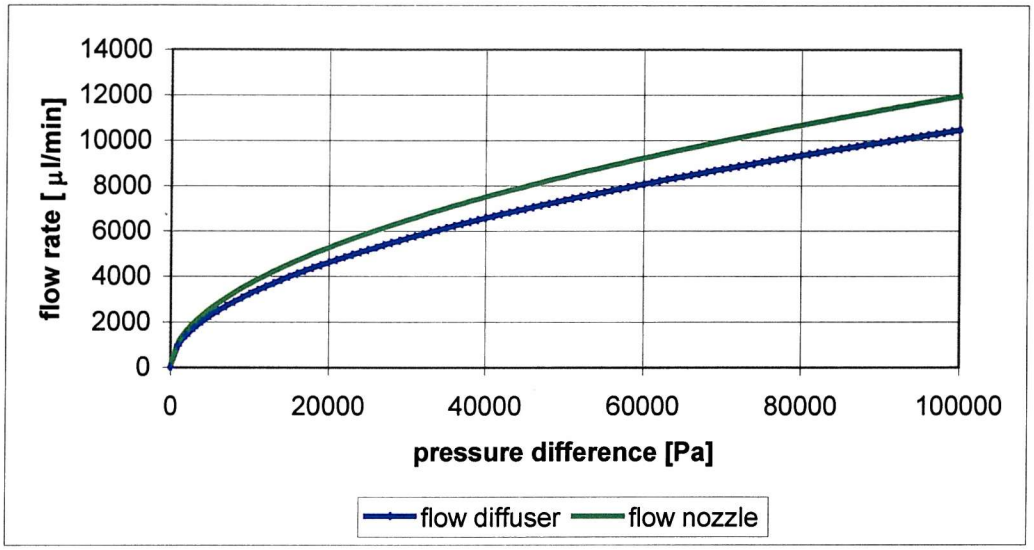

Figure 3.6: Flow versus pressure of diffuser/nozzle structures for a taper angle of 35.3° and ethanol as liquid using equations 3.6 and 3.7.

3.2.4 Varying Number of Valves: Pump Simulations

In order to achieve high pump rates, arrays of different numbers of inlet and outlet valves have been investigated. They have been varied from one inlet and one outlet up to 10 inlets and 10 outlets.

The flow rates for the micropump have been simulated for a membrane size of 7 mm x 7 mm x 70 µm and an actuator size of 6 mm x 6 mm x 250 µm using following equation [Koch00]:

$$\frac{dp}{dt} = \frac{\Phi_v(p_{inlet} - p) - \Phi_v(p - p_{outlet}) - \delta_U \cdot \frac{dU}{dt}}{\gamma_p} \tag{3.8}$$

where p is the chamber pressure, Φ_v is the volume flow through diffuser/nozzle using values obtained from equations 3.6 and 3.7 with ethanol, U is the sinusoidal voltage applied to the piezoelectrics $U(t)=U_0 \cdot \sin(2\pi \cdot f \cdot t)$, $\delta_U = \frac{dV}{dU} = 0.5 \cdot 10^{-12} \frac{m^3}{V}$ and $\gamma_p = \frac{dV}{dp} = 5.4 \cdot 10^{-16} \frac{m^3}{Pa}$ are characteristic values of the pump membrane and are obtained from ANSYS 5.4 simulations.

The equation was solved using Maple 6. The results for the different number of inlet and outlet valves can be seen in figure 3.7. It shows that for frequencies below 1000 Hz the pump rate is the same for all simulations. Only at higher frequencies, the pump rate from a higher number of inlet and outlet valves surpasses the pump rate from lower numbers of inlet and outlet valves. This can be explained by the pressure within the pump chamber. The pressure created at a certain frequency is distributed to the number of valves. For a larger number of valves the frequency needs to be high to build up a pressure that gives a reasonable difference between diffuser and nozzle flow.

For the design of the gas/liquid micropump, the six inlet/six outlet-valve setup was chosen as the pump was expected to be operated below a frequency of 5000 Hz. Experience with the previous design of the pump characterised by Koch [Koch00] showed that the maximum pump rate is achieved below that frequency.

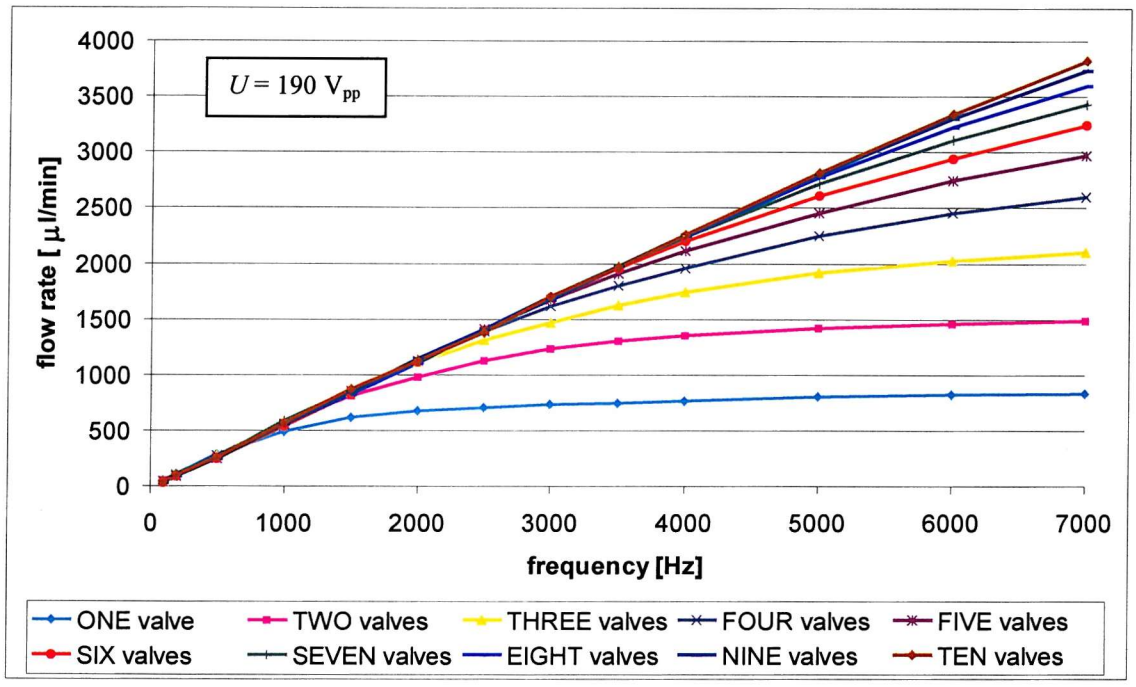

Figure 3.7: Simulation of the frequency behaviour of the pump with different numbers of inlet valves using equation 3.8. The simulations assume zero backpressure.

3.2.5 Mass-Produced Membrane Actuator

The membrane of the micropump is actuated piezoelectrically. For mass production of the micropump, PZT can be printed onto the whole silicon wafer by thick-film technology. The printing of PZT onto silicon is described by Koch and Maas [Koch97a, Maas97, Koch98b] and the performance data have been obtained for the previous micropump design with a silicon membrane of 8 mm x 4 mm x 70 µm with a screen printed actuator of 7 mm x 3 mm x 100 µm. A SEM photograph of the thick-film printed PZT can be seen in figure 3.8.

To enable thick-film printing, the top of the membrane wafer needs to be flat and the new design of the gas/liquid micropump provides this platform for the screen printing mass

fabrication technology. Due to the insertion of the valve into the membrane cavity the top of the membrane wafer is kept flat and this is a great advantage over the designs presented by Gerlach [Gerl97] and Linnemann [Linn98], which both do not have the possibility of enabling mass fabrication methods for the actuator.

However, the first tests of the gas/liquid pump have been done with bulk PZT material as only a few pumps are necessary to evaluate the performance of the new design and it also saves the cost for the screen printing sieves and the printing materials. A 250 μm thick PZT-5H plate from Morgan Matroc Ltd. was sawn into 6 x 6 mm^2 pieces, which were then glued onto the membrane chips using conductive epoxy glue.

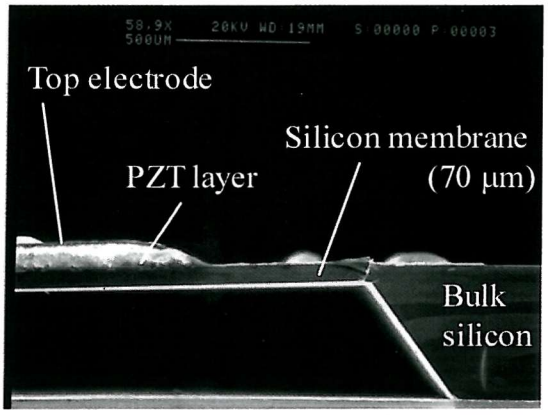

Figure 3.8: Thick-film actuator on a micromachined silicon membrane [Koch00].

3.3 Simulation

3.3.1 Liquid Pumping

The flow rate and the backpressure of the micropump with six inlet and outlet valves have been simulated using equation (3.8) from section 3.2.4. The flow through diffuser/nozzle has been analytically calculated using equations (3.6) and (3.7) from section 3.2.3 with the data for ethanol as the liquid. The simulation results for the pump rate versus frequency applied to the PZT actuator with two different actuation voltages can be seen in figure 3.9.

At low frequencies the pump rate is not high, as a high frequency is required to build up a reasonable pressure difference between the diffuser and the nozzle flow. From a frequency of 500 Hz onwards the pump rate increases steadily up to a frequency of 10000 Hz. Beyond this point, the curves level towards a maximum pump rate above which it can not be increased by increasing the frequency. The simulation using the larger actuation voltage gives a higher pump rate.

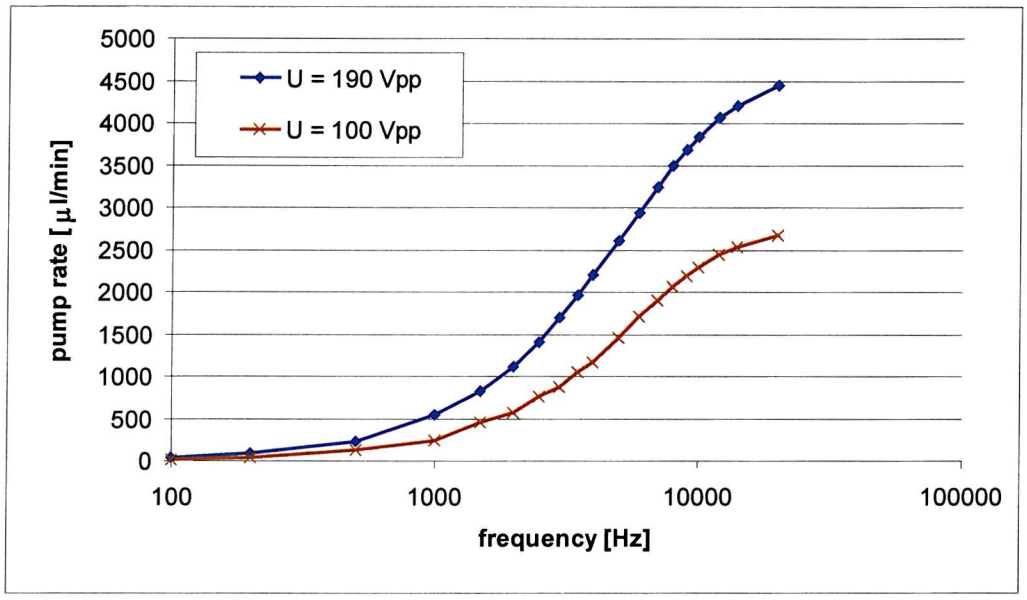

Figure 3.9: Simulation of the pump rate versus frequency of the micropump for ethanol as liquid; D_0 = 130 µm.

The dependence of the pump rate on the applied backpressure is depicted in figure 3.10. The actuation frequency for the simulation was varied as indicated in the legend of the graph and the voltage was 190 V_{pp}. A linear drop of the pump rate with respect to the applied backpressure at the outlet can be found for all simulation results. The simulations show that larger backpressures can be achieved for higher frequencies.

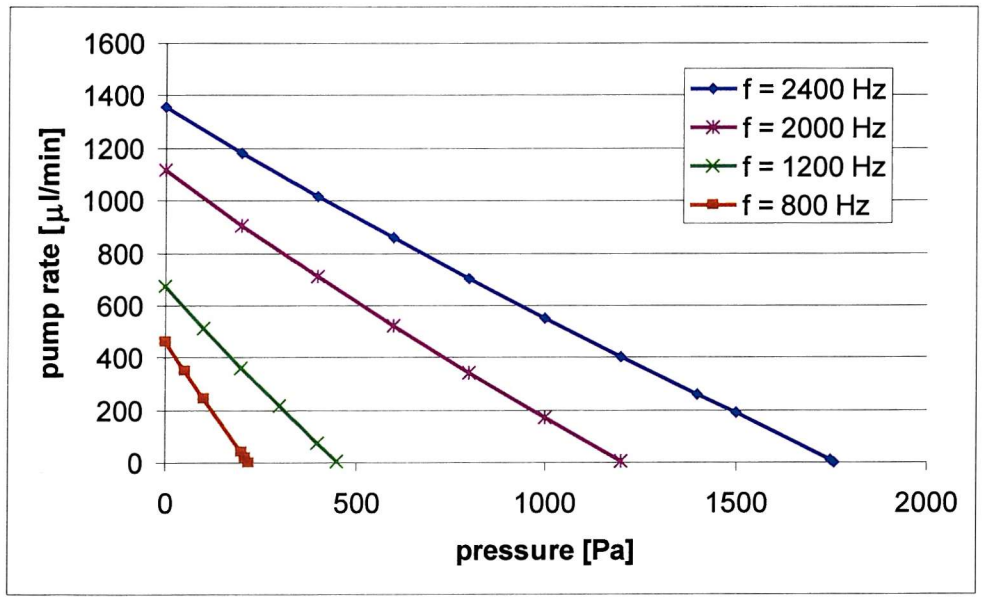

Figure 3.10: Simulation of the pump rate versus backpressure of the micropump for ethanol as liquid; U = 190 V_{pp}.

3.3.2 Gas Pumping

The flow rate and the backpressure of the micropump with six valves have been simulated using equation (3.8) from section 3.2.4. The flow through diffuser/nozzle has been analytically calculated using equations (3.6) and (3.7) from section 3.2.3 with the data for air as the fluid (density air: ρ = 1.2982 kg·m^{-3}, dynamic viscosity air: μ = 18.1·10^{-6} Pa·s). The above formula is valid for incompressible fluids. Air, however, is compressible and therefore a lower measured flow rate compared to the simulation is expected. A higher pressure difference within the pump chamber is necessary to pump an equal amount of compressible fluid compared to an incompressible fluid.

The simulation results for the pump rate versus the frequency applied to the PZT actuator with a voltage of 300 V_{pp} can be seen in figure 3.11. The results show a similar behaviour to the results from the simulation using ethanol. At low frequencies the pump rate is not high, as a high frequency is required to build up a reasonable pressure difference between the diffuser and nozzle flow. From a frequency of 1000 Hz onwards the pump rate increases steadily beyond the highest simulated frequency of 20 kHz. The simulated flow rates are very high. This is due to the difference of two orders of magnitude in the density and viscosity of air compared to ethanol.

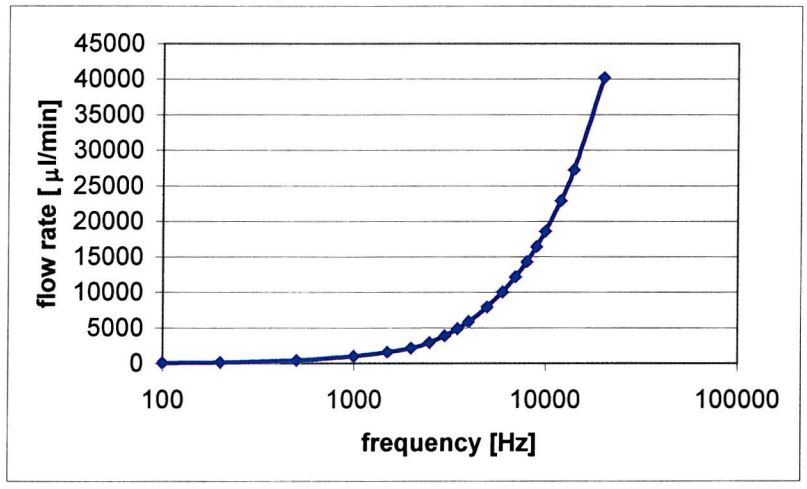

Figure 3.11: Simulation of the pump rate versus frequency of the micropump with air as the fluid.

The dependence of the pump rate on the applied backpressure is depicted in figure 3.12. The actuation frequency for the simulation was 3400 Hz and the voltage was 300 V_{pp}. The slope of the linearly decreasing backpressure is very high. It gives a maximum backpressure of 28.3 Pa, which is rather low. The density and viscosity of air is two magnitudes lower than ethanol, therefore giving only low backpressures.

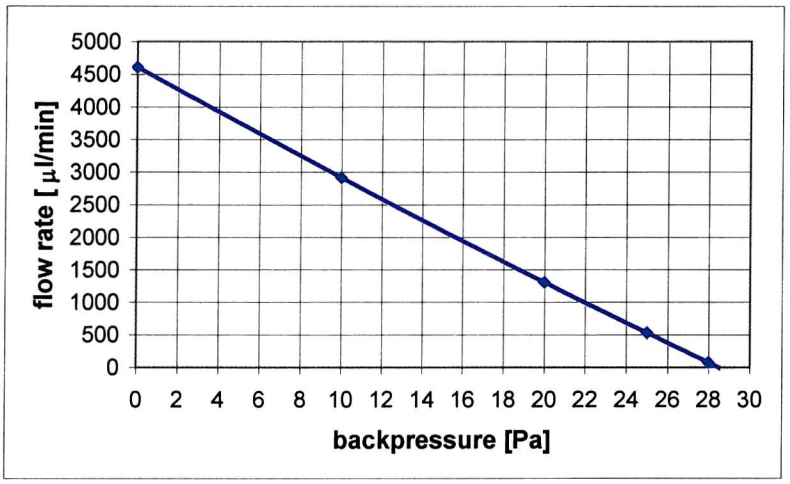

Figure 3.12: Simulation of the pump rate versus backpressure of the micropump for ethanol as liquid.

3.4 Micromachining of the Pump

3.4.1 Passive Dynamic Valves and Valve Projection

The micromachining is based on double sided processing of 4 inch <100> oriented silicon wafers. Double sided alignment structures are necessary because the inlet and the outlet valves are etched at the same time from both sides of the wafer. Photoresist, Shipley SPRT511, is patterned on the front of the wafer. Then 1 µm deep structures are etched into the silicon by reactive ion etching with SF_6 as a reaction gas. The resist is stripped by plasma ashing and a new resist is patterned on the back of the wafer. This time the mask for the exposure of the resist is aligned to the first mask on the front side with the help of infrared light shone through the silicon wafer. Again, after the 1 µm deep dry etch, the resist is stripped by plasma ashing.

The next section of the fabrication process involves the creation of the patterns for the inlet and outlet valves on both sides of the wafer before the bulk etch. An RCA cleaning stage is followed by a dry oxidation (80 nm) and the deposition of LPCVD nitride (160 nm). Photoresist, Shipley SPRT511, is patterned on the front of the wafer while another layer of resist protects the back. After spinning resist onto the edge of the wafer the inlet valve pattern is generated on the front by reactive ion etching with argon and CHF_3 as reaction gases. The protection of the oxide and nitride on the edge of the wafer is necessary due to the subsequent KOH etch, which would leave the wafer fragile due to the jagged edge produced in KOH solution. Stripping the resist by plasma ashing is followed by patterning a new layer of resist on the back of the wafer. After that, the edges are again protected by a layer of resist. The nitride and oxide on the back is etched by reactive ion etching to leave the patterns for the outlet valve. After stripping the resist the wafer is dip etched in 20:1 buffered hydrofluoric acid and then placed into a potassium hydroxide (KOH) etch bath (30%, 70 degC). The silicon is etched to a depth of 100 µm, the first part of the etch for the inlet and outlet valves (figure 3.13a). This

partial etch of the valves is necessary because of the subsequent process to create the recess where the membrane wafer is to be placed in the assembly stage of the pump (figure 3.13f).

Creating this recess is the last part of the valve fabrication. Photoresist, Shipley SPRT511, is patterned on the front of the wafer with the back and edge protected subsequently. The pattern for the recess is created by reactive ion etching into the nitride and oxide layers with argon and CHF_3 as reaction gases (figure 3.13b). After that, the resist is stripped by plasma ashing. A dip etch in 20:1 buffered hydrofluoric acid is followed by a final etch in KOH (30%, 70 degC) to etch 400 µm deep into the silicon. This KOH etch completes the creation of the inlet and outlet valves and leaves a 100 µm thick platform. The valve fabrication ends with a nitride and oxide strip in orthophosphoric acid at 160 degC and in 7:1 hydrofluoric acid respectively (figure 3.13c). A SEM photograph of the valve unit can be seen in figure 3.14.

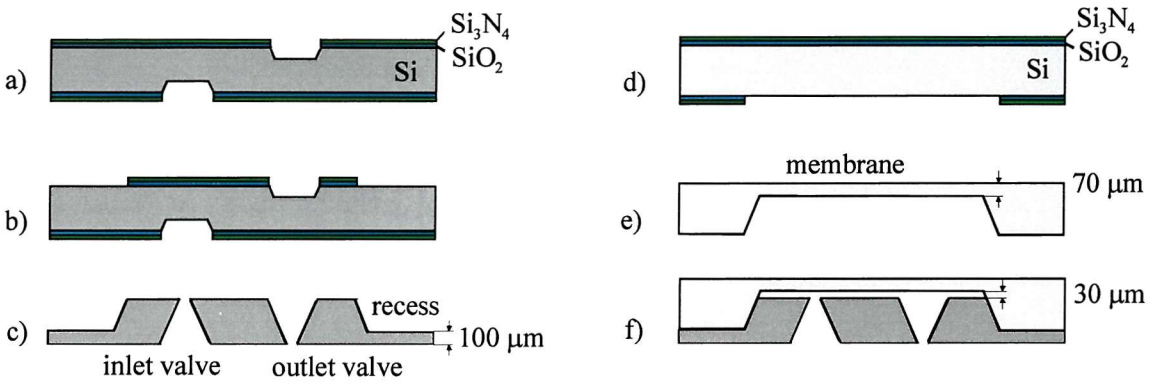

Figure 3.13: Schematic of the fabrication process of the valve (a – c), the membrane (d – e) and the combination of both (f).

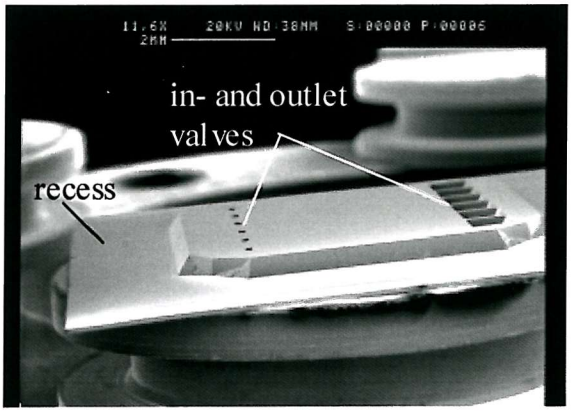

Figure 3.14: SEM photograph of the valve chip.
(see figure 3.13c for sectional view)

3.4.2 Membrane

The fabrication of the membrane starts with a dry oxidation (80 nm) and a LPCVD nitride (160 nm) deposition. The fabrication process requires only one lithography step in which the patterns for the membrane openings are created. Double sided polished 4 inch <100> oriented wafers are used. The nitride and oxide are etched by reactive ion etching with argon and CHF_3 as etch gases. The resist is stripped by plasma ashing (figure 3.13d). Now the wafer is dip etched in 20:1 buffered hydrofluoric acid and then placed into a KOH etch bath (30%, 70 degC) to etch 430 µm into the wafer leaving a membrane with a thickness of 70 µm. This etch is a timed etch with an etch rate of 0.54 µm/min. Last, the nitride is stripped with orthophosphoric acid at 160 degC and the oxide is stripped with 7:1 buffered hydrofluoric acid (figure 3.13e).

A SEM photograph of the assembled gas/liquid micropump consisting of the passive dynamic valve unit, the membrane unit and the PZT actuator can be seen in figure 3.15.

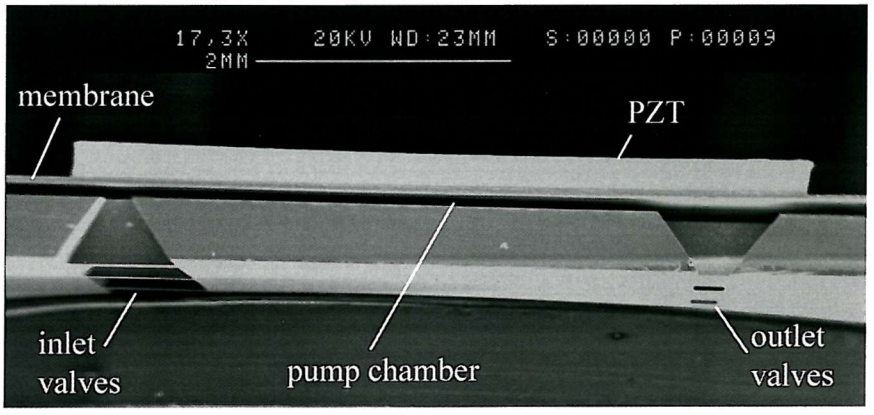

Figure 3.15: Cross-section of the assembled micropump.
(see figure 3.13f for sectional view)

3.5 Measurements and Comparison to Simulation Results

To test the performance of the novel micropump design, several measurements have been carried out. First, the membrane displacement at certain frequencies and voltages applied to the piezo-actuator was determined. Then the pump rate performance of the pump using ethanol as liquid was tested followed by a test showing the bubble tolerance of the pump. Finally the ability of the micropump to pump air is shown.

3.5.1 Membrane Displacement

In order to test the actuation behaviour of the membrane actuator, the central displacement of the membrane was measured with a single mode optical fibre laser interferometer. A signal

generator was connected to the PZT and a sinusoidal waveform was employed in all experiments for driving the actuator. Figure 3.16 shows the measurement setup.

The frequency dependence of a 7 mm x 7 mm x 70 μm membrane with a 6 mm x 6 mm x 250 μm PZT plate glued on top has been tested. A voltage of 40 V_{pp} was applied to the electrodes of the PZT plate and the frequency was varied between 1 kHz and 7 kHz. The deflection versus the frequency is depicted in figure 3.17. Two membranes have been tested and both show a resonance peak at 2.4 kHz with a maximum deflection of about 1.1 μm. Frequencies below 4 kHz give a reasonable deflection of the membrane whereas for high frequencies the deflection converges towards zero. The peak at 2.4 kHz is the natural resonance of the membrane combined with the glue and the PZT.

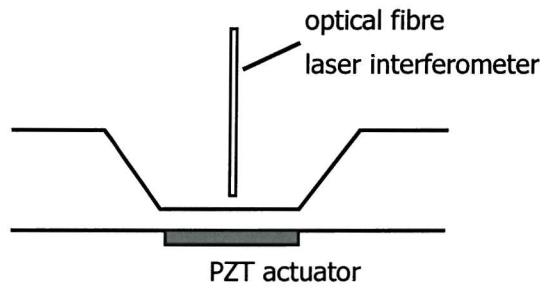

Figure 3.16: Measurement setup for the membrane actuator.

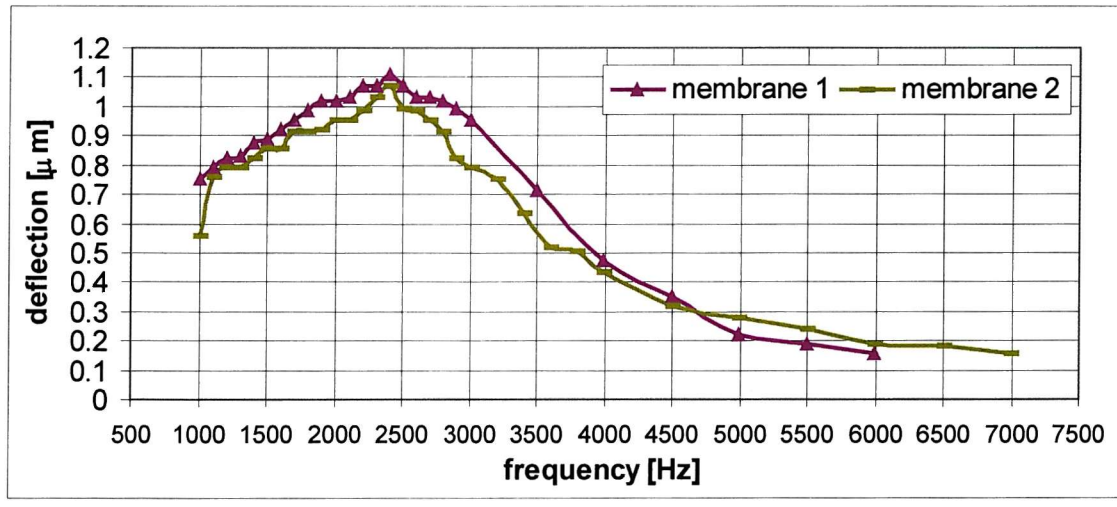

Figure 3.17: Frequency dependence of the surface mounted membrane actuator.

Next, the deflection versus the applied voltage at a fixed frequency of 2.4 kHz was measured. It can be seen in figure 3.18 that the deflection of the membrane actuator increases linearly as the voltage applied to the PZT is increased. The measurement data are in very good agreement with the results from the ANSYS 5.4 simulation and with the analytically calculated data from section 3.2.2.

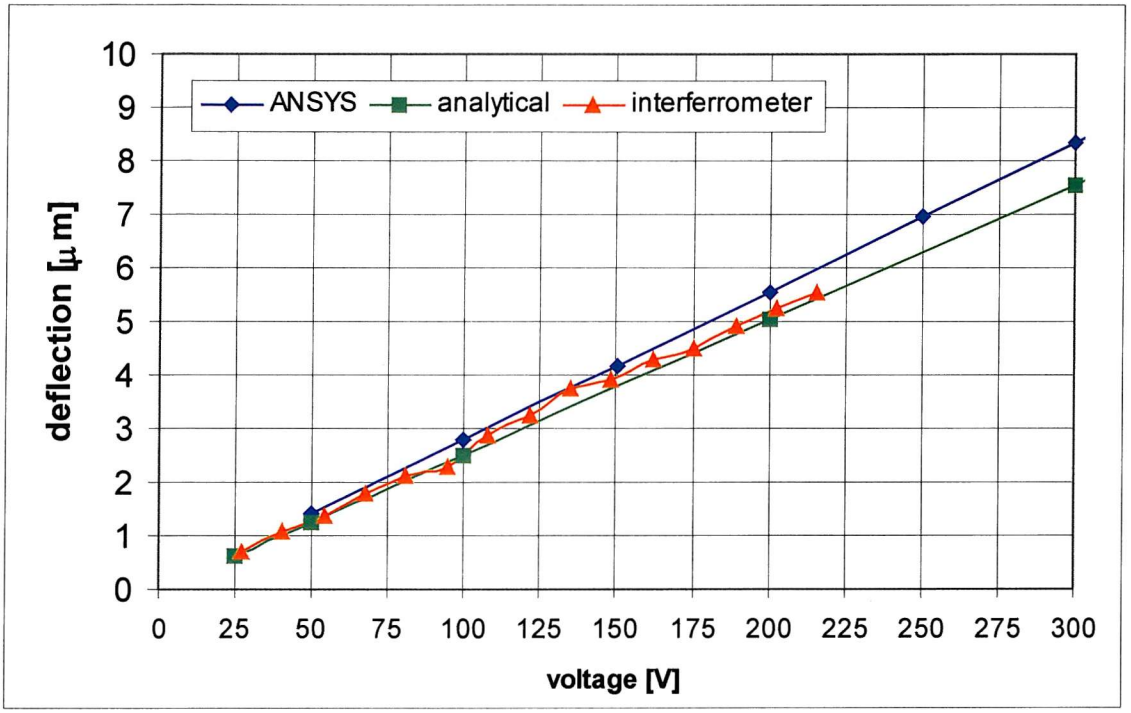

Figure 3.18: Deflection of the membrane versus applied voltage for ANSYS simulation, analytical calculation and interferometer measurement.

3.5.2 Liquid Pumping

The liquid pumping was tested using a jig manufactured from Perspex (figure 3.19). Two metal pipes of 3 mm outer diameter, on which plastic hoses could be connected, were inserted on opposite sides into drilled holes. Another set of holes (1 mm diameter) was drilled perpendicularly from the top of the Perspex dice. Two recesses of 8 mm x 2 mm were milled 1mm deep to enable all six inlet and outlet valves to be filled with fluid. The test jig is 14 mm wide, 14 mm long and 12 mm high. Photographs of the test jig without and with the pump mounted on top can be seen in figure 3.20 and figure 3.21. Perspex was used due to its transparency and due to its compatibility with Cyanoacrylate glue. The transparency makes it possible to observe the presence of adhesive in all the necessary places particularly between the inlet and outlet valves. Because of its resistance to ethanol Cyanoacrylate adhesive was used to glue the silicon micropump chip unlike epoxy glue, which dissolved after only a few minutes of pump operation.

The pump was primed by the pressure from the height of the liquid column from the inlet hose. Careful attention was given not to trap any air bubbles within the measurement setup as this would distort the results. Ethanol has been favoured as a test liquid due to its low surface tension and its high tendency to dissolve air [Koch97b].

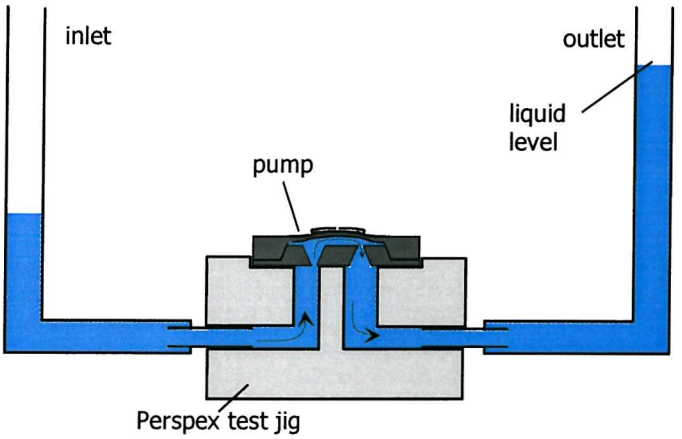

Figure 3.19: Measurement setup for the micropump test.

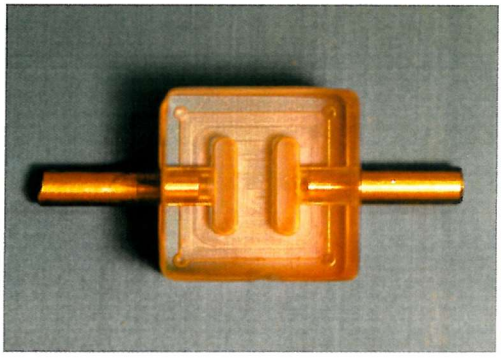

Figure 3.20: Photograph of the Perspex test jig.

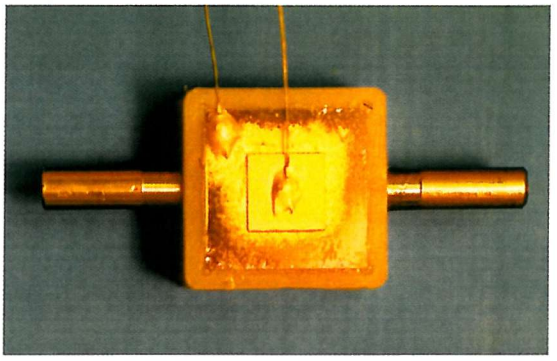

Figure 3.21: Photograph of a pump mounted onto a test jig.

Once the pump chamber had been filled with ethanol, a signal generator was connected to the piezoelectric membrane actuator. A sinusoidal waveform was employed in all experiments for driving the actuator.

The pump rate was calculated by the volume displacement in the outlet hose at zero backpressure divided by the time necessary. Figure 3.22 depicts the pump rate of the micropump over a frequency range between 0.5 kHz and 3.5 kHz and an applied voltage of 190 V_{pp}. A pump rate of 1500 µl/min was achieved at a frequency of 2.5 kHz.

The simulation using the analytically calculated flow data through the diffuser and the nozzle gives the tendency of the pump behaviour up to a frequency of 2.5 kHz, albeit with significantly larger pump rates at frequencies below 2.5 kHz (figure 3.22). At higher frequencies the measured pump rate drops whereas the simulated pump rate increases. The decline shown in the measurements can be explained by a fluid dynamic effect of the diffuser/nozzle valves, which is not included in the simulation model. The flow through the diffuser/nozzle can not follow the high frequencies.

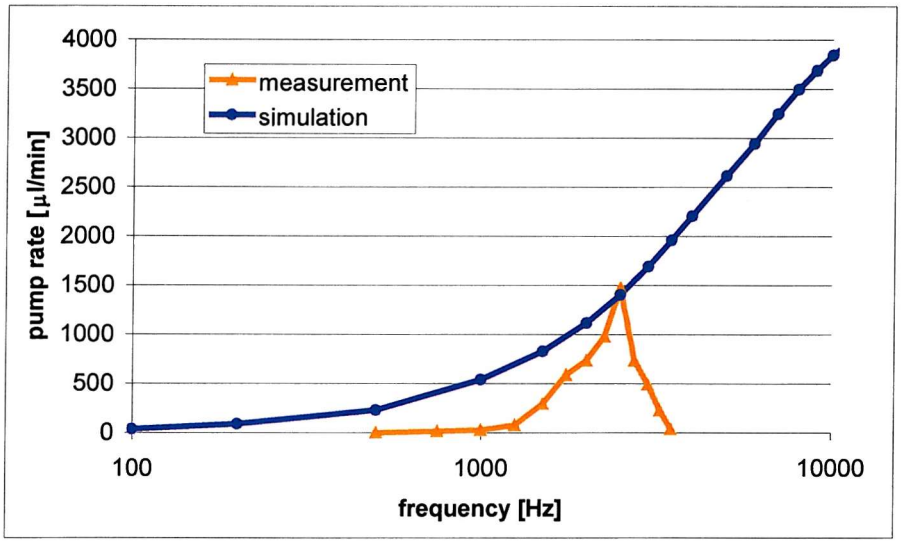

Figure 3.22: Pump rate of the hybrid actuated micropump for sinusoidally shaped actuation: frequency dependence; $U = 190\ V_{pp}$.

The measured drop of the pump rate versus the backpressure can be seen in figure 3.23. To measure the backpressure the height of the liquid column within the outlet hose was observed during pump operation. At a certain height, the liquid column stops moving, which indicates the maximum pressure the pump is able to pump against. The pump rate was calculated from the height difference of the outlet liquid column at certain points divided by the time necessary. A voltage of 190 V_{pp} at a frequency of 2.4 kHz was applied to the PZT, giving a maximum backpressure of 1000 Pa.

In figure 3.23 the simulation result from section 3.3.1 is included. The model predicts a maximum backpressure of 1700 Pa, which is close to the measured backpressure of 1000 Pa. The same linear drop of the pump rate with increasing backpressure is observed.

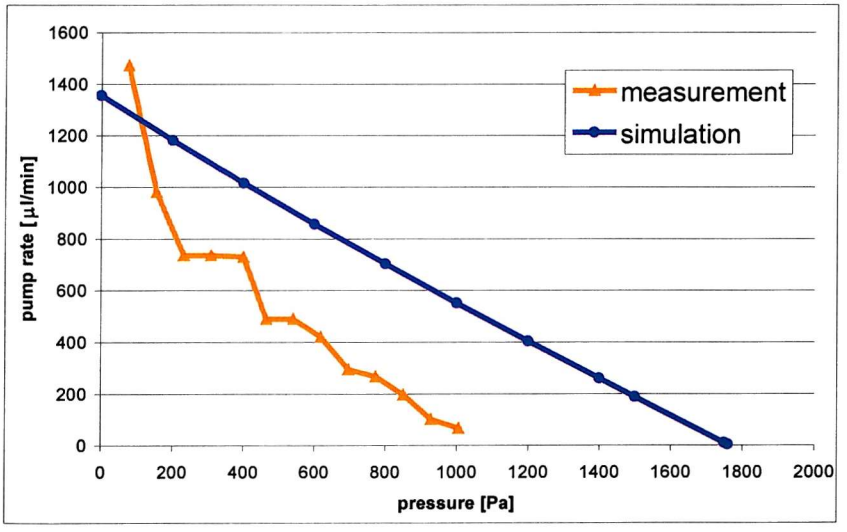

Figure 3.23: Pump rate of the hybrid actuated micropump for sinusoidally shaped actuation: backpressure dependence; $f = 2400$ Hz, $U = 190\ V_{pp}$.

3.5.3 Bubble Tolerance and Gas Pumping

The pump is designed to pump gases as well as liquids. Two tests have been carried out to evaluate the pump performance. First the pump was tested as regards bubble tolerance and second its ability to pump air was measured.

3.5.3.1 Bubble tolerance

To test the bubble tolerance of the novel micropump design, the pump was filled with ethanol as described above. A 2-way valve was connected to the inlet hose to insert air bubbles into the flow stream as depicted in figure 3.24. The pump was operated with a voltage of 190 V_{pp} and a frequency of 2.5 kHz.

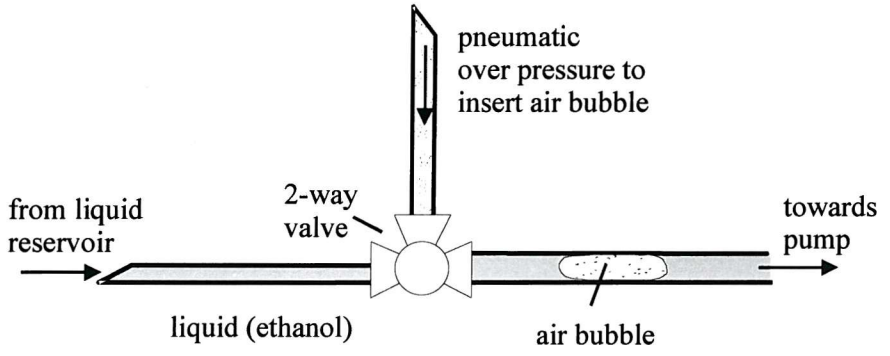

Figure 3.24: Measurement setup for bubble tolerance tests.

During operation of the micropump with ethanol as liquid air bubbles were inserted into the flow stream. When a bubble entered the pump, the performance dropped until the bubble was released from the pump chamber.

The pump showed tolerance to small air bubbles, however, once the size of the bubble exceeded a certain volume (3 mm long, 1.25 mm in diameter: ≅ 14 µl, which is three times the chamber volume), the bubble would slowly enter the chamber but would not come out preventing the pump from working. It was assumed that if the bubble filled the entire chamber then the air replaced the ethanol as the fluid in the pump and the compression ratio was not large enough to continue pumping.

The pump was cut in half and the chamber height was measured with a SEM (scanning electron microscope) to be 86 µm. Additional investigation showed that the adhesive layer bonding the membrane and valve chip had a height of 30 µm and the membrane had been over-etched reducing its thickness to 50 µm instead of 70 µm. Taking these factors into account together with the thickness variation of the membrane and valve wafers gives a rather large chamber volume of V_{ch} = 4.3 µl resulting in a compression ratio of ε = 1:43 for an actuation voltage of 190 V_{pp}. This shows that the compression ratio was not high enough and to achieve gas pumping ε needs to be increased.

3.5.3.2 Gas pumping

In response to the measurement results from the previous section, the compression ratio ε was further increased by reducing the chamber height of the micropump and by increasing the actuation voltage, hence increasing the stroke volume. The thickness of the chip containing the membrane was reduced, the high viscous epoxy adhesive was replaced by a low viscosity Cyanoacrylate glue and the actuation voltage was increased to 300 V_{pp}.

The measurement setup is depicted in figure 3.25. The micropump was glued on top of the test jig described in 3.5.3.1 and the outlet hose was placed 4 mm deep into a beaker containing water giving a backpressure of 40 Pa. A signal generator was connected to the piezoelectric and a sinusoidal waveform was employed in all experiments for driving the actuator. The frequency was varied between 1 kHz and 3.8 kHz and the number of air bubbles leaving the outlet hose into the water beaker was counted.

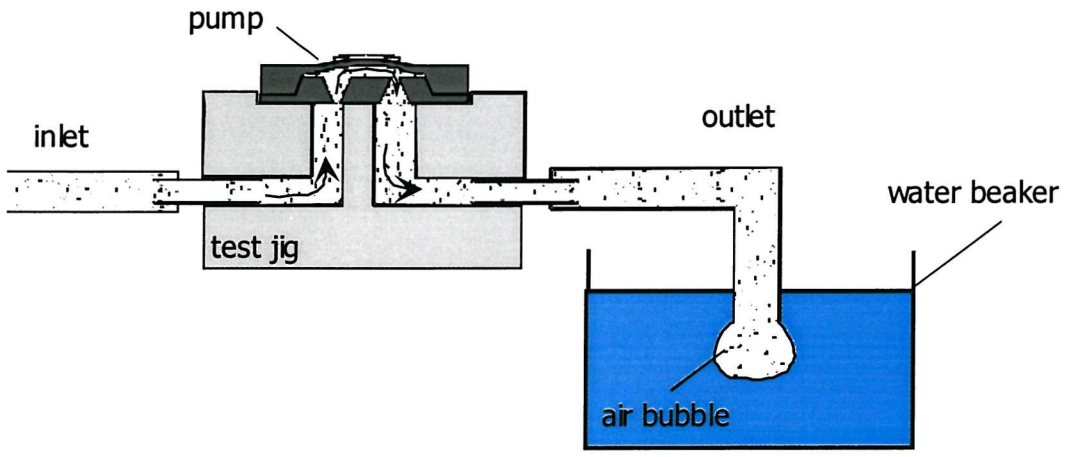

Figure 3.25: Measurement setup for gas pumping.

The measured results are shown in figure 3.26. Up to a frequency of 3.3 kHz no pumping was observed. At a frequency of 3.4 kHz the pump rate reached a maximum of 21 bubbles leaving the outlet hose within two minutes. At a frequency of 3.5 kHz the number of air bubbles was 14 and at a frequency of 3.6 kHz the number of bubbles was 1 within two minutes of operation. At higher frequencies no more pumping could be observed. The test was repeated twice with similar results, as can be seen also in figure 3.26.

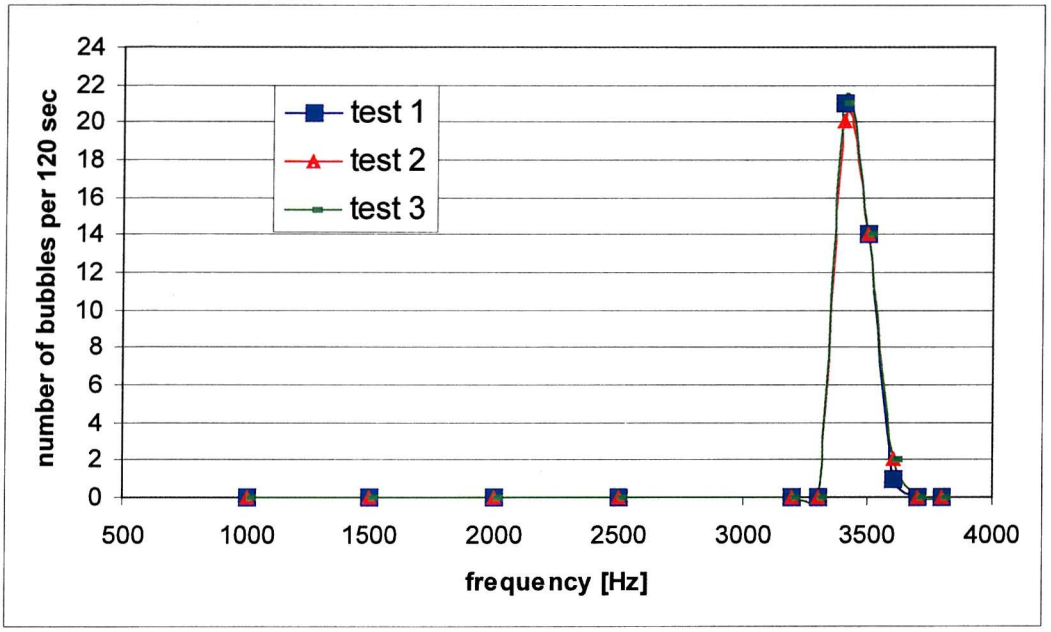

Figure 3.26: Measurement results for gas pumping.

The size of bubbles leaving the outlet hose was approximately twice the inner diameter of hose, which was 1.25 mm. Assuming that the bubbles were spherical, an approximate gas pumping rate of 690 µl/min at a frequency of 3.4 kHz was given. A shift of the frequency with the highest pump rate from 2.5 kHz with the previous micropump to a frequency of 3.4 kHz was observed. The diaphragm resonance and the system resonance, which includes the dynamic behaviour of the valves have an influence on the resonance frequency of the pump. The membrane of the pump tested with ethanol was first actuated in air without the valves and showed a resonance frequency of 2.4 kHz (section 3.5.1). Then actuated as a system, including the valves and ethanol as fluid, the resonance frequency was 2.5 kHz. The pump tested in this section had a resonance frequency of 3.4 kHz as a system resonance. The diaphragm resonance was not measured on its own. Further investigation would be necessary to state whether the diaphragm resonance or the system resonance is the decisive factor for varying the resonance frequency of the pump.

The manual assembly of the pump has an influence on the resonance frequency of the diaphragm. The thickness of the conductive epoxy glue with which the PZT was bonded to the silicon membrane can vary and also the PZT itself can be placed off centre, which has an influence on the stiffness of the membrane. The resonance frequency will increase with a stiffer membrane.

Comparing the measured results with the simulation from section 3.3.2 shows a significant difference in the flow rates (figure 3.27). However, this is not surprising as the equation used for the simulation is only valid for incompressible fluids.

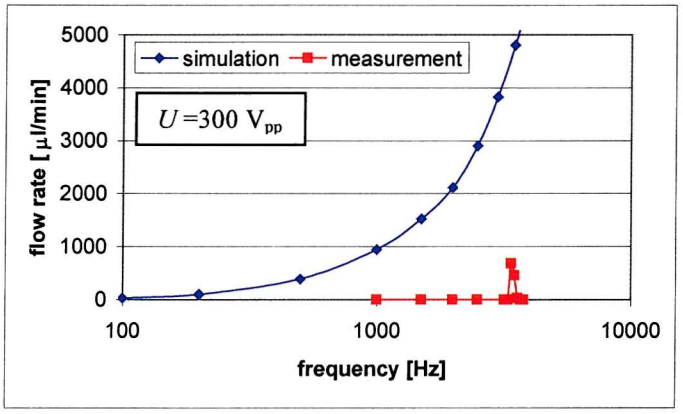

Figure 3.27: Comparison of measured results to simulation for air pump rate.

SEM measurements done after the pump testing revealed that the chamber height was as little as 18 µm with the Cyanoacrylate used to bond the membrane and valve chip having had a height of only 5 µm compared to the epoxy glue having had a height of 30 µm. The compression ratio for a chamber height of 18 µm and an actuation voltage of 300 V_{pp} was ε = 1:6.

With the measurement results given it shows that the new micropump is able to pump gas. However, to obtain more accurate pump rates a different measurement setup is necessary. The outlet of the pump could be placed into a glass cylinder, which is upside down in a water beaker. The displaced volume of water within the cylinder would be a measure of the pump rate. However, in this technique the backpressure changes. Another measurement technique would be the use of a calibrated flow sensor with low impedance or the observation of the travel distance of a water drop within a horizontal outlet hose. The backpressure could be measured with a pressure sensor placed at the outlet of the pump.

3.6 Conclusion

In this chapter, a piezoelectrically actuated micropump with passive dynamic valves designed for pumping gas and liquid and being tolerant towards gas bubbles has been presented. This aim was reached by minimising the pump chamber volume and by maximising the deflection of the membrane. The pump has been designed so that during assembly the valve unit slides into the membrane unit to decrease the height of the pump chamber, hence reducing the dead volume within the pump. This design enables at the same time the self-aligning of the two units to each other. The size of the membrane has been changed from the previous rectangular shape of 8 mm x 4 mm to a square shape of 7 mm x 7 mm to increase the deflection of the membrane. ANSYS 5.4 simulations and analytical calculations of the membrane deflection have been carried out. With the improvements made, the compression ratio of the pump was enhanced from ε = 1:373 for the previous design to ε = 1:6 for the new design.

Passive dynamic diffuser/nozzle valves have been used and a study for employing rows of one to ten inlet/outlet valves has been done. It showed that for frequencies below 1000 Hz the pump rate is the same for all simulations. Only at higher frequencies, the pump rate from a higher number of inlet and outlet valves surpasses the pump rate from lower numbers of inlet and outlet valves. This can be explained by the pressure within the pump chamber. The pressure created at a certain frequency is distributed to the number of valves. For a larger number of valves the frequency needs to be high to build up a pressure that gives a reasonable difference between diffuser and nozzle flow.

The micropump has been designed so that the novel mass fabrication technique for the membrane actuator developed by Koch [Koch00] can be used. To employ the thick-film screen printing technology an even surface is required. This is the first time that a gas/liquid micropump has been presented, which is tolerant towards gas bubbles, is self-aligning and has the possibility of employing mass fabrication of the piezoelectric membrane actuator.

A novel fabrication process has been described enabling the self-alignment of the membrane unit to the valve unit. Also the fabrication of the passive dynamic valves and the actuated membrane was explained. Both, valve unit and membrane unit are fabricated in 4 inch <100> oriented silicon wafers enabling cheap mass production.

Simulations of the pump rates and backpressures have been done. The membrane displacement due to piezoelectric actuation has been measured with a laser interferometer and showed very good agreement with ANSYS 5.4 simulations and analytical calculations. A pump rate of 1500 µl/min was obtained for ethanol as pump medium at a frequency of 2.5 kHz and a voltage of 190 V_{pp}. Under the same conditions, a backpressure of 1000 Pa was achieved. The pump showed tolerance towards gas bubbles of approximately 14 µl in size. Gas pumping was achieved at a frequency of 3.4 kHz and an actuation voltage of 300 V_{pp} resulting in a pump rate of around 700 µl/min.

CHAPTER 4

Micromachined Flow Sensor

4.1. Introduction

A micromachined flow sensor to measure and control the microlitre per minute output from the micropump is desirable. This degree of control of the pump rate would enable a dosing system and a micromachined chemical reaction system consisting of two pumps, two flowsensors and a mixing chamber (characterised by Koch [Koch98c]). A schematic of the flow sensor can be seen in figure 4.1.

The initial design and fabrication of a flow sensor based on the thermal principle as described in chapter 2.2.2 has been done by a previous PhD student [Koch97b]. However, due to technological problems during the fabrication, no working flowsensor was obtained. The design layout and the fabrication process had to be changed for a successful implementation. The original technological problems and the obtained solutions are described in the design and fabrication section in this chapter. Before that, in section two, the measurement principle is described and in section four simulations have been carried out to predict the behaviour of the sensors. Measurements and comparisons to the simulation are described in section five and conclusions are drawn in section six.

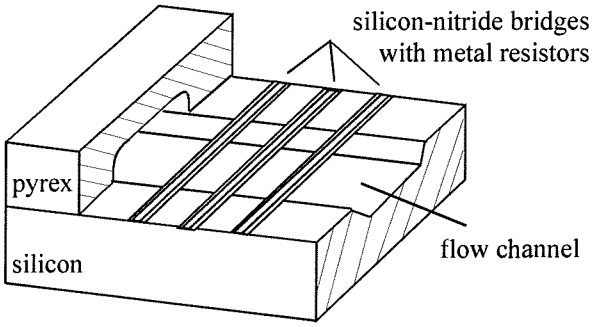

Figure 4.1: Schematic of the thermal flow sensor.

4.2. Measurement Principle of the Flow Sensor

Figure 4.2 illustrates the principle of the flow sensor. As mentioned before, most flow sensors described so far in the literature work in the thermal domain. Convection cools a heater and disturbs the temperature distribution close to the heater. With the micromachined flow sensor realised during this work, several flow sensing techniques are feasible.

Three resistors are located in the middle of the flow channel. Heat is dissipated in the middle resistor called the heater (H). The resulting temperature distribution is sensed with two temperature sensitive resistors T_1 and T_2 symmetrically located near the heater. One resistor is located upstream relative to the heater and one resistor is located downstream. The heater as well as the sensing resistors are located on supporting beams which cross the flow channel in the x-y plane. This method of operation is termed the constant power mode. Other modes of operation are possible. Using the constant temperature mode or constant current mode, only one of the resistors is used. For the time of flight mode, the heater and one of the temperature sensitive resistors is used. Bi-directional flow can be measured using the constant power or the time of flight mode.

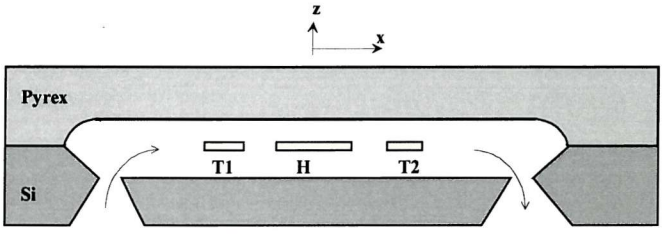

Figure 4.2: Schematic cross section of the flow sensor.

4.3 Design and Fabrication of the Flow Sensor

The severest problem with the initial fabrication was the high stress in the nitride layer supporting the heater and sensor resistors in the middle of the flow channel. This high stress resulted in the breaking of the beams crossing the flow channel. No low stress nitride process was available in the facilities at the Microelectronics Centre. Therefore, a test batch had to be developed, which is described in 4.3.1. In addition, supporting beams on the edges of the grid were implemented. This is explained in 4.3.2. Also during the initial fabrication, alignment problems were experienced. The metal resistor layer, which is on top of the nitride grid, was often misaligned resulting in an interruption in the resistor leads. Widening the underlying nitride beam structure, also described in 4.3.2, solved this problem.

The chip has a width of 4 mm and a length of 7.5 mm. The length of the flow channel running between the inlet and outlet is 2.1 mm and the width of the flow channel is 280 μm or 580 μm. The sensor has been designed so that it is simple to integrate with other micro-liquid handling components such as pumps and mixers. The inlet and outlet are on the back of the

chip with a silicon backplane so that it can be anodically bonded onto the microfluidic circuitboard described in chapter 5.

4.3.1 Low-stress nitride

Three techniques for the creation of low stress nitride are known. By altering the RF frequency during the deposition of PECVD (plasma enhanced chemical vapour deposition) silicon nitride the stress within the layer can be altered from tensile to compressive [Claa85]. However, this technique needs equipment, in which the frequencies can be altered. This was not available within the facilities of the Microelectronics Centre's cleanroom. The PECVD silicon nitride layer obtained from the machine settings in the cleanroom was tested for stress by applying the nitride etch mask used for the creation of suspended bridges over the flow channel. It was shown to have high tensile stress as all bridges were broken with the silicon nitride curled up.

The other two techniques use a LPCVD (low pressure chemical vapour deposition) furnace. One is termed 'silicon-rich-nitride' and the other 'oxy-nitride'. In both cases, the gas flow rates during the deposition are changed resulting in different layer compositions. Silicon-rich-nitride is deposited using dichlorsilane and ammonia. Oxy-nitride is deposited using dichlorsilane, ammonia and nitrous oxide.

The test batch included silicon-rich-nitride $Si_{3+x}N_{4-y}$ and oxi-nitride $Si_xN_yO_z$ in various gas ratios during deposition and standard nitride Si_3N_4 as a reference. The deposition temperature for all nitrides was 740 degC.

In table 4.1 the flow ratios of the gases and the particular gas flow rates, the pressure within the furnace and the deposition times are listed. The number column refers to the different wafers.

The following abbreviations have been used in tables 4.1 and 4.2:

No.	number of wafer
$\phi_{SiH2Cl2}$	flow rate of dichlorsilane - SiH_2Cl_2
ϕ_{NH3}	flow rate of ammonia – NH_3
ϕ_{N2O}	flow rate nitrous oxide – N_2O
p_f	pressure within furnace
t_{dep}	deposition time
R_{avg}	average deposition rate
avg.	average
sccm	standard cubic centimetre, 1 sccm = $1 \cdot 10^{-3}$ litre
λ	wavelength of light
Å	Angstroem, 1 Å = $1 \cdot 10^{-10}$ m

standard nitride						
No.	SiH_2Cl_2:NH_3	$\phi_{SiH2Cl2}$ [sccm]	ϕ_{NH3} [sccm]	ϕ_{N2O} [sccm]	p_f [mbar]	t_{dep} [min]
1	1:4	25	100	-	0.29	67
silicon-rich nitride						
No.	SiH_2Cl_2:NH_3	$\phi_{SiH2Cl2}$ [sccm]	ϕ_{NH3} [sccm]	ϕ_{N2O} [sccm]	p_f [mbar]	t_{dep} [min]
2	4:1	182	45	-	0.29	52
3	6:1	182	30	-	0.29	52
4	8.6:1	172	20	-	0.34	104
5	8.4:1	168	20	-	0.34	53
6	8.4:1	168	20	-	0.34	95
oxy-nitride						
No.	SiH_2Cl_2:NH_3:N_2O	$\phi_{SiH2Cl2}$ [sccm]	ϕ_{NH3} [sccm]	ϕ_{N2O} [sccm]	p_f [mbar]	t_{dep} [min]
7	1:1.3:1.8	38	49	68	0.31	96
8	1:1.3:2	38	49	76	0.31	96
9	1:1.3:2.2	38	49	82	0.31	96

Table 4.1: Process conditions for low-stress nitride test batch.

standard nitride									
No.	thickness [Å]				refractive index at λ = 630 nm				R_{avg} [Å/min]
	flat	middle	curve	average	flat	middle	curve	avg.	
1	1534.67	1495.52	1502.27	1510.82	2.021	2.025	2.023	2.023	22.9
silicon-rich nitride									
No.	thickness [Å]				refractive index at λ = 630 nm				R_{avg} [Å/min]
	flat	middle	curve	average	flat	middle	curve	avg.	
2	1481.04	1447.52	1434.32	1454.29	2.153	2.152	2.152	2.152	28.0
3	1286.65	1263.99	1245.17	1265.27	2.227	2.229	2.231	2.229	24.3
4	2097.90	2080.30	2179.93	2119.38	2.344	2.380	2.337	2.354	20.4
5	1253.37	1172.77	1164.38	1196.84	2.353	2.333	2.333	2.340	22.6
6	2303.35	2131.55	2110.59	2181.80	2.306	2.313	2.314	2.311	23.0
oxy-nitride									
No.	thickness [Å]				refractive index at λ = 630 nm				R_{avg} [Å/min]
	flat	middle	curve	average	flat	middle	curve	avg.	
7	1615.16	1591.31	1594.67	1600.36	1.933	1.939	1.937	1.936	16.7
8	1559.62	1539.45	1531.72	1543.60	1.928	1.932	1.938	1.933	16.1
9	1507.43	1489.75	1485.54	1494.22	1.932	1.937	1.939	1.936	15.6

Table 4.2: Measurement results obtained from ellipsometer.

The test batch was evaluated by first characterising the different layers using an ellipsometer. Table 4.2 shows the measurement results obtained for the layer thicknesses and the refractive indices. Measuring at three locations on the wafer specified the uniformity and then the average thickness and refractive index respectively were calculated. The average deposition rate was obtained by dividing the average thickness by the deposition time given in table 4.1.

The results from table 4.2 show that the refractive index of standard nitride is similar to that found in reference books (table 4.3). Within silicon-rich-nitride the refractive index increased with increasing flow rate ratio of dichlorsilane to ammonia (SiH_2Cl_2:NH_3). Varying the flow rates for the oxy-nitride deposition had no influence on the refractive index. It can also be seen that the thickness of the nitride film varies across the wafer for all deposition conditions. However, for flow sensor applications this non-uniformity has no influence on the sensor's performance and therefore is not studied further.

The refractive index of oxy-nitride, which is less than that of silicon-nitride, can be explained by the low refractive index of silicon dioxide (table 4.3) as the oxy-nitride film is a mixture of silicon nitride and silicon dioxide. The increasing refractive index of silicon-rich-nitride is due to the increasing amount of silicon, which has a high refractive index (table 4.3), within the deposited layer.

	wavelength [nm]	refractive index
silicon	633	3.415
silicon dioxide	644	1.457
standard silicon nitride	620	2.022

Table 4.3: Refractive index of various materials [Pali85].

An extensive study on LPCVD silicon-rich nitride films has been done by Gardeniers [Gard96]. The study suggests that low-stress nitride is obtained at a refractive index around n=2.3. Table 4.4 shows the relationship between the refractive index and the stress within the thin film.

refractive index	σ [MPa]
2.033	1190±90
2.204	680±170
2.335	60±50
2.542	-160±140

Table 4.4: Relationship between the refractive index and the stress within silicon-rich nitride films [Gard96].

It can be seen from table 4.4 that the tensile stress within the nitride layer decreases with increasing refractive index. Even compressive stress can be created with high flow ratios of SiH_2Cl_2:NH_3 giving a high refractive index. The maximum achievable flow ratio of SiH_2Cl_2:NH_3 with the furnace used was 8.6:1 resulting in a refractive index of 2.354. This number suggests that a low-stress nitride film can be obtained.

To verify this assumption, wafers with standard silicon-nitride, oxy-nitride and silicon-rich-nitride were patterned using the mask that was used to create the suspended nitride grid over the flow channel by wet etching in KOH. This experiment showed that all the bridges using standard silicon-nitride were broken. About 40% of the bridges using oxy-nitride were intact after the KOH etch. The wafer using the high refractive index silicon-rich-nitride yielded 99% of the bridges intact. It can therefore be concluded that the silicon-rich-nitride deposited using a flow ratio SiH_2Cl_2:NH_3 of 8.6:1 is low stress and hence this is to be used for the fabrication of the flow sensors.

4.3.2 Optimisation of nitride grid

To optimise the suspended nitride grid the beams were widened to avoid misalignment and hence interruption of the deposited metal resistors. The nitride bridges were arranged at an angle over the flow channel. This angle is necessary for the underetching of the nitride grid in KOH solution. A mask opening at an angle to the flat will result in a rectangle perpendicular to the flat as can be seen in figure 4.3. This is due to the crystal orientation within the bulk silicon. By creating or changing the layout for the nitride grid, the mask openings must be designed so that the resulting rectangles overlap each other (figure 4.4). Thereby, the whole structure will be underetched creating the suspended nitride beams.

In order to increase the stability of the nitride grid, supporting beams were added at each end. Figure 4.5 shows the layout for the wide channel (580 μm) and figure 4.6 shows the layout for the narrow channel (280 μm).

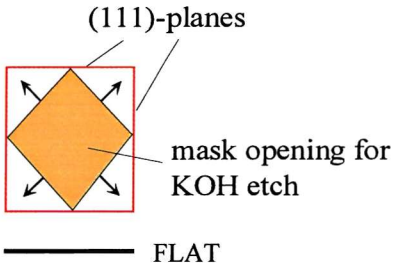

Figure 4.3: Schematic of KOH etch progress.

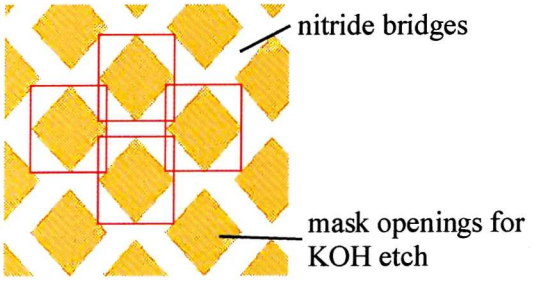

Figure 4.4: Schematic for the creation of a suspended nitride grid.

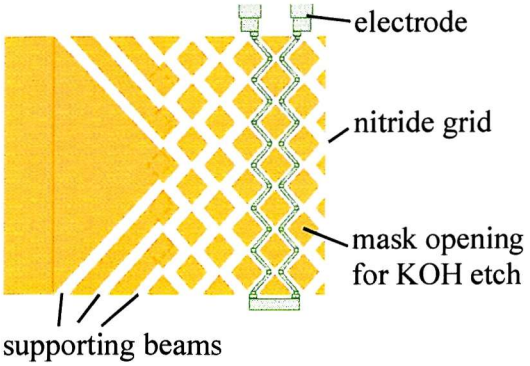

Figure 4.5: Supporting beams for wide channel.

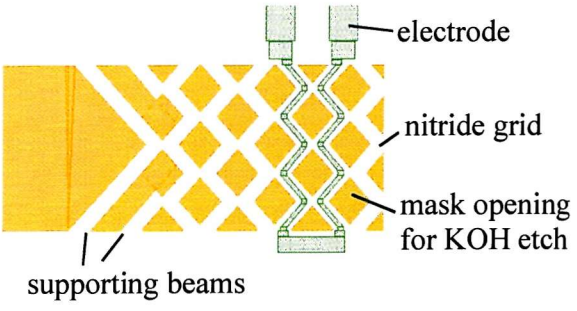

Figure 4.6: Supporting beams for narrow channel.

4.3.3 Micromachining

The flow sensor was fabricated on 100 mm (100) double sided polished silicon wafers. In the first stage, double-sided alignment features had to be created. In part I, the silicon wafers were cleaned in fuming nitric acid for 10 min. After the photolithography on the fronts (backs protected), using Shipley SPRT511 resist, alignment marks were etched using a dry etching process 1μm deep into the silicon with SF_6 as the reaction gas. The resist was stripped off by ashing in an oxygen plasma. The second lithography mask was aligned to the previously etched marks on the front side. For this, an infrared camera was used to look through the wafer. After exposing and developing, alignment marks for the back were etched, also, 1 μm deep using the same dry etch process. Again, the resist was removed form the wafers by ashing.

After RCA-cleaning, silicon-rich-nitride (SiH_2Cl_2:NH_3 ≡ 8.6:1) was deposited by low pressure chemical vapour deposition (LPCVD). This layer serves as the etch mask during subsequent wet silicon etches using potassium hydroxide (KOH) and as a supporting mesh for the sensor resistors.

The next stage was to create the supply holes into the back of the wafer. Shipley SPRT511 resist, patterned by a standard photolithography process, was the mask for the dry etch process to pattern the nitride. The reactive gases used were CHF_3 and argon. The resist was removed by ashing. Next followed a dip etch of the wafers into 20:1 buffered hydrofluoric acid (BHF) in order to remove the native oxide and thereby get a more homogenous etch result. Immediately after rinsing, the wafers were immersed into 30% KOH at 70 degC. The etching rate for these conditions is 0.54 μm/min. The supply holes were etched 400 μm deep into the 500 μm thick wafers (figure 4.7a).

In the metallization stage the resistors and contact pads were created. After a fuming nitric acid clean 30 nm chromium and 200 nm gold were evaporated onto the fronts of the wafers. During the photolithography Shipley S1818 resist was used as SPRT511 does not adhere well to gold. The metal layers were patterned using a gold etchant (potassium iodide) and chromium etch (22% ceric ammonium nitrate and 5% acetic acid), respectively. The resist was stripped using fuming nitric acid (figure 4.7b).

Next the flow channel was created releasing the nitride supporting grid with the metal resistors at the same time. First a fuming nitric acid clean was done. Then, after a standard photolithography process, using Shipley S1818 resist, the nitride was dry etched with CHF_3 and argon as reactive gases. The resist was stripped using an oxygen plasma (figure 4.7c). Again, before the KOH etch, the wafers were dip etched in 20:1 BHF. The flow channels were etched to a depth of 50 μm and the supply holes were etched from the back at the same time (figure 4.7d).

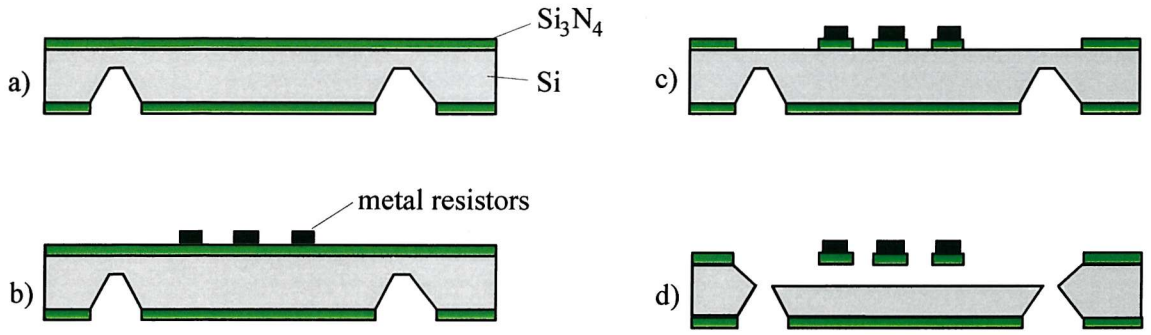

Figure 4.7: Fabrication steps part I for the flow sensor (cross section: length).

Part II of the flow sensor fabrication was the processing of 500 µm thick pyrex wafers, which were used to seal the flow channels. First the wafers were cleaned with fuming nitric acid. Then a chromium/gold layer was evaporated on one side. Chromium, 30 nm thick, was used as an adhesion layer for the gold layer, which is 400 nm thick. After the photolithography using Shipley S1818 resist, the wafers were submerged into the gold and chrome etchants.

The pyrex wafers with the patterned chromium/gold were then exposed to 48 % hydrofluoric acid (HF) to etch 50 µm deep cavities (figure 4.8a). The etch rate was 8 µm/min. During the etch the resist was left on the wafers to prevent pinhole formation. Finally, the resist, gold and chromium was stripped to complete this part of the fabrication process.

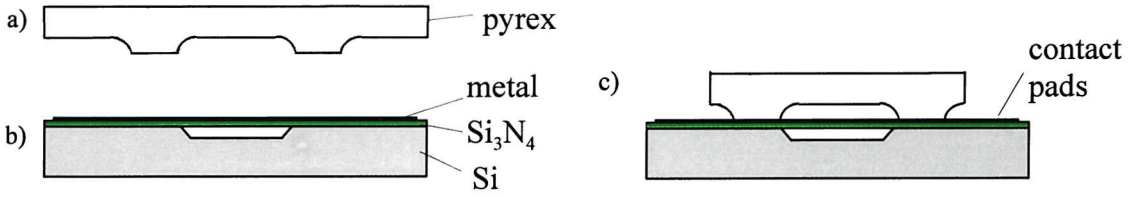

Figure 4.8: Fabrication steps part II and III for the flow sensor (cross section: width).

Part III of the fabrication process was the combination of the pyrex and silicon wafer (figure 4.8a and 4.8b). Anodic bonding was used as the method for achieving a permanent seal. The bonding parameters were 400 degC and 400 Volts applied for 30 min. In addition to the flow channel cavity two cavities were etched on either side of the channel in part II of the fabrication process. The pyrex over these cavities could be sawn away using a standard wafer saw leaving the silicon with the contact pads undamaged (figure 4.8c). The final step was to saw the wafer into single chips of 4 mm x 7.5 mm size.

A photograph of the flow sensor before the pyrex lid bonding can be seen in figure 4.9. The nitride grid with the support beams over a wide channel (580 µm) are shown in figure 4.10. No bending of the grid or the beams was observed. Figure 4.11 shows a SEM picture of the metal resistors aligned on the nitride grid. The design and fabrication alterations made proved to be successful.

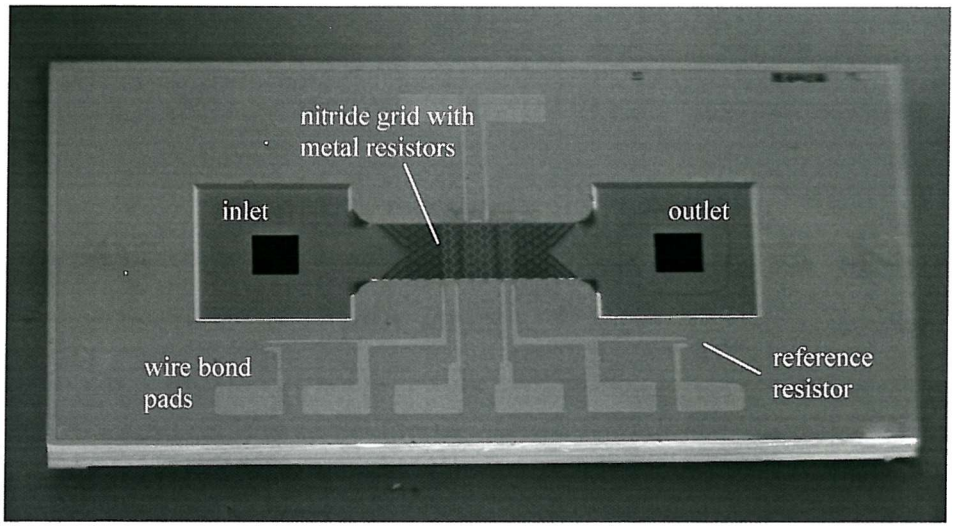

Figure 4.9: SEM picture of a flow sensor with a wide channel prior to lid bonding.

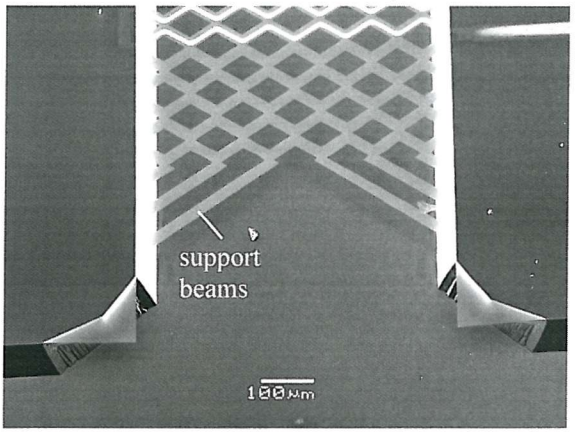

Figure 4.10: SEM picture of nitride grid with support beams over a wide channel (580 µm).

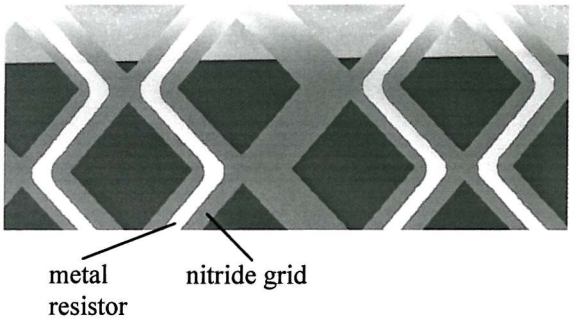

Figure 4.11: SEM picture of the metal resistors on the nitride grid.

4.4 Simulation of the Thermal Flow Sensor

In order to estimate the optimum operating range of the flow sensor, some simulations were done, assuming that the flow sensor was to be operated in the constant power mode (see section 4.2). The whole model is based on lumped elements and simulates the heater and its surrounding. The conductivity to the walls is modelled in a two-dimensional model (y-z plane) and the effect of convection on the temperature distribution is modelled in the x-z plane. The simulations are based on the work of Lammerink [Lamm93]. A schematic of the dimensions of the flow sensor in the x-direction is shown in figure 4.12. Several assumptions were made in order to simplify the analysis:

- The thermal diffusion in the z-direction is much larger than the heat conduction along the bridge.

- The temperature gradient in the z-direction is constant.
- The temperature along the metal bridge in the y-direction is constant.
- The fluid has a laminar flow profile.
- The surrounding walls act as a heat sink (T_w = 0 degC).

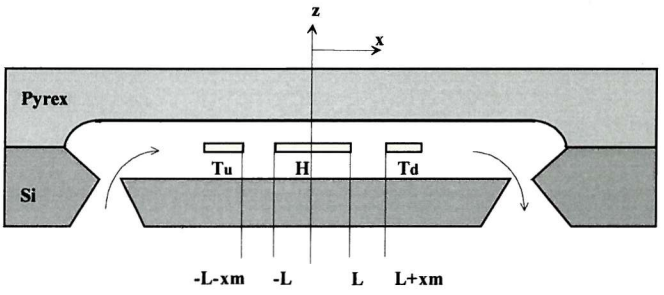

Figure 4.12: Schematic cross section of the flow sensor.

In the steady state, the gradient of the heat current is zero, and the temperature distribution can be written, with the boundary condition $\lim_{x \to \pm\infty} T(x) = 0$, as [Lamm93]:

$$\begin{aligned} x < -L: &\quad T(x) = T_0 \exp(\lambda_1 (x + L)) \\ -L < x < L: &\quad T(x) = T_0 \\ x > L: &\quad T(x) = T_0 \exp(\lambda_2 (x - L)) \end{aligned} \tag{4.1}$$

with the assumptions, that the heater is located between $-L \le x \le L$ and that the temperature is constant throughout the heater ($T = T_0$ for $-L \le x \le L$). λ_1 and λ_2 are given by:

$$\lambda_{1,2} = \frac{1}{2D}\left[v \pm \sqrt{v^2 + \frac{4}{l_z^2} D^2}\right] \tag{4.2}$$

with $D = \frac{\kappa_f}{\rho \cdot c}$ the thermal diffusivity of the liquid.

ρ is the fluid density, c the fluid heat capacity (at constant pressure), v the fluid velocity, κ_f the fluid thermal conductivity and l_z is the distance from the bridge to the channel wall in z direction (total height of the channel is therefore $2l_z$).

The temperature T_0 is given by [Lamm93]:

$$T_0 = \frac{P}{G2L + A\kappa_f (\lambda_1 - \lambda_2)} \text{ with } G = \kappa_f \frac{2l_y}{l_z} \tag{4.3}$$

A is the cross sectional area of the flow channel ($A = l_y \cdot 2l_z$), $2L$ is the heater width, P is the power applied to the heater and l_y is the width of the bridge.

The temperature at the two sensor sides, upstream (at $x = x_m$) and downstream (at $x = -x_m$) and the temperature difference ΔT are given by:

$$T_d = T_0 \exp(\lambda_2 (x_m - L))$$

$$T_u = T_0 \exp(\lambda_1 (-x_m + L)) \qquad (4.4)$$

$$\Delta T = T_d - T_u$$

$$\Delta T = T_0 \{ \exp(\lambda_2 (x_m - L)) - \exp(\lambda_1 (-x_m + L)) \}$$

The dimensions of the device design are: L = 65 µm (1/2 length of the heater), l_y = 280 µm (width of the heater bridge) for the narrow channel and l_y = 580 µm for the wide channel, l_z = 50 µm (distance of heater bridge from top and bottom of the channel), $A = 2 l_y l_z$ (cross sectional area of the channel). The properties of water are taken for the fluid: κ_f = 0.54 W m^{-1} K^{-1} (thermal conductivity), ρ = 998.2 kg m^{-3} (density), c = 4187 J kg^{-1} K^{-1} (specific heat capacity). The temperatures T_u, T_d, ΔT and the heater temperature T_0 are given in figure 4.13 as a function of the volume-flow Q (velocity $v = Q/A$) for the design with the narrow channel (width 280 µm).

Plots of the temperature distribution as a function of both, the volume-flow Q and the position x for a power of P = 50 mW for the narrow channel and P = 100 mW for the wide channel over the heater bridge are given in figures 4.14 and 4.15 for the designs with the narrow and the wide channels, respectively. The volume-flow is varied from 0 µl/min to 100 µl/min in steps of 25 µl/min.

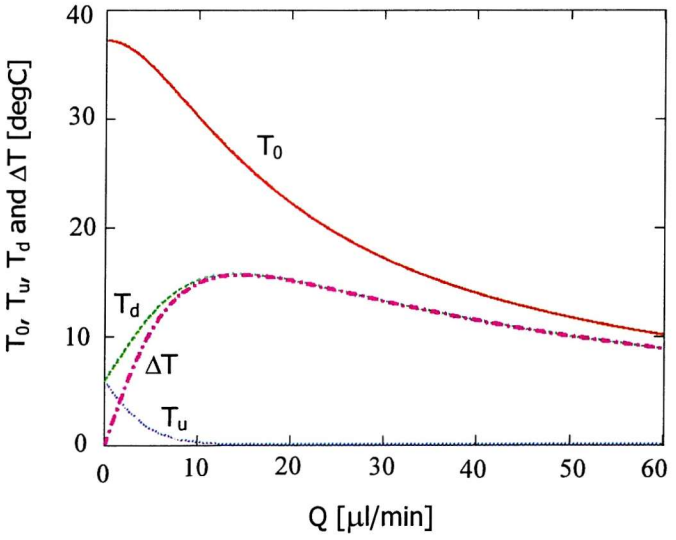

Figure 4.13: Sensor temperatures as functions of the volume-flow Q. T_0 is the heater temperature, T_u and T_d the upstream and downstream sensor temperatures, respectively, and ΔT the temperature difference between T_u and T_d.

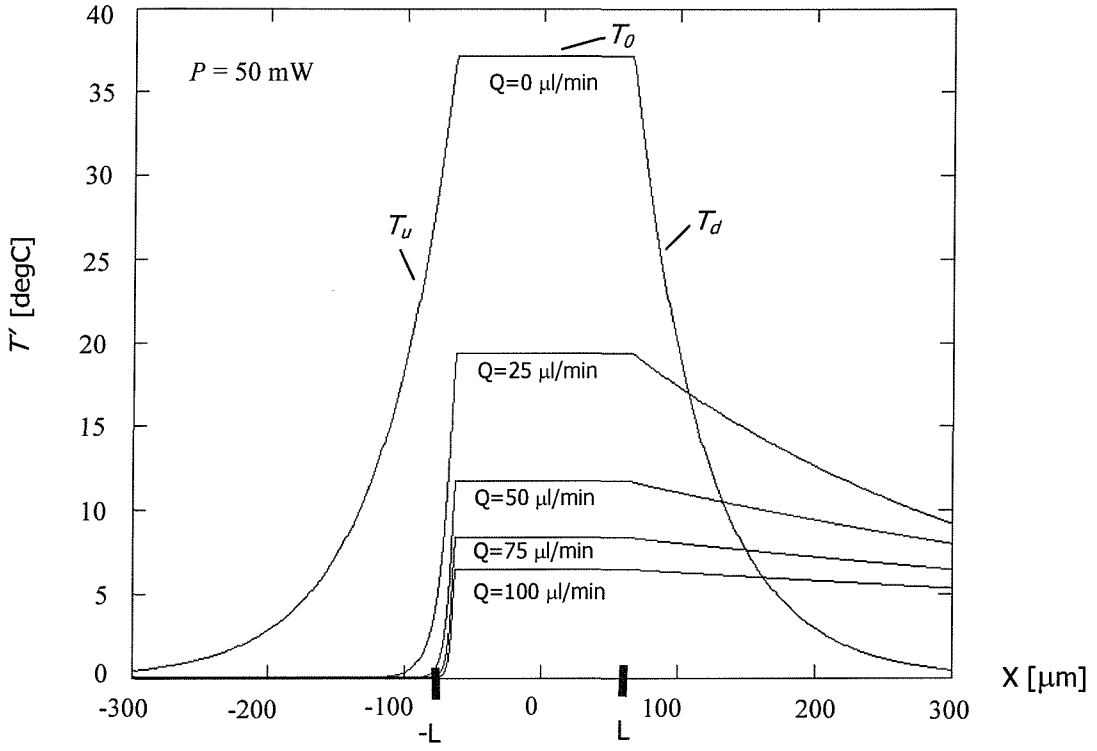

Figure 4.14: Simulation of the temperature distribution T' along the channel for the narrow channel design (width of the bridge 280 µm). $x <$ -L: T_u, -L< x < L: T_0, $x >$ L: T_d.

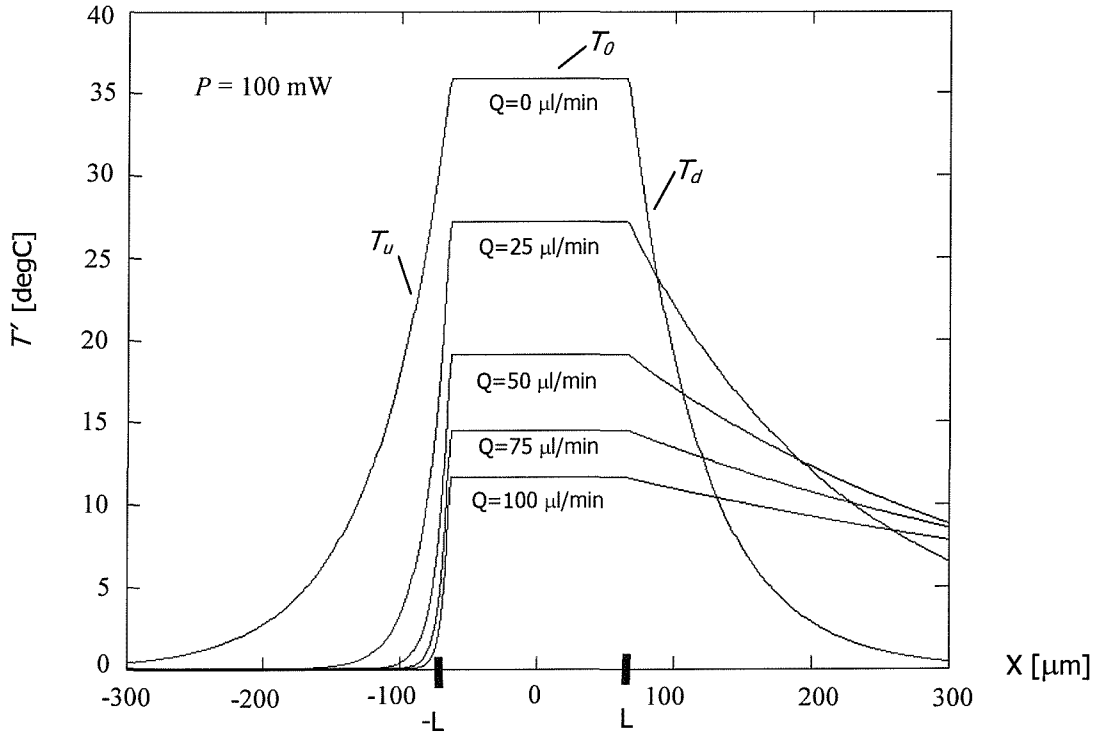

Figure 4.15: Simulation of the temperature distribution T' along the channel for the wide channel design (width of the bridge 580 µm). $x <$ -L: T_u, -L< x < L: T_0, $x >$ L: T_d.

In order to judge the efficiency of the sensor, the temperature difference at the location x_m upstream and downstream of the heater as a function of the volume-flow of the fluid is plotted in figure 4.16 for the narrow channel design and in figure 4.17 for the wide channel design.

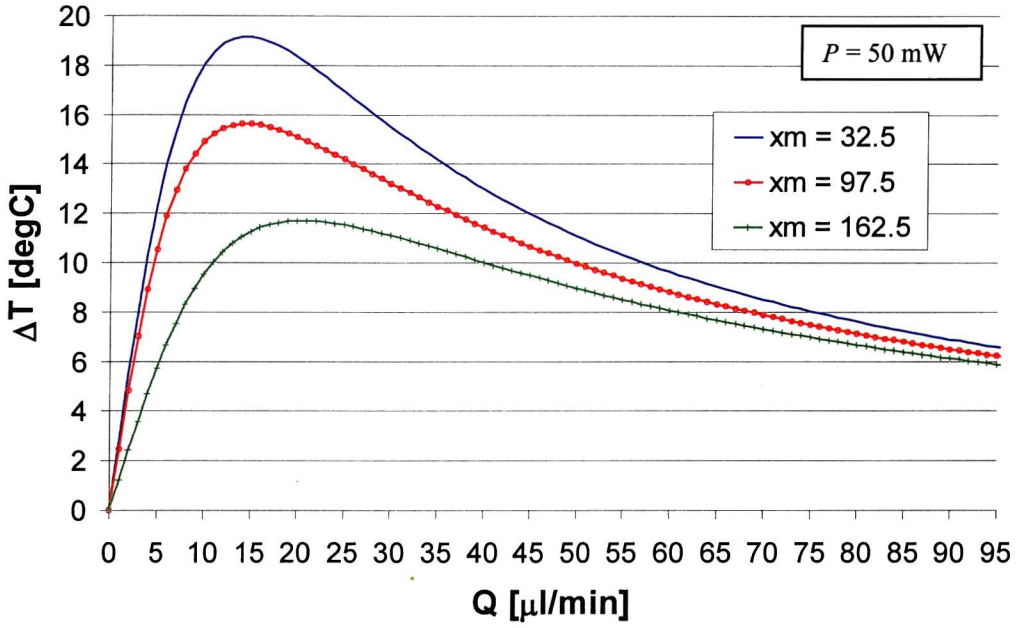

Figure 4.16: Simulated temperature difference of the thermal flow sensor for the narrow channel design (width of the bridge 280 µm). x_m is the distance from sensors to heater.

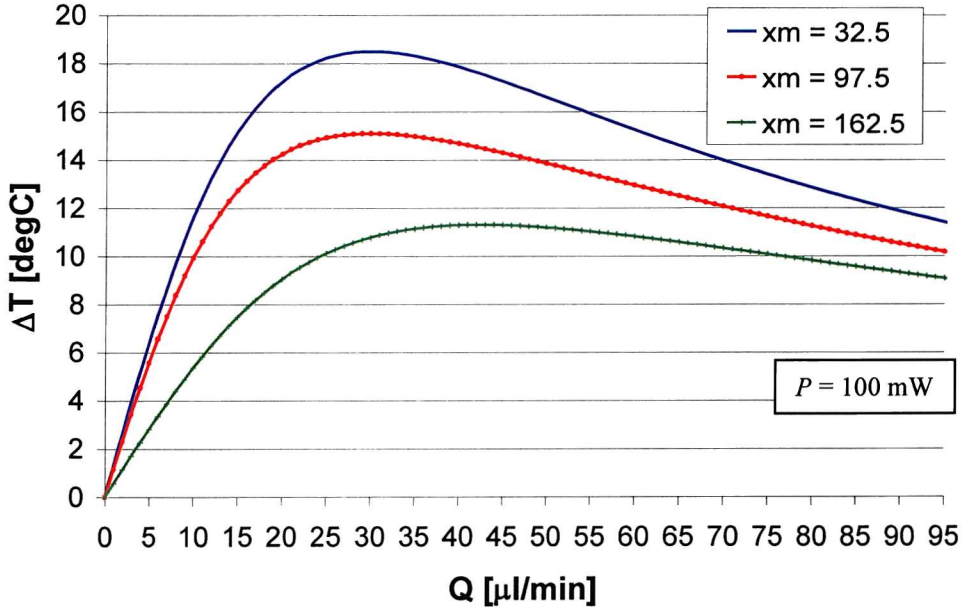

Figure 4.17: Simulated temperature difference of the thermal flow sensor for the wide channel design (width of the bridge 580 µm). x_m is the distance from sensors to heater.

For the narrow channel an almost linear region of the temperature difference is given for volume-flows up to 17 µl/min for x_m = 162.5 µm. For the wide channel an almost linear region of the temperature difference is given for volume-flows up to 30 µl/min for x_m = 162.5 µm. It is desirable to operate the flow sensors in these linear regions. Therefore the volume-flow has to be taken into account in choosing the sensor design and in choosing the distance x_m from the sensors to the heater.

The temperature sensors are created in the same way as the heater, except, that the current through the wires is supposed to be much less than for the heater. The electrical resistance of a metal is dependent on its temperature: $R = R_0 \cdot (1 + \alpha \cdot \Delta T)$, with α as the temperature coefficient. Therefore, a measurement of the resistance can be used to measure the temperature. The temperature coefficients of some common metals used in micromachining are given in table 4.5.

material	temperature coefficient [10^{-3} K^{-1}]
Ti	5.5
Pt	3.93
Au	3.4

Table 4.5: Specific electrical resistance and temperature coefficients for Ti, Pt, Au [Stoe93, Weas89].

4.5 Measurements and Comparison to Simulations

4.5.1 Temperature Coefficient

To evaluate the temperature coefficient of the heater/sensor resistors, the flow sensor chip was placed in a temperature controlled oven and the change in resistance was observed. The measurement results (figure 4.18) show a linear relationship between the temperature and the resistance. For a temperature change of 140 degC, the resistance changes by 12 Ohm. The temperature coefficient is given by [Stoe93]:

$$\alpha = \frac{\frac{\Delta R}{R}}{\Delta T} \tag{4.5}$$

With the data from figure 4.18, a temperature coefficient of α = 0.13·10^{-3} K^{-1} was calculated. The temperature coefficient for bulk gold is α = 3.4·10^{-3} K^{-1} [Weas89]. The resistance changed by a factor of 6 after the anodic bonding, a process in which the metal film is heated to 400 degC. The measured temperature coefficient before anodic bonding was α = 2.1·10^{-3} K^{-1}. A similar effect has been reported by Lammerink [Lamm93], where the resistance of chromium/gold resistors increased by a factor of 20 after the anodic bonding process (bonding temperature 450 degC).

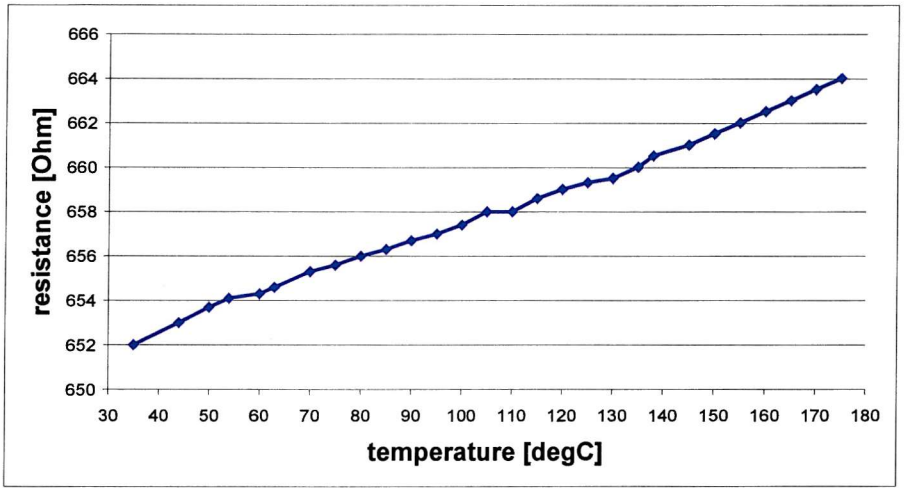

Figure 4.18: Measurement of resistance versus temperature.

4.5.2 Flow Measurements

The flow sensor was tested using a jig manufactured from Perspex (figure 4.19 and 4.20). Two metal pipes of 3 mm outer diameter, on which plastic hoses could be connected, were inserted on opposite sides into drilled holes. Another set of holes (1 mm diameter) was drilled perpendicularly from the top of the Perspex dice. The test jig is 12 mm wide, 7.5 mm long and 10 mm high. The block has a 2 mm recess on either side for ceramic strips containing wire bond pads to be glued. A flow sensor with a narrow channel (280 µm) was mounted on top of the Perspex block using Cyanoacrylate adhesive. A photograph of the test setup can be seen in figure 4.21.

A flow injection analysis (FIA) instrument from Laboratoriumstechnik, Zuerich, Switzerland was connected to the test jig. The FIA can be regulated from 1 µl to 99 µl in 1 µl increments. De-ionised water was used as test liquid.

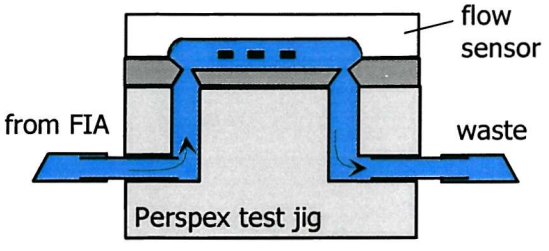

Figure 4.19: Measurement setup for the flow sensor test – cross sectional front view.

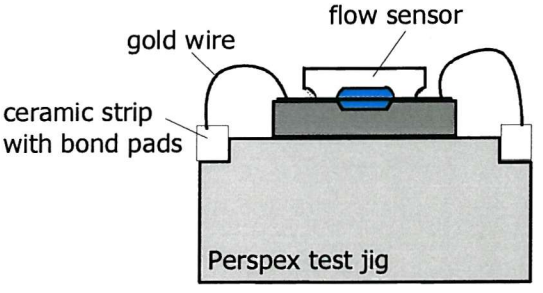

Figure 4.20: Measurement setup for the flow sensor test – cross sectional side view.

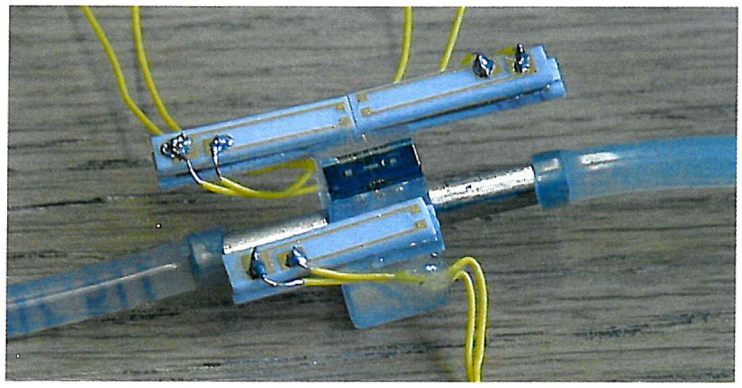

Figure 4.21: Photograph of the test setup.

Once the test jig had been filled with water, the heater resistor was connected to a constant current source and the voltage was measured with a digital multimeter from which the resistance change could be calculated. When the flow rate on the FIA was altered the voltage across the resistor changed due to a temperature change of the resistor. The measurement results are given in figure 4.22 for constant currents of 6.34 mA, 9.12 mA and 11.38 mA applied to the chromium/gold resistor suspended over the flow channel. This constant current measurement, as also described by [Mull95], was intended to show the functionality of the flow sensor after the successful fabrication. The advantage of this measurement method is that no electrical circuit was necessary to read the output of the sensor. The resistance of the heater was measured before the experiment had started with a current of 0.99 mA (no heating) and no flow within the channel.

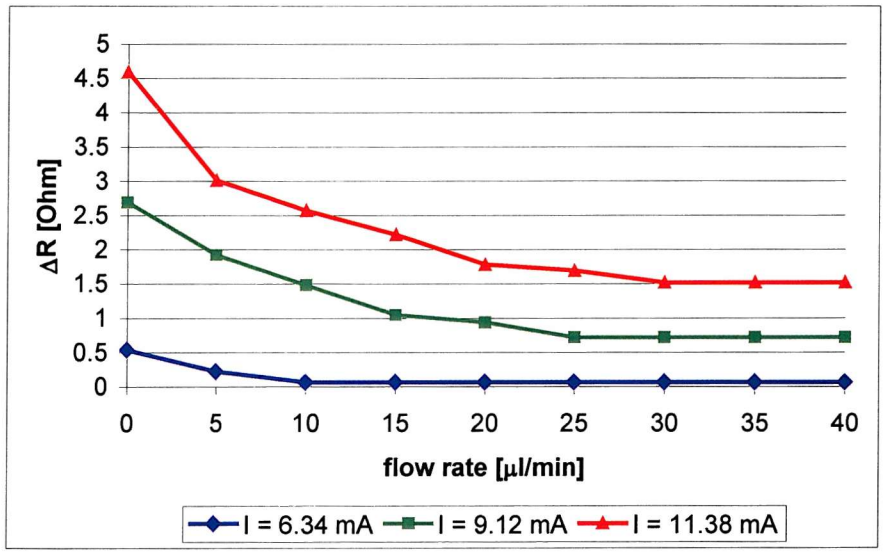

Figure 4.22: Measurement results for constant current mode.

The measurements show that for higher currents the resistance change is larger, as expected. With increasing flow rate, the resistance drops until it reaches a point where higher flow rates do not result in a further decrease of the resistance. With a constant current of 11.38 mA a flow of up to 30 µl/min could be measured. It can also be seen that the resistance

levels at a certain value above the initial resistance value measured without heating and no flow within the channel. The system reaches an equilibrium between the heating effect due to the current through the resistor and the cooling effect due to the water flow within the channel.

4.5.3 Comparison of Measurement Results to Simulations

In section 4.4, the temperature T_0 of the heater resistor is given for varying flow rates. Equation 4.3 was used to calculate the temperature T_0 for a constant power. For the constant current mode, the current stays constant and the resistance changes. Therefore, the power changes as the resistance changes. However, the equation can be used, as the power change ΔP is very small over the current and flow rate values used (table 4.6). ΔP was calculated as the difference between the power at 0 µl/min and at 40 µl/min flow rate for a constant current. For the given resistor and current values, the power has been calculated for each of the simulations: $P = I^2 \cdot R$, with $R = \Delta R + R_0$; R_0=266.5 Ω (table 4.6). The temperature changes obtained from the simulations (equation 4.3) are converted to resistance changes with the data obtained from figure 4.18: $\Delta R = \Delta T \cdot 0.0857\ \Omega\ K^{-1}$. ΔT is the difference between T_0 ($P \neq 0$) and T_0 ($P = 0$). The measurements are compared to the simulation results in figure 4.23.

I [mA]	6.34	9.12	11.38
P [mW]	10.7	22.3	34.9
ΔP [mW]	0.02	0.16	0.40

Table 4.6: Power equivalent to current used to heat the sensing resistor.

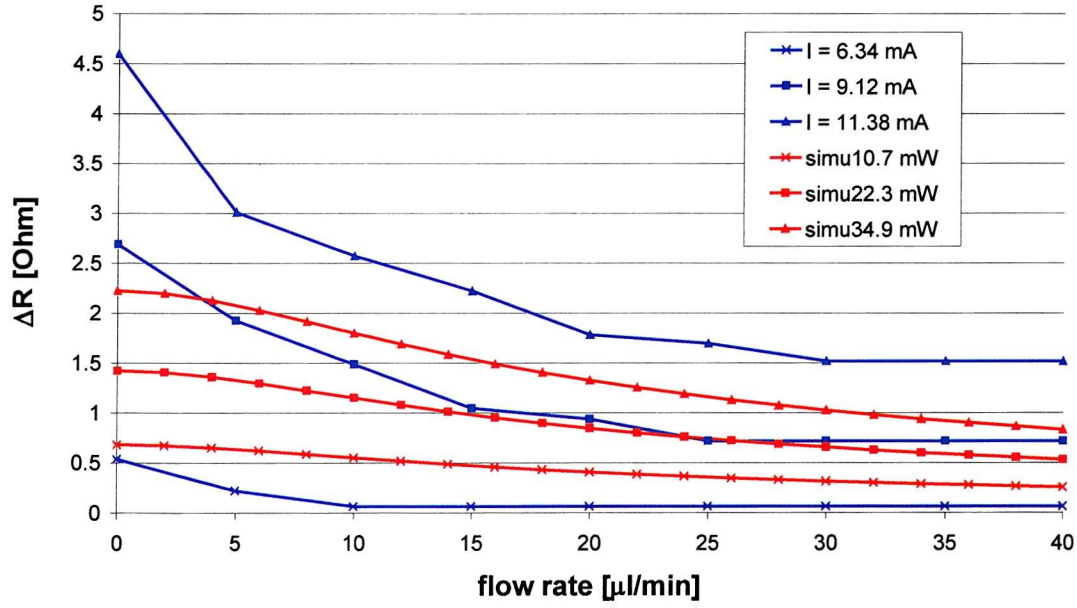

Figure 4.23: Simulation results compared to measurement results. The blue curves are measured, the red curves are simulated. The curves with the equivalent line markers belong together.

When 6.34 mA current was applied, the resistor heated up to almost the same value as that simulated at zero flow rate. For increasing flow rate, the resistance value dropped faster than the simulated value and levelled out at a value below the simulated one. For the other two measurements, the resistor heated above the simulated value at zero flow rate and also dropped faster than the simulated values. For the 9.12 mA current, the measured value levels out close to the simulated values and for the 11.38 mA current the measured value levels out at a higher value than the simulated value for large flow rates.

Several assumptions were made for the simulation: the thermal diffusion in the z-direction is much larger than the heat conduction along the bridge, the thermal diffusion in the z-direction is linear, the temperature along the metal bridge in the y-direction is constant, the fluid has a laminar flow profile and the silicon/pyrex acts as a heat sink staying at constant temperature. During the measurements, the flow sensor chip was not connected to a heat sink, but to a Perspex block whose thermal conductivity is very low. Therefore, the whole chip would have heated up during the measurements. This explains the higher resistance values for the 9.12 mA and 11.38 mA measurements. The faster cooling of the measured values compared to the simulated values can also be explained by the flow sensor chip not acting as a heat sink. After the current was switched on, the chip was left for a certain amount of time until the resistance value had settled. During this time, the silicon/pyrex heated up as well and when the flow was switched on, the sensor resistor and also the chip were cooled down by the water.

This experiment proved the functionality of the flow sensor and hence successful fabrication.

4.6 Conclusion

In this chapter, a flow sensor based on the work of Lammerink [Lamm93] and Koch [Koch97b] has been presented. The technological problems for the realisation of the sensor have been overcome. The design of the nitride supporting grid has been altered and low stress nitride was implemented. To obtain low stress nitride, a test batch was processed with various conditions for the nitride deposition. The best result was obtained with dichlorsilane and ammonia as deposition gases at a gas flow ratio of 8.6:1.

The complete micromachining process to realise flow sensors has been described. The flow sensors can be implemented into microfluidic systems as described in chapter 5. Measurements with the constant current mode have been carried out and they show that the flow sensor was fabricated successfully and that it can be used for monitoring flow rates.

CHAPTER 5

Microfluidic Circuitboard

5.1 Introduction

Many discrete microfluidic devices have been characterised. However, integration into complete systems is not very common. One aim of this thesis was to create a microfluidic interconnection technology. In accordance with the printed circuitboard in electronics, a similar approach for fluidic devices is desirable. Such novel microfluidic circuitboards should allow discrete devices to be mounted in various independent configurations, forming complete systems.

In this chapter, a technology for achieving this goal of integrated microfluidic systems is described. The basic principle for fluidic interconnection of a system realised on a microfluidic circuitboard is shown in figure 5.1.

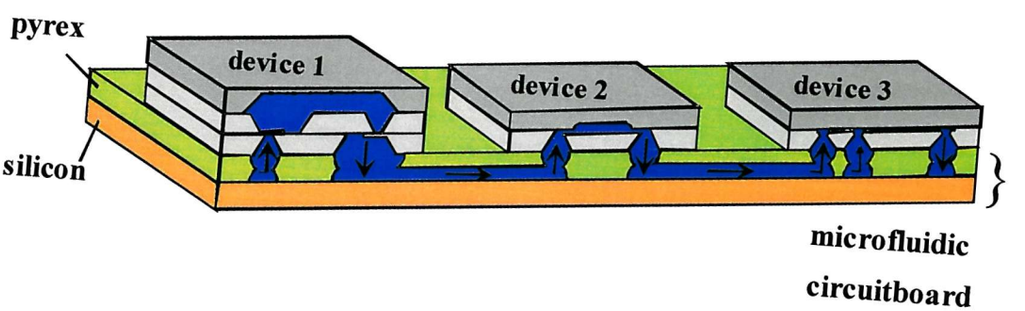

Figure 5.1: Schematic of the microfluidic circuitboard.

The microfluidic circuitboard consists of a double layer of silicon and pyrex, joined by anodic bonding, with the fluidic channels running between. It conducts the fluid from one device to the next without the need for intermediate macroscopic connections. A great advantage of such a system is its applicability to many fluidic problems due to its versatility. To realise other systems only the mask layout for creating the channels in the pyrex wafer has to be changed. So, various microfluidic systems can be easily fabricated and with no limit of either number or

kinds of devices. The fabrication technology is not demanding and would allow a simple way of mass fabrication.

Such a system could be a microplant where chemical reactions can be carried out on demand, a drug delivery system or a particle analysis system for counting, sizing and sorting of particles and/or cells.

The connection to the devices is through holes in the pyrex. As all the discrete microfluidic devices developed by our group like pumps, mixers, etc. have a bottom silicon layer, anodic bonding to the circuit board can guarantee a leak free contact. Other designs of a fluidic circuitboard have been proposed by Lammerink [Lamm96] and Richter [Rich97] but both of them were fixing the discrete devices to their interconnection board with adhesive. Richter developed a circuitboard where the channels and through holes are etched into silicon with a pyrex backplane. Nevertheless, the discrete microfluidic devices had to be glued onto the silicon as anodic bonding was not possible. Lammerink fabricated an epoxy board containing the channels and through holes, which is attached to a transparent polycarbonate substrate.

First, the layout of the fluidic circuitboard is explained. After that, the technology, which is mainly based on deep etching of pyrex with 48% hydrofluoric acid (HF) and the anodic bonding method, is presented. The whole process requires just four lithography masks of which two only require coarse alignment. The testing of the fluidic circuitboard is then described and the chapter ends with a conclusion.

5.2 Layout of the Microfluidic Circuitboard

The design of the fluidic board is based on two requirements. First, it should connect the discrete fluidic devices and second, there should be very little pressure drop within the channels. The depth of the channels (250 μm) is defined by the thickness of the pyrex wafer (500 μm) as supply holes and channels are etched from both sides of the wafer at the same time. Furthermore, the dimensions of the supply holes and the length of the channels are defined by the in/out-lets of the fluidic devices to be bonded on top of the circuitboard. Therefore the width of the channels has to be chosen to give low pressure drops, as there are high pressure drops (in the kPa range) within some microfluidic devices that might be mounted on the board. The length of the flow channels varies between 3 mm to 6 mm due to the dimensions of the devices to be mounted on top. Hence, the width has been chosen to be between 2 mm and 3 mm.

To determine the pressure drop the flow pattern has to be evaluated first. Therefore, in order to determine whether the flow pattern is laminar or turbulent, it is common practice to calculate the Reynolds number and compare it to the transitional number 2300. If the calculated number is under this transitional number, the flow is considered to be laminar. The Reynolds number R_e is given by [Grav93]:

$$R_e = \frac{\rho}{\mu} \cdot v \cdot D_h \tag{5.1}$$

$$D_h = 4 \cdot \frac{\text{cross sectional area of channel}}{\text{circumference of channel}} \tag{5.2}$$

where ρ, μ, v, and D_h are the density (ρ = 998.2 kg m^{-3} for water), dynamic viscosity (μ = $1.005 \cdot 10^{-3}$ N s m^{-2} for water), velocity and hydraulic diameter, respectively.

The Reynolds number is calculated with the parameters given above for a volume flow of Q = 100 µl/min ($v = Q/A$). The channel, which is expected to give the lowest pressure drop has dimensions of 3 mm x 3 mm x 250 µm and a Reynolds number of R_e = 1.0 and the channel with the highest expected pressure drop has dimensions of 2 mm x 6 mm x 250 µm and a Reynolds number of R_e = 1.5. Hence, it can be concluded that all the channels within the microfluidic circuitboard have truly laminar flow.

To calculate the pressure drop the following formula for laminar flow patterns was used [Grav93]:

$$\Delta p = Q \cdot C_{fr} \cdot L_{ch} \frac{\mu}{2 \cdot A \cdot D_h^2} \tag{5.3}$$

L_{ch} is the length of the channel, Q is the volume flow, A is the cross sectional area of the flow and C_{fr} is the friction coefficient (C_{fr} = 96 for a rectangular cross section, where the width is much larger than the height).

For a volume flow of 100 µl/min, the pressure drop for the 3 mm x 3 mm x 250 µm channel is Δp = 1.5 Pa and for the 2 mm x 6 mm x 250 µm channel the pressure drop is Δp = 4.9 Pa. Therefore the pressure drop within the circuitboard is negligible compared to the maximum backpressure of 1 kPa, which the micropump can pump against.

HF is an isotropic etch and so the shape of the channel cross-section is not exactly rectangular. But this adds no significant extra impedance to the flow because of the large dimensions used. Slight over-etching of the holes from the top and the channels from below by a few micrometers ensures that the supply holes are fully opened, thereby preventing flow restriction due to incomplete etching of the pyrex circuitboard.

5.3 Fabrication of the Microfluidic Circuitboard

5.3.1 Micromachining

The main part of the microfluidic circuitboard is a 0.5 mm thick pyrex glass wafer. The glass surface is often mechanically stressed after polishing during manufacture. This stress leads to a very ragged edge after etching in hydrofluoric acid (HF). To achieve smooth edges during the

process, the wafer has to be annealed for 1 hour at 570 degC. This was done in a horizontal furnace in atmospheric ambient.

The fabrication process for the pyrex wafer can be divided into two major parts. The first part is creating doubled sided alignment aids (figure 5.2 a-e). These alignment aids are necessary as the channels and the supply holes are etched at the same time from both sides of the wafer and need to be aligned to each other. The equipment normally used for double sided alignment of silicon can not be used for pyrex with chromium/gold as a masking material, as there is no transmission of the infrared light. The masking layers need to be opened from the back to align the mask for the channels through the optically transparent pyrex glass to the marks etched earlier into the front.

For this, the pyrex wafer is coated on both sides with a 100 nm thick gold (Au) layer using a 20 nm thick chromium (Cr) layer as an adhesion promoter (figure 5.2 a). After lithography, using Shipley S1818 resist (2.2 μm thick), the gold and chromium layers are structured with potassium iodide and chromium etchant (22% ceric ammonium nitrate and 5% acetic acid), respectively (figure 5.2 b). Without removing the resist, the whole wafer is placed into 48% HF at room temperature for 90 sec to give 12 μm deep marks. The etch rate for this etch is therefore 8 μm min^{-1}. After that the layers of resist, gold and chromium are stripped (figure 5.2 c).

For the next step, the pyrex wafer is coated a second time on both sides with Cr and Au layers. This time the thickness of the Au is 300 nm and the thickness of Cr is 40 nm to protect against the longer channel and through-hole etch which follows later. To expose the alignment marks on the front for the double sided alignment on the back of the wafer the Cr/Au-layer on the back has to be opened, as mentioned before. For that purpose a mask with two large square openings is coarse aligned on the back to the etched front marks. After structuring the resist, the gold and chromium layers are etched (figure 5.2 d). Finally the resist is stripped off (figure 5.2 e).

The same chromium/gold layers are now used for the second part of the fabrication process, which is the creation of the channels and holes into the Pyrex (figure 5.3 a-d). The back contains the structures for the channels and holes and on the front are the structures for the connection holes to the different microfluidic devices only. The back is aligned through the previously opened windows in the Cr/Au-layer to the etched marks on the front. Then, resist, gold and chromium layers are structured while the front Cr/Au-layer is protected with resist (figure 5.3 a).

After that, the resist is stripped off with fuming nitric acid and in a new lithography step the front mask is aligned to the etch marks, while the back is protected. The stripping of the resist is necessary as the front protection layer for the back etch cannot be structured after the hardbake. The gold and chromium are etched (figure 5.3 b) and after that the resist is stripped off with fuming nitric acid. Now, after both sides of the Cr/Au-mask on the pyrex are structured (figure 5.3 c) the wafer is exposed to 48 % HF at room temperature for 32 min to etch from both sides equally into the 500 μm thick pyrex (figure 5.3 d). Stripping the gold, chromium and resist layers finishes the processing of the pyrex.

The channels have to be sealed to complete the microfluidic circuitboard by bonding a silicon base wafer (figure 5.3 e). The wafers are cleaned with fuming nitric acid and anodically bonded using a voltage of 400 V at 390°C for 20 min. Apart from the cleaning step the silicon base wafer is not processed.

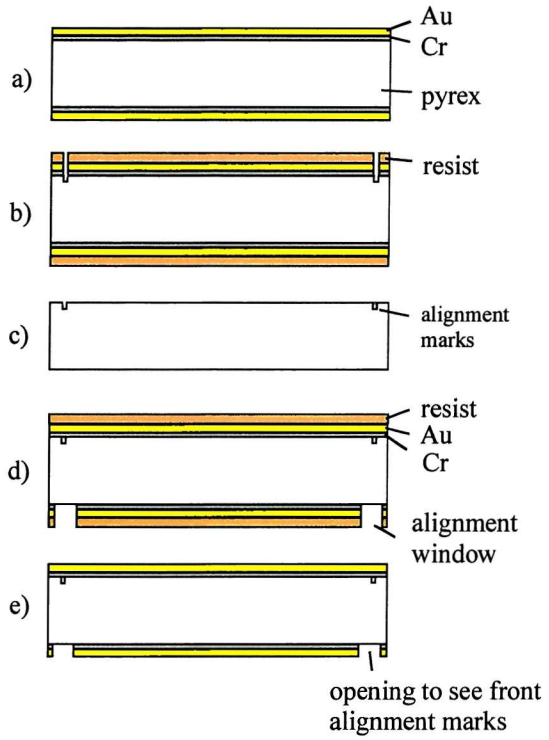

Figure 5.2: Schematic of the fabrication process (wafer level).

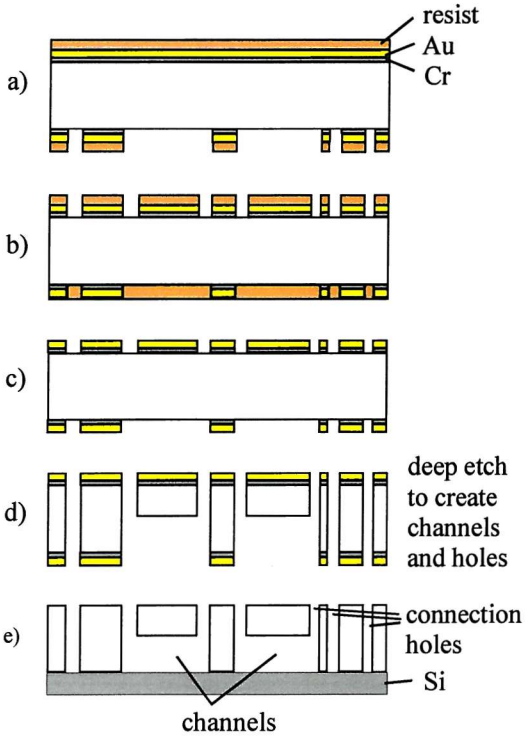

Figure 5.3: Schematic of the fabrication process (chip level).

A photograph of the finished microfluidic circuitboard is shown in figure 5.4. To create microfluidic systems, discrete devices are mounted over the orifices on top of the pyrex in a follow-up step also using the anodic bonding method with the same parameters. The negative electrode is connected to the pyrex via the hotplate and the silicon base wafer and the positive electrode is placed on top of the silicon part of the discrete microfluidic devices.

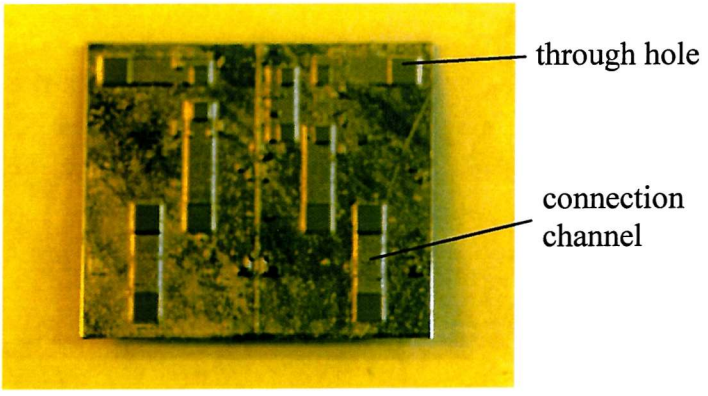

Figure 5.4: Photograph of the microfluidic circuitboard.

5.3.2 Discussion

The result of the first batch proved the fabrication sequence to be functional. However, the surface of the pyrex was rough due to pinholes in the Cr/Au-mask through which the HF could attack the pyrex. The thickness of the masking layer during the long HF etch for the first batch was chromium 40 nm and gold 300 nm. Figure 5.5a shows a photograph of an etched pyrex wafer. The dark marks are the holes on the top of the wafer and the grey marks are the unfocused holes on the back of the wafer. The diameter of the largest holes is about 100 µm, which was measured using a profilometer. The depth of the holes was measured to be 60 µm. In some cases the number of the holes was so high that clusters formed, leading to cross leakage between closely spaced channels as can be seen in figure 5.6.

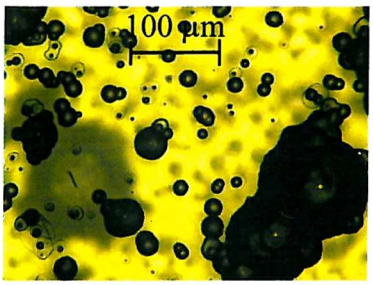

Figure 5.5a: Holes etched into the pyrex through thin Cr/Au masking layer.

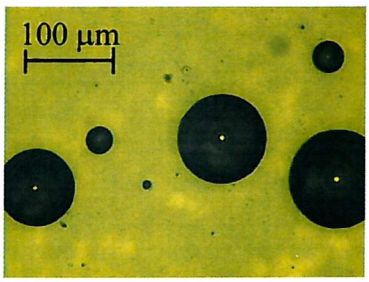

Figure 5.5b: Holes on the back with thick Cr/Au masking layer.

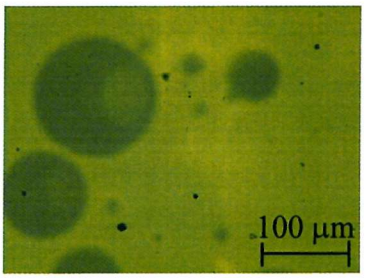

Figure 5.5c: Small black dots are holes on the front with thick Cr/Au layer and photoresist as masking layer. The grey marks are the unfocused holes on the back.

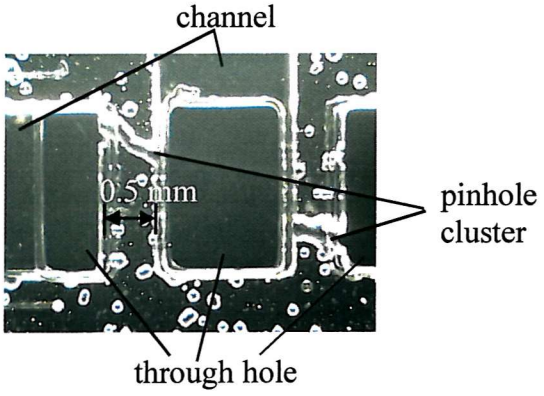

Figure 5.6: Zoom into microfluidic circuitboard: pinhole cluster between channels.

This problem was solved in a second batch by using a thicker masking layer. The chrome was here 40 nm and the gold 600 nm, which was the maximum achievable thickness with the evaporator present in the cleanroom at Southampton University. Besides that, the resist was left on the upper side during etching of the wafers in HF. The resist could not be left on the back due to the process flow. The back had to be covered completely with resist to prevent

underetching of the gold structures, which had already been patterned. Then it had to be stripped off to etch the pyrex. The one sided stripping was done on a spinning chuck with spraying acetone onto the wafer.

The amount of pinholes was significantly less (figure 5.5b and 5.5c) compared to the previous process (figure 5.5a) and the pinholes were not connected to each other, hence preventing leakage between the channels. The resist proved to be an effective additional masking layer as a difference between the lower (figure 5.5b) and upper (figure 5.5c) side could be seen after the etching. The resist, Shipley S1818 - 2.2 μm, was hard-baked for 30 min at 115 degC. It can withstand the 48% HF etch for 40 – 45 min before lifting off.

The anodic bonding of either batch one, with the thin Cr/Au masking layer, or two, with the thick Cr/Au masking layer, even with the rough surface, was not a problem. The channels could always be sealed with the silicon bottom wafer so that no leakage occurred. Only some devices from batch one, where pinhole clusters formed between channels with narrow spacing, could not be used for creating microfluidic systems due to cross leakage.

The bond between pyrex and silicon is permanent and no long term stability problems occur. The bond yield was always 100% due to the large bond areas.

Other masking methods for pyrex etching are reported in the literature using silicon for pinhole prevention. Lammerink [Lamm93] used sputtered polysilicon (thickness not stated) and Corman [Corm97] structured a 0.5 mm thick silicon wafer, which was then anodically bonded to the pyrex. After the pyrex etch, the silicon wafer was stripped off with KOH. It was still possible to anodically bond again on the same side of the glass wafer which was anodically bonded already once before. Bartek [Bart00] used a 200 nm thick amorphous silicon layer deposited by low pressure chemical vapour deposition.

Investigations for the application of the above mentioned masking layers were done. Sputtered polysilicon cannot be used, since pyrex wafers are treated as contaminated (sodium ions) and are therefore not allowed into the sputtering machine in the cleanroom at Southampton University.

The approach with the pre-patterned silicon wafer bonded to the pyrex wafer seems inappropriate. New masks would have to be designed and the structuring and post-etch removal of the 0.5 mm thick silicon is very time consuming. The etch rate of silicon in 33% KOH at 70 degC is 0.54 μm/min, which would lead to an etching time of almost 16 hours for the structuring and the same time for the removal of the silicon masking wafer. The third possibility, the amorphous silicon approach, seemed to be the most promising as the technology for depositing amorphous silicon is available.

A test batch with a 500 nm thick amorphous silicon layer deposited onto pyrex was created. After a fuming nitric acid clean the wafers were placed into a DEP90 plasma deposition system from Oxford Plasma Technology, which used silane (SiH_4) as a deposition gas. The silicon was patterned using reactive ion etching (SF_6). After placing the pyrex wafer in 48% HF, the amorphous silicon lifted off the wafer after 1 min etching time ruining the wafers.

Due to satisfactory results from the first two batches using chromium/gold, the masking with silicon has not been followed up. However, varying the process conditions, e.g. power,

temperature, pressure and frequency of the plasma depositor could enhance the deposition of the amorphous silicon similar to the plasma silicon nitride deposition [Claa85]. Different internal stress under varying process conditions could be achieved. The adhesion of the amorphous silicon might be improved by applying an adhesion layer, e.g. chromium, which sticks well to pyrex and silicon, or by trying to anodically bond the amorphous silicon layer to the pyrex.

5.4 Testing of the Microfluidic Circuitboard

Two different tests for the validation of the fluidic circuitboard principle were carried out. First a piezoelectrically actuated diaphragm micropump was mounted onto the circuitboard and the performance of the pump was investigated. Second a complex fluidic system was realised on top of the circuitboard and liquid was passed through the system to show the leak free interconnection of the discrete devices. It is the first time that such a microfluidic system on a single chip has been presented.

5.4.1 Test Employing a Diaphragm Micropump

A diaphragm micropump was mounted onto the microfluidic circuitboard. Two Perspex blocks were glued over the inlet and outlet ports with Cyanoacrylate adhesive for external fluid connection. Both, Perspex and Cyanoacrylate, are compatible with the use of ethanol as a test liquid. The system was filled with the pressure of the liquid column at the inlet side, which was approximately 1.5 m high. A schematic of the test setup can be seen in figure 5.7. The purpose of this experiment was to evaluate the pump performance when mounted onto the fluidic board. The pump used has been characterised by Koch [Koch00]. It features dynamic passive valves (smaller diameter of cone is D_0 = 130 µm) with a piezoelectric actuator mounted on top of the membrane. The silicon membrane has dimensions of 8 mm x 4 mm and is 70 µm thick. The size of the piezo (PZT-5H) is 7 mm x 3 mm and is 250 µm thick.

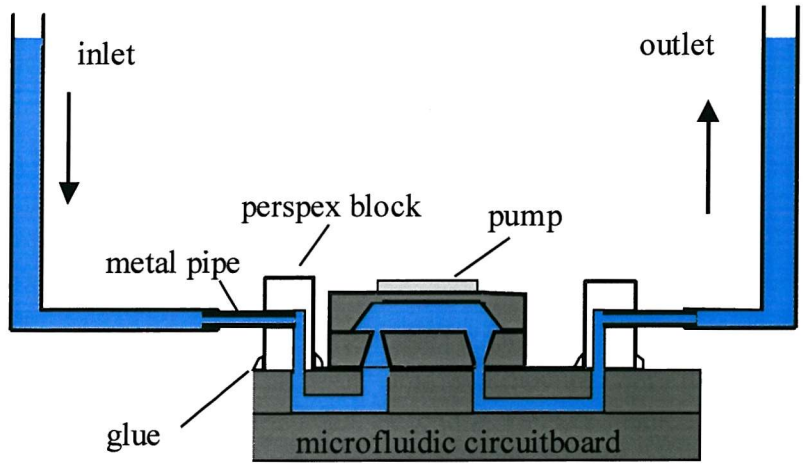

Figure 5.7: Schematic of the test setup for the microfluidic circuitboard.

The pump rate is measured by the height of the liquid column displaced during a certain time at the outlet hose. Figure 5.8 shows the pump rate versus the frequency at zero backpressure, with a maximum pump rate of 350 µl/min at 300 V_{pp} applied to the PZT. A simulation of the pump rate for the above micropump dimensions and for a voltage of 300 V_{pp} applied to the piezoelectrics has been done (see section 3.2.3) and is shown also in figure 5.8. The measurement correlates well with the simulation up to a frequency of 1700 Hz. After that dynamic effects cause the measured pump rate drop. Those effects are not included in the simulation.

It can be concluded, that the channels within the fluidic circuitboard give no significant pressure loss and that the anodic bonding method can be used for the leakage free assembly of devices onto the circuitboard.

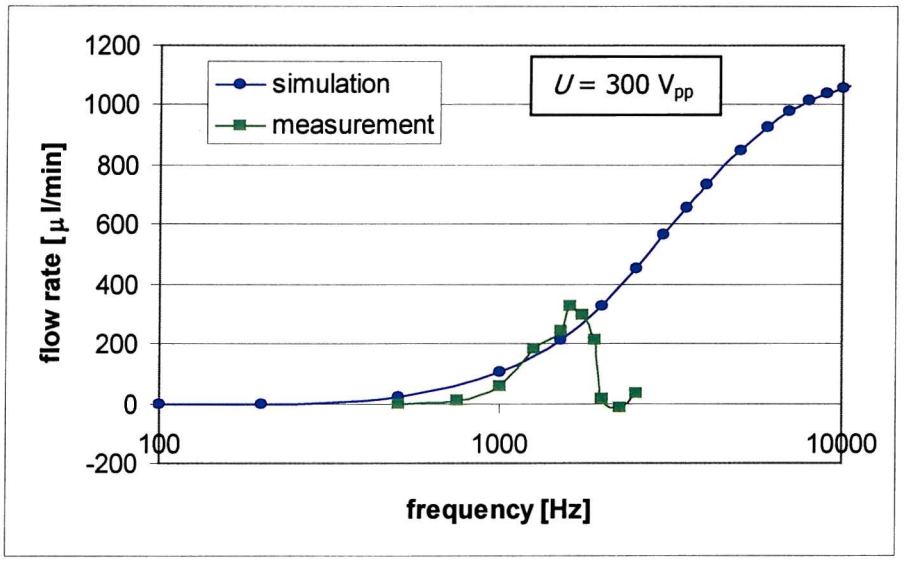

Figure 5.8: Simulated and measured pump rate versus frequency of a diaphragm micropump mounted on the microfluidic circuitboard.

5.4.2 Microchemical Reaction System

A novel and complex system has been realised on the microfluidic circuitboard. It consists of two pumps, two flow sensors and a mixing chamber. A schematic of the principle of the chemical reaction system is given in figure 5.9 and a photograph of the whole system is shown in figure 5.10. The two pumps have the same dimensions as the one above (section 5.4.1). The flow sensors (see chapter 4) have a channel width of 580 µm, a channel length of 2 mm and a channel height of 100 µm, but are dummy devices, i.e. they don't have working sensing elements. The mixing/reacting chamber [Koch98c, Koch99] relies on interdiffusion of the fluids, as the small value of the Reynold's number in micro-capillaries does not favour turbulent mixing. Two fluids/chemicals come together through 32 laterally alternated inlets in order to increase the boundary surface between them. The mixing chamber has a width of 2.2 mm, a length of 2.4 mm and a height of 5 µm. The results from Koch showed, that with this device,

perfect mixing was achieved at pressures lower than 2 kPa. For higher pressures, the flow streams are separated until they exit the mixing chamber.

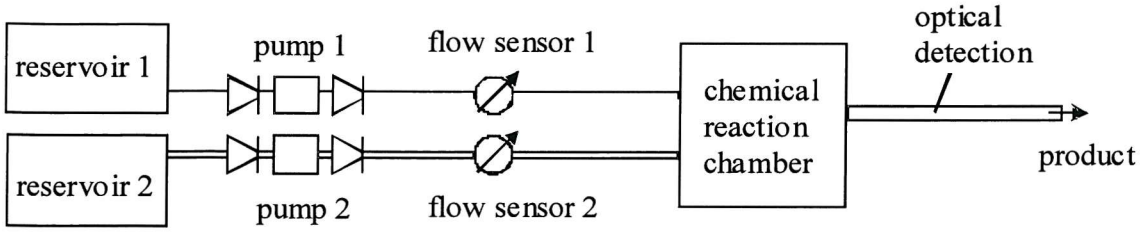

Figure 5.9: Schematic of a chemical reaction system.

The reaction system realised on the microfluidic circuitboard was tested by mixing red and green inks. The advantage of using inks as test liquids is that proportional mixing can be made visible and the diffusion process can be observed throughout the length of the micromixer [Koch99]. Before usage, the inks were mixed with ethanol (5 parts ink, 5 parts ethanol) and passed through filters with 0.2 µm pores to ease the handling procedure. The inks were fed into the system by varying the height difference (~ 0.2 - 1 m of liquid column) between the inlet reservoirs and the mixing chamber. The hoses were connected to the circuitboard by means of Perspex blocks glued over the inlets and the outlet (figure 5.7).

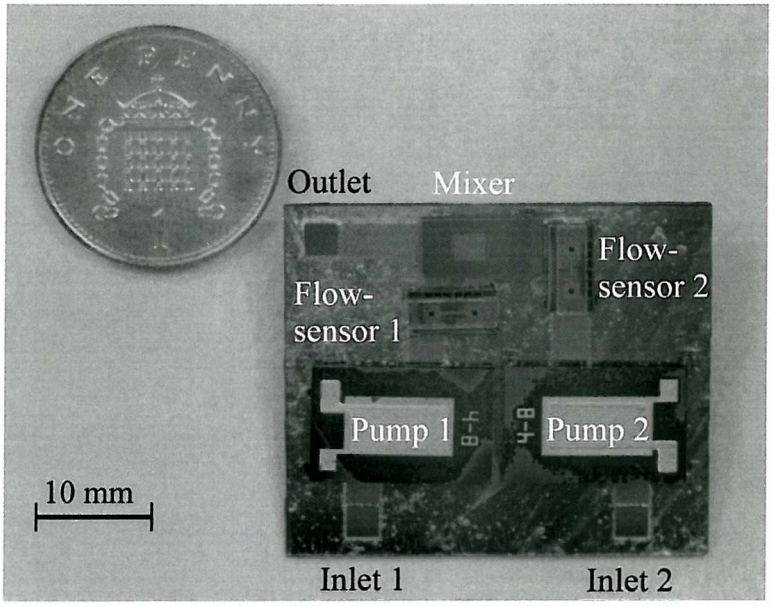

Figure 5.10: Microchemical reaction system realised on a microfluidic circuitboard. Dimensions of the circuitboard: 3 cm x 3.5 cm x 0.1 cm.

The system proved to be leakage free and the inks could be mixed in the chamber with the pressure created by the heights of the inlet liquid columns. The pumps had no PZT actuator and were used only as flow through devices. (The system shown in figure 5.10 broke during handling and another system was set up without PZT actuators on the pumps). The pressures from the height of the inlet liquid columns have not been recorded as it was only intended to

prove the microfluidic circuitboard for interconnection of the discrete fluidic devices. For future work, the liquids should be actively pumped by the diaphragm micropumps, with the flow controlled by the flow sensors.

This type of system has the potential to be used for automated chemical analysis or (bio)chemical production on the micron scale. Applications include the measurement of a reaction gradient (stopped flow), screening of chemicals for drug discovery or DNA synthesis, enzyme & substrate reactions, high temperature as well as light induced reactions. Compared with conventional reactions several advantages are gained with a shift to microsystems: Clean reactions are possible due to constant flushing out of the products, and a very homogeneous temperature distribution is achievable for endothermic reactions. Furthermore, reactions are safer through the use of small quantities. With the use of massive parallelisation of these systems the same volumes could be processed as with larger systems.

A specific application of this microfluidic chemical reaction system is in aquatic analytical applications, which is being explored together with the Oceanography Centre of Southampton University. Important points are the use of very low power and the use of only small volumes of reagents thus the system is ideally suited for long deployments in situ. Furthermore, the mixing and reaction is more rapid than if conventional large-scale systems are used.

Examples of uses of small autonomous analysers in the sea include measurement of plant nutrients, specifically ammonia, which can be toxic at high concentrations. Ammonia is produced during destruction of organic matter and may grow to unacceptable concentrations under polluted conditions. It is a high priority analyte for water authorities and groups such as the Environment Agency, and the best technique currently uses fluorescent detection. A single working reagent consisting of orthophthaldialdehyde, sodium sulfite and sodium borate, is mixed with the sample [Holm99], thus making it an ideal application for the above presented microfluidic circuitboard. The fluorescent light can either be detected directly above the mixing chamber as it has a pyrex glass lid or later within one of the fluidic channels in the circuitboard, consisting also of transparent pyrex.

One can envisage small disposable analysers being employed a) in rivers or lakes to give forward warning of high ammonia levels, b) for basic research in open ocean systems with a series of inexpensive analysers along a vertical line under a buoy, and the buoy left for weeks/months. This would provide remotely information on the vertical structure with time. Such an array could be towed behind a ship to give quasi instantaneous along track information on spatial variability for a set vertical distance.

To evaluate the usability of a micromachined system initial sea water compatibility tests are being carried out. Southampton Oceanography Centre tests samples with silicon, silicon dioxide and silicon nitride surfaces and the results are being awaited.

5.5 Conclusion

Achieving integrated microfluidic systems, e.g. chemical microplants, drug delivery systems and particle analysis systems is of great interest because of low-cost fabrication and possible

automation. A very common method in electronics is the integration of discrete devices on an electrical circuitboard. In order to adapt this technique in microfluidics, a microfluidic circuitboard has been developed.

The layout of the fluidic circuitboard is described with the channels having a width of 2-3 mm, a length of 3-6 mm and a height of 250 μm. The pressure losses have been calculated to be less than 5 Pa within a channel for a flow rate of 100 μl/min.

The micromachining of the pyrex is explained, which is based on deep etching with 48% hydrofluoric acid to form channels and through holes. The formation of holes in the pyrex surface due to pinholes in the chromium/gold masking has been discussed. Silicon as a masking layer would give the best results, but due to technological restrains this could not be accomplished. However, a thick chromium/gold masking layer with photoresist gave satisfying results.

On top of the circuitboard, various microfluidic devices can be mounted simply with the anodic bonding method. To realise different microfluidic systems only the mask layout for creating the channels in the pyrex wafer has to be changed. This allows a way of mass fabricating different microfluidic systems. The fluidic circuitboard has been tested by mounting a diaphragm micropump and measuring the pump rate. A voltage of 300 V_{pp} and a frequency of 1.6 kHz applied to the PZT gave a pump rate of 350 μl/min. The measurement correlates well with the simulation up to a frequency of 1.7 kHz, after that the measured pump rate drops due to dynamic effects. Those effects are not included in the simulation.

A whole set of discrete microfluidic devices has been surface mounted successfully onto the microfluidic circuitboard containing the interconnection channels. Two inks were fed through two pumps, two flow sensors and a mixing chamber connected on a single chip. The assembled system proved to be free from leakage and the two inks could be combined within the micromixer.

It can be concluded that the channels within the fluidic circuitboard give no significant pressure loss and that the anodic bonding method can be used for leakage free assembly of discrete devices. Several applications have been listed to show the potential applications of the realised microfluidic chemical reaction system.

CHAPTER 6

Micromachined PCR-Chip: Biotechnology Combined with Microfluidics

6.1. Introduction

The polymerase chain reaction (PCR) is a well-characterised method for the selective identical replication of DNA molecules [Erli89]. By an enzymatic in-vitro amplification process, the concentration of a DNA species is nearly doubled in a process, which steps through three different temperatures. In this way, the DNA concentration can be multiplied more than a million-fold by 20 to 30 cycles of temperature. A description of DNA amplification using PCR is given in appendix A.

Since the first report of specific DNA amplification using the PCR in 1985, the number of different applications has grown steadily. It has become an important analytical method for the detection of diseases, pathogens or in forensics where the amount of sample is often small and direct detection would be impossible. Two important innovations were responsible for automating PCR. First, a heat-stable DNA polymerase was isolated from the bacterium 'Thermus aquaticus', which inhabits hot springs. This enzyme, called the 'Taq DNA polymerase', remains active despite repeated heating during many cycles of amplification. Second, DNA thermal cyclers have been designed in which a computer controls the repetitive temperature changes required for PCR.

The advantages of miniaturized PCR chips are many, such as rapid temperature cycling, smaller quantities of rather expensive reagents needed, low cost fabrication and portability, which is of great use for environmental screening as well as in the medical sector. The first micromachined PCR chip was presented by Northrup in 1993 [Nort93]. It used a relatively large reagent volume of 25 – 50 µl and needed the use of silicone adhesive to seal the chambers. Since then, a number of miniaturised PCR chips have been presented and they are reviewed in section 2.2.3.

The aim of this project was to design a miniaturised PCR chip that is capable of very fast temperature cycling, hence having a low reagent volume and low thermal mass. Also it must

have the potential for real-time optical detection, i.e. have an optical window into the reaction chamber. A schematic of such a PCR chip can be seen in figure 6.1.

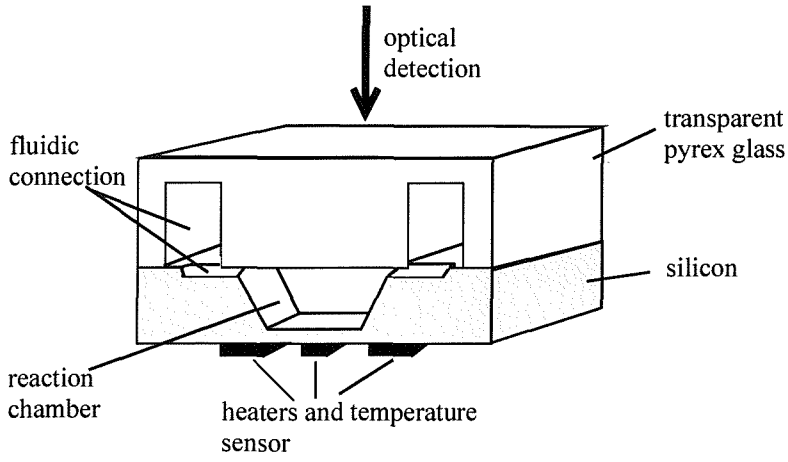

Figure 6.1: Schematic cross section of a micromachined PCR chip.

The PCR chip presented by Daniel [Dani98] has a reagent volume of 1 µl and is very fast (heating 90 degC/sec; cooling 74 degC/sec) but lacks the possibility of optical detection of the PCR products. An oil drop is used to seal the reaction chamber and thus prevent the PCR solution from evaporating. Poser [Pose97] also presented a silicon based PCR chip with very fast temperature rise (80 degC/sec) and fall times (40 degC/sec). The reaction chamber has a volume between 5 µl and 10 µl and is covered with a glued pyrex plate. Optical detection is also not possible as the inlet and outlet tubes cover the reaction chamber. Furthermore, the device is very large (20 x 18 mm^2) and high integration, i.e. low cost fabrication, is not possible. The heating and cooling rates of other published PCR chips are slow or the chips lack the possibility of optical detection.

Instead of a micro-chamber, Kopp [Kopp98] and Koehler [Koeh98] employed capillaries on a silicon chip to construct a 'continuous flow PCR' device. However, given the capacity of PCR to synthesise millions of DNA copies, contamination of the sample reaction with products of a previous reaction (product carryover) is a potential problem, particularly in those reactions initiated with only a few templates. Therefore, for industrial applications single shot PCR devices are preferred. Furthermore, these devices are not flexible enough, e.g. for changes in cycle number. Monitoring the kinetics of the reaction would be difficult as the reaction mixture is within a long channel.

In the following sections, the design, fabrication and packaging of a silicon based closed chamber PCR chip with an optical window is described followed by performance data. Further integration was investigated and a study on optical fibres and pn diodes integrated into the PCR chip has been carried out. This obviates the need for bulk optical components like mirrors and lenses and enables the system to be made insensitive to ambient light.

The work was carried out under a contract from the Defence Evaluation and Research Agency (DERA) Porton Down. The instrumentation box used to control the thermal cycling and the optical detection was contracted to and to be built by OptiSense Ltd.

6.2 Closed Chamber PCR-chip

6.2.1 Design

This section describes the design such as chamber size, chip size and fluidic connection on the chip as well as the electrode design and the thermal aspects of the PCR chip.

6.2.1.1 Chamber and chip dimensions

The aim of the work was to design PCR chips with chamber volumes of 1 µl. The dimensions of the chambers were calculated, taking into consideration the angle of 54.71 degrees between the (111) and (100) crystal planes of <100> silicon wafers when using KOH as a chemical etchant (figure 6.2) [Seid90]. The depth of the chamber was chosen to be 400 µm, which leaves a membrane thickness of 100 µm. Thinner membranes might break during the temperature cycles as the liquid within the chamber expands. The length and the width of the upper chamber edges were calculated to be 1.86 mm for a 1 µl chamber. Square chambers were chosen because of the easier optical detection when a circular beam of light is shone into the chamber from the top and fluorescent light is detected through a dichroic beam-splitter and an optical filter, also from the top.

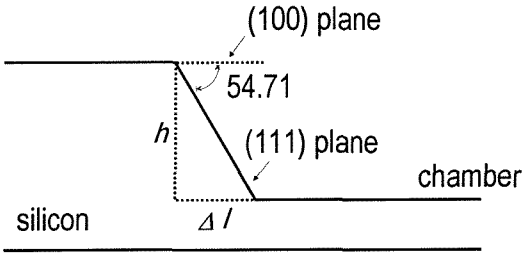

Figure 6.2: Scheme for the relation between the upper and lower chamber area; h is the height of the chamber and Δl is the reduction in length.

The chip size was determined by the chamber size, the space required for the fluidic connections and the areas necessary for anodic bonding (figure 6.3). On the back, space for the resistors and wire-bond pads was needed and an area beneath the reaction chamber was required for placement of the Peltier cooling pad (figure 6.4). The dimensions of the various components are given in the following sections. The above mentioned criteria gave a chip size of 6 mm x 4 mm. There were 222 chips on each wafer.

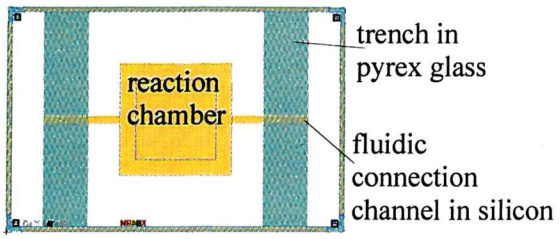

Figure 6.3: Layout of the PCR chip: top view.

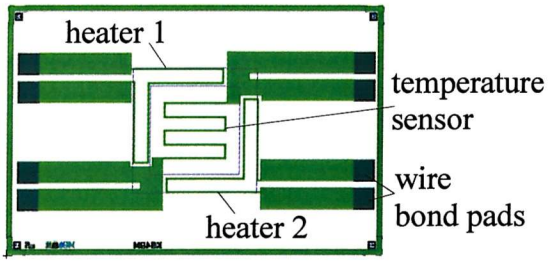

Figure 6.4: Layout of the PCR chip: bottom view.

6.2.1.2 Internal and external fluidic connection

The fluidic connection involves a trench sawn into a 1 mm thick pyrex wafer and a channel etched into the silicon leading from the saw cut to the reaction chamber as depicted in figures 6.1 and 6.3. The trench in the pyrex is 0.8 mm wide and 0.8 mm deep where a hypodermic needle or a fused silica capillary of 0.6 mm diameter can be glued in as described in 6.2.3. The trenches for inlet and outlet are located on either side of the chamber to keep the area above the chamber clear for optical detection.

The connection channel etched into the silicon from the trench in the pyrex to the PCR chamber is designed to give as little pressure loss as possible and at the same time have small dimensions. The triangular shaped channels are 142 µm wide and 100 µm deep. The pressure drop Δp is calculated from [Grav93]:

$$\Delta p = Q \cdot C_{fr} \cdot L_{ch} \cdot \frac{\mu}{2 \cdot A \cdot D_h^2} \tag{6.1}$$

where Q is the volume flow, C_{fr} is the friction coefficient (for KOH etched triangles C_{fr} = 35.12 [Rich97]), L_{ch} is the length of the channel, μ is the viscosity ($1.005 \cdot 10^{-3}$ Ns m^{-2} for water), A is the cross sectional area of the channel and D_h is the hydraulic diameter (see equation 5.2). For a volume flow of 100 µl/min and a channel length of 770 µm the pressure drop is 600 Pa and therefore, the channels can be easily filled with a syringe. The pressure drop is also low enough to fill the chamber with a micropump and hence, the PCR chip can be integrated into a microfluidic system.

The meeting point of the fluidic connection channel with the square PCR chamber created a convex corner and because of the crystal dependent etch rates of KOH, compensation structures had to be implemented to avoid etching of the corners. Three different structures were designed. The first uses a rectangular area of 742 µm width and 870 µm length (figure 6.5). The width was calculated using [Sand91] while the length was restricted by the size of the chamber as a space between the left and right compensation structure had to be left for the KOH to attack:

$$b_s = \left(2 \cdot d \cdot \frac{R(141)}{R(100)} - L_s\right) \cdot 2 \cdot \tan 31^\circ \tag{6.2}$$

where d is the etch depth, $R(141)/R(100)$ is the etch rate relationship between the crystal planes (1.4 in 30% KOH) and L_s is the length of the structure. The width of the beam is $2b_s$ plus the width of the fluidic connection channel (142 μm).

The second compensation structure uses a triangular area. It was designed such that the distance from the corner where the fluidic connection channel meets the chamber to the side of the triangle was 400 μm (which is the etch depth) as indicated in figure 6.6.

The third layout of the PCR chip had no compensation structure implemented (figure 6.7).

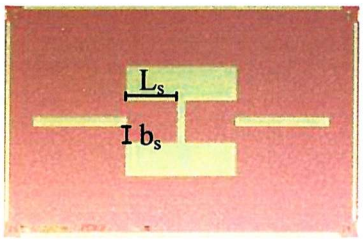

Figure 6.5: Rectangular compensation structure.

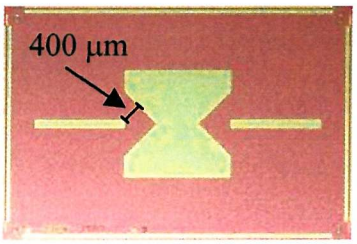

Figure 6.6: Triangular compensation structure.

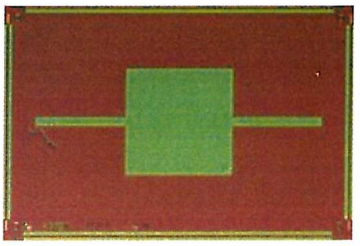

Figure 6.7: Without compensation structure.

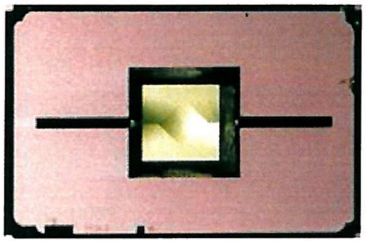

Figure 6.8: After etching in KOH 400 μm deep: corners not underetched.

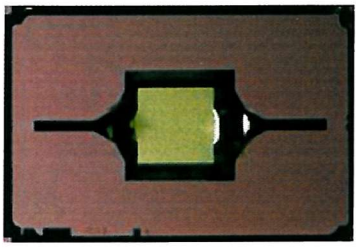

Figure 6.9: After etching in KOH 400 μm deep: corners slightly underetched.

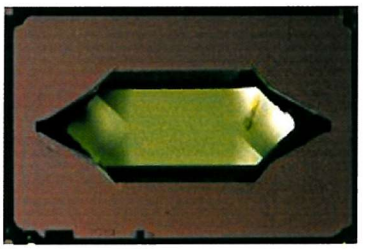

Figure 6.10: After etching in KOH 400 μm deep: corners totally underetched.

As can be seen in figure 6.8, after etching 400 μm deep into the silicon wafer, the corners where the fluidic channel meets the chamber are not underetched with the rectangular compensation structure. Using the triangular compensation structure, the corners were slightly underetched (figure 6.9) and on the PCR chip without compensation structures, the corners were totally underetched (figure 6.10). The square chamber is more difficult to fill with liquid as gas bubbles can get stuck in the corners whereas the chamber with the widest inlet and outlet opening is easiest to fill.

6.2.1.3 Electrode design

The two heaters and the temperature sensor, which are deposited on the back of the PCR chip, are made of 200 nm thick platinum with an adhesion layer of 20 nm thick titanium. The sensor was designed to have a resistance of 100 Ohm with four contact pads, which is an industrial standard for temperature sensors. It is located under the bottom of the chamber. The two heaters are placed directly under the chamber side walls and can be connected in parallel or in

series. The electrode design is shown in figure 6.4. For platinum, there is a linear relationship between temperature and resistance and it is used for most commercially available temperature sensors.

For calculating the theoretical resistance values R of the electrodes the following formula has been used:

$$R = \frac{l}{b} \cdot \frac{\rho_r}{d} \tag{6.3}$$

where l is the length of the electrode, b is the width of the electrode, ρ_r is the specific resistance (ρ_r = $1 \cdot 10^{-7}$ Ω m for platinum), and d is the thickness of the electrode. The temperature sensor is l = 5.9 mm long and b = 0.03 mm wide. This gives a value of R = 98 Ω. The length of the heater is l = 5.5 mm and the width is b = 0.05 mm, giving a value for R = 55 Ω.

Aluminium (1 µm thick) is deposited over the wire-bond pads (figure 6.4) as gold wires do not bond to platinum. An 80 nm thick oxide between the silicon and the titanium/platinum eliminates any electrical contact between the discrete resistors.

6.2.1.4 Thermal considerations

The power P, required to cause a temperature rise ΔT in a time Δt is given by the following equation [Stoe93]:

$$P = C_{th} \cdot \frac{\Delta T}{\Delta t} \tag{6.4}$$

C_{th} is the thermal capacitance and is calculated by [Stoe93]:

$$\begin{aligned} C_{th} &= C_{th\ si} + C_{th\ water} + C_{th\ pyrex} \\ &= (\rho_{si} \cdot c_{p\ si} \cdot V_{si}) + (\rho_{water} \cdot c_{p\ water} \cdot V_{water}) + (\rho_{pyrex} \cdot c_{p\ pyrex} \cdot V_{pyrex}) \end{aligned} \tag{6.5}$$

where ρ is the density, c_p the specific heat and V the volume of silicon, water or pyrex. The volume of the reaction chamber is 1µl and therefore, V_{water} = $1 \cdot 10^{-9}$ m^3 and the volume of the silicon chip (6 mm x 4 mm x 0.5 mm) is V_{si} = $11 \cdot 10^{-9}$ m^3. The volume of the pyrex (6 mm x 4 mm x 1 mm) is V_{pyrex} = $2.4 \cdot 10^{-8}$ m^3. With the data given in table 6.1, the thermal capacitance is calculated to be C_{th} = 59.5 mW s K^{-1}. A similar calculation for the thermal capacitance of a PCR chip filled with water has been done by Daniel [Dani98]. To heat the chip from room temperature (20 degC) to 95 degC within 1 second, a power of 4.46 W is necessary (equation 6.4).

material	density [g cm^{-3}]	specific heat [W s g^{-1} K^{-1}]	thermal conductivity [W m^{-1} K^{-1}]
silicon	2.33	0.714	150
water	0.996	4.18	0.613
pyrex	2.2	0.7	1.46
RS quick-set epoxy	-	-	0.22

Table 6.1: Parameters of silicon, water, pyrex and glue (at 300 K).

The thermal time constant τ for the PCR chip can be calculated by:

$$\tau = C_{th} \cdot \theta \tag{6.6}$$

where θ is the thermal resistance, which is given by [Stoe93]:

$$\theta = \frac{L}{k \cdot A} \tag{6.7}$$

where L is the length of the thermal path, k is the thermal conductivity and A is the heat conducting area. A schematic of the thermal network can be seen in figure 6.11. It is assumed that heat is lost over the areas where the chip is glued to the package with the package acting as a heat sink. Heat losses to the surrounding air have not been included in the calculation and therefore, the result will only be a rough estimate.

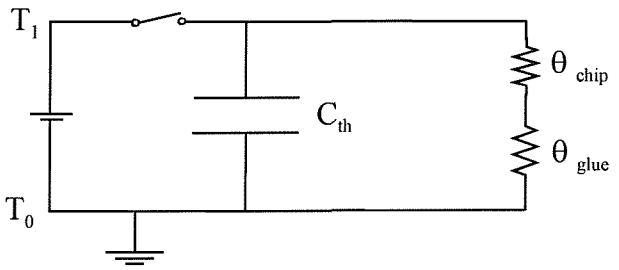

Figure 6.11: Schematic of the thermal network.

The thermal resistance of the chip (figure 6.12) is calculated by:

$$\theta_{chip} = \left(\frac{1}{\theta_{Si1}} + \frac{1}{\theta_{Si2} + \theta_{water}} + \frac{1}{\theta_{Si3}} \right)^{-1} + \theta_{py} \tag{6.8}$$

with L_{py} = 1 mm, A_{py} = 2.4·10^{-5} m^2, $L_{Si1,3}$ = 500 µm, $A_{Si1,2,3,water}$ = 8·10^{-6} m^2, L_{Si2} = 100 µm, L_{water} = 400 µm and the thermal conductivity data from table 6.1 it follows that θ_{chip} = 28.7 K W^{-1}.

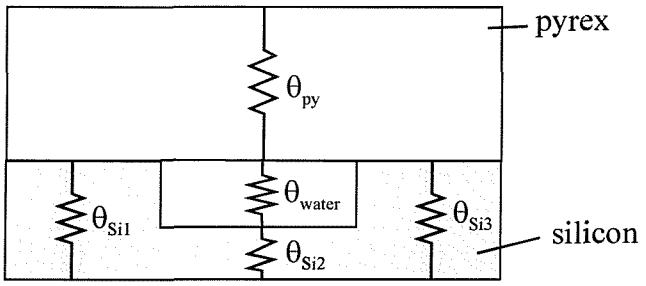

Figure 6.12: Schematic of the thermal resistances within the PCR chip.

The thickness of the glue is about 100 μm with a contact area between the chip and the package of $A_{glue} = 3 \cdot 10^{-6}$ m^2. Using equation (6.7) and the data for thermal conductivity for the glue from table 6.1, a thermal resistance of $\theta_{glue} = 151.5$ K W^{-1} can be calculated. The thermal resistance of the network is therefore $\theta = \theta_{chip} + \theta_{glue} = 180.2$ K W^{-1}. The time constant can now be calculated using equation 6.6 to obtain a value of $\tau = 10.7$ sec.

It is expected that the chip can be heat cycled fast enough with this time constant value. The chip presented by Poser has a size of 18 x 20 mm^2 and has temperature rise times of 80 degC/sec and temperature fall times of 40 degC/sec. Although there are thermal insulation structures implemented, the chip is still larger than the here presented. The measurement results in section 6.2.4.2 give a time constant of 7.3 sec and in section 6.2.4.3 it is shown that the chip can be cycled with temperature rise times of 44 degC/sec and temperature fall times of 33 degC/sec, which proves that the assumption was right.

6.2.2 Fabrication

The micromachining is based on double sided processing of silicon and pyrex wafers. For aligning chambers on one side and the electrodes on the other side of the silicon chip, double sided alignment structures need to be implemented. The fabrication of the silicon wafer requires four lithography steps and the fabrication of the pyrex wafer one lithography step.

In this section, the creation of the double sided alignment structure is described. Before the first lithography step, the wafers were cleaned with fuming nitric acid. Then positive photoresist, Shipley SPRT511, was spun onto the front of the wafer using an automatic track spinner. The alignment of the first mask for the double sided alignment structures was done using a semi automatic mask aligner. The etching of the marks into the silicon was done with a dry etcher using SF_6 as the reaction gas. The etching rate is 1 μm per minute. The resist was then stripped off using an asher (oxygen plasma) subsequently followed by a 10 min clean in fuming nitric acid. After spinning positive photoresist onto the back of the wafer a manual mask aligner, fitted with an infrared camera, was used for the double sided alignment. The silicon is transparent to infrared light. Again the dry etcher was used for creating 1 μm deep marks on the back of the wafer.

After etching the double sided alignment structures onto the front and the back of the wafer it was oxidised with 600 nm of wet oxide and covered with 160 nm of LPCVD nitride (low pressure chemical vapour deposition). Both layers were structured by reactive ion etching, using a dry etcher with CHF_3 and argon as etching gases, to give the patterns of the reaction chambers, the connection channels and the compensation structures (figure 6.13a). The compensation structures are necessary because of the crystal dependant etch rate of KOH (potassium hydroxide), which would under-etch at the convex corners formed where the connection channels meet the reaction chamber (section 6.2.1.2). A gas flow of 6 sccm Argon and 3 sccm CHF_3 was used for etching the nitride and a gas flow of 25 sccm Argon and 25 sccm CHF_3 was used for etching the oxide. The mask for this etch was a 1.1 µm thick positive photoresist patterned by a third lithography step.

Then, after stripping the resist by ashing, the wafer was immersed into KOH (30%, 70 degC) to etch the reaction chambers and the connection channels. The etching rate is 0.54 µm/min. The (111) planes were used as an etch stop for the connection channels (V-groove), which were just 100 µm deep whereas the depth of the chamber was 400 µm. Thereafter, the nitride and oxide was stripped off with orthophosporic acid at 160 degC and buffered hydrofluoric acid respectively (figure 6.13b).

After that, a 80 nm thick thermal oxide was grown on the wafer. On the back a 20 nm thick film of titanium and a 200 nm thick film of platinum were deposited using an electron gun evaporator with a planetary wafer holder system. Titanium was used as an adhesion layer. The platinum was patterned by argon ion beam milling to form the heater and sensor resistors (figure 6.13c). The ion beam milling stopped within the titanium and the remaining layer was wet etched. This left the underlying oxide undamaged. Positive photoresist was used as the mask for this fourth lithography step.

The next fabrication step involved sawing of a pyrex wafer. 800 µm wide and 800 µm deep trenches were sawn into the 1 mm thick pyrex wafer to form the part of the chip wherein the hypodermic needles or the fused silica capillaries could be glued for the external fluidic connections. The cutting lines were defined by evaporating 40 nm of chromium onto one side of the wafer, pattering the resist and wet etching the chromium, using a ready mixed chromium etchant consisting of 22 % ceric ammonium nitrate and 5 % acetic acid. However, the saw cuts were made on the opposite side to the patterns, which could be seen through the transparent pyrex glass. The reason for that is that the chromium pattern is used as a grid electrode for the later anodic bonding. Experiments showed that the bonding time can be significantly decreased using this grid instead of a single point probe.

The last step before cutting the wafer into single chips was the anodic bonding of the pyrex wafer to the silicon wafer to seal the reaction chambers (figure 6.13d). The wafers were placed on a hot plate and the voltage was supplied by a 2.5 kV power supply. The bonding conditions were 400 degC and 1000 Volt applied for 30 min. The bonding was done under vacuum as bonding in air oxidises the aluminium bond pads making wire bonding impossible.

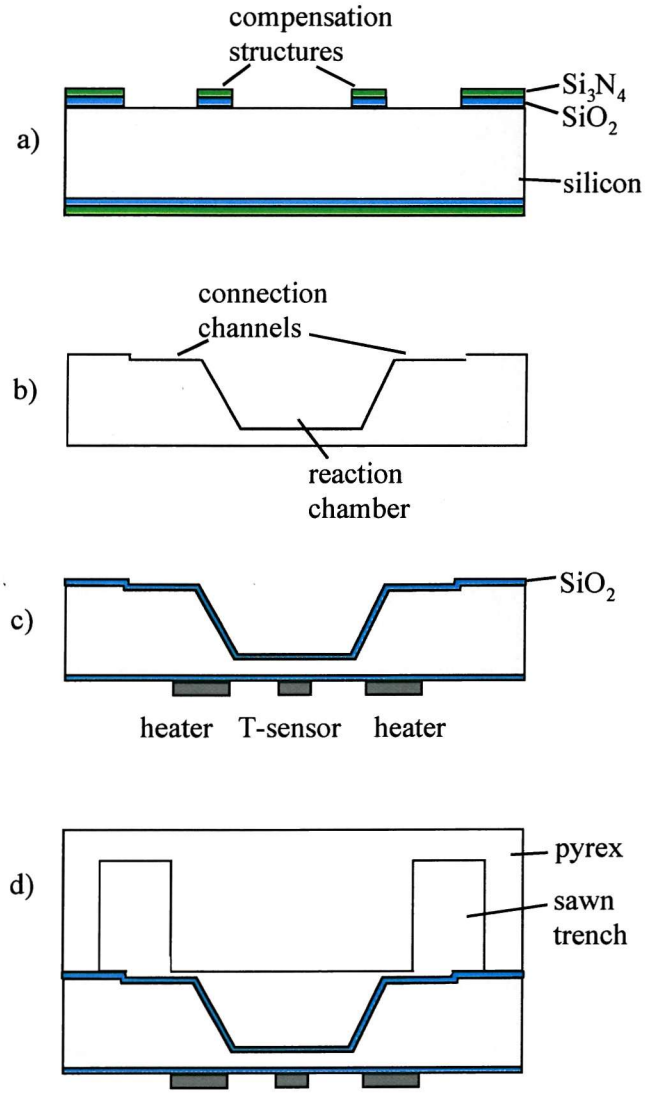

Figure 6.13: Schematic of the fabrication process.

6.2.3 Packaging

For easy handling and for making the power connection to the heaters and sensors, the PCR chip was glued onto a standard 40 PIN DIL ceramic package. As the chip sits upside down on the package because of the wire bonds to the resistors and the external cooling (Peltier cooler), a hole has to be drilled into the bottom of the ceramic package to give optical access to the pyrex part of the chip. A hole of 6 mm diameter was cut using an ultrasonic drill. A second hole of 8 mm diameter was drilled on one side of the package to allow space to crimp and cut the hypodermic needles as close as possible to the chip. A photograph of a packaged PCR chip can be seen in figure 6.14a.

a) b)

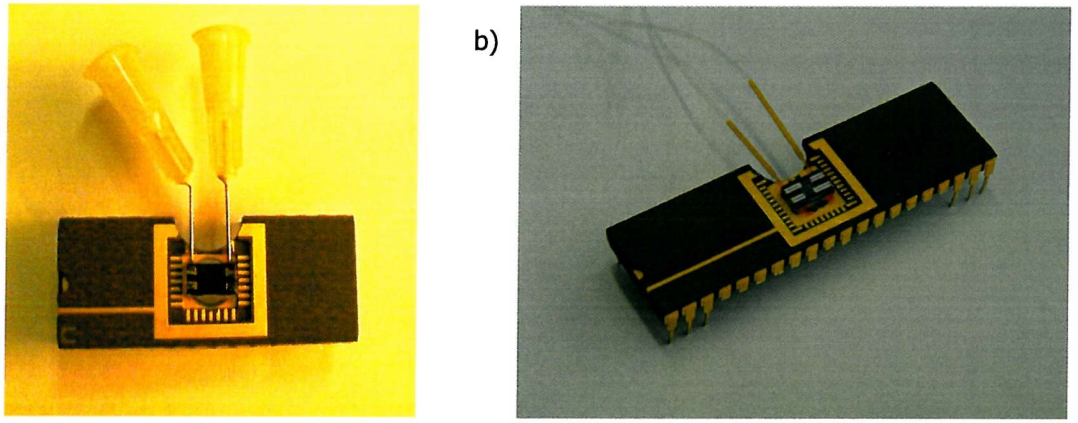

Figure 6.14: Packaged PCR chip: a) hypodermic needles (earlier 28 PIN DIL); b) fused silica capillaries (40 PIN DIL).

Quick set epoxy glue was used to glue the PCR chip onto the package. A template was used for the repetitive exact placement of the PCR chip. This exact placement is necessary because of the narrow light beam used for the optical detection. Gold wires of 25 µm diameter connect the heaters and the temperature sensor to the package.

In a final step, modified (sharp end taken off and metal abraded) hypodermic needles of 0.6 mm diameter from Becton-Dickinson Ltd. were glued into the trenches of the pyrex. RS quick set epoxy glue was used as it proved to be bio-compatible. The PCR solution can be conveniently filled into the chip with a standard syringe. After filling, the needles were sealed off using a crimping tool and after that they were cut to reduce the thermal mass.
Alternatively, fused silica capillaries of 0.4 mm diameter could be glued in with Microposit adhesive, both obtained from Composite Metal Services Ltd. (figure 6.14b). A silicone hose from MERCK Ltd. was placed onto the fibre and after filling the chamber with a syringe, a knot was made into the hose to seal the chip. All the components for this setup proved also to be compatible with PCR. This alternative external fluidic connection was used as the crimping tool damages some of the devices due to mechanical shear forces.

These packaged PCR chips can be placed into the instrumentation box developed by OptiSense Ltd., containing the power connection via a ZIF socket, the cooling arrangement and the detection optics (figure 6.15).

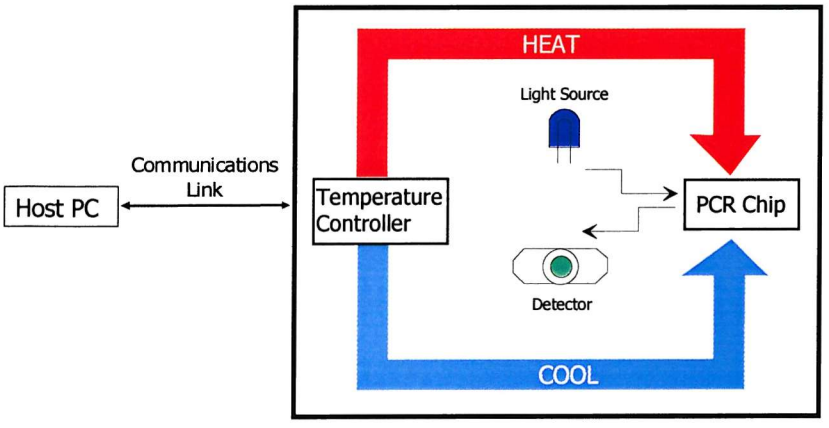

Figure 6.15: Schematic of instrumentation box (after OptiSense Ltd.).

6.2.4 Performance Data

6.2.4.1 Platinum resistors

To evaluate the performance of the PCR chip, the platinum resistors had to be characterised first. To measure the resistance change with temperature, the chip was placed in a temperature controlled oven and the change in resistance was observed. Figure 6.16 shows a linear relationship between the temperature and the normalised change in resistance. For a temperature change of 65 degC, the resistance changes by 12.1 %. The temperature coefficient is given by [Stoe93]:

$$\alpha = \frac{\frac{\Delta R}{R}}{\Delta T} \tag{6.9}$$

With the data from figure 6.16, a temperature coefficient of $\alpha = 1.85 \cdot 10^{-3}\ K^{-1}$ was calculated. The temperature coefficient for bulk platinum is $\alpha = 3 \cdot 10^{-3}\ K^{-1}$ [Weas89]. This difference might be due to the method of deposition or contamination of the thin film.

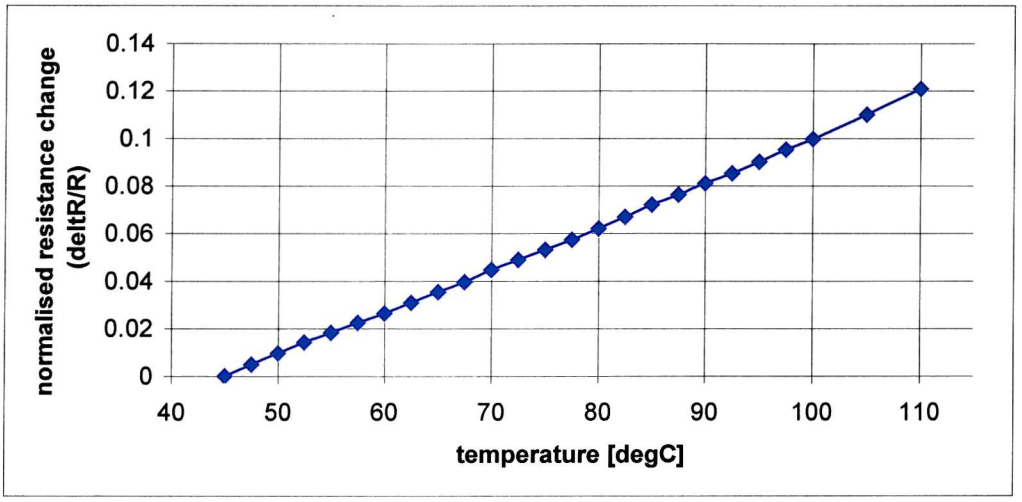

Figure 6.16: Relationship of the resistance change with temperature for the platinum resistors.

6.2.4.2 Time constant

The time constant τ has been evaluated in this experiment. τ is defined as the time necessary for the chip to cool down to 37 % of its initial temperature value. A constant current source of 2 mA was connected to the temperature sensor. Both heaters were connected in parallel. When a voltage was applied to the heaters, the chip heated up. After 30 seconds, the power was switched off and the change in voltage of the temperature sensor due to the change in resistance was recorded with a digital oscilloscope. A schematic can be seen in figure 6.17. The time constant should be small to facilitate fast cooling of the chip.

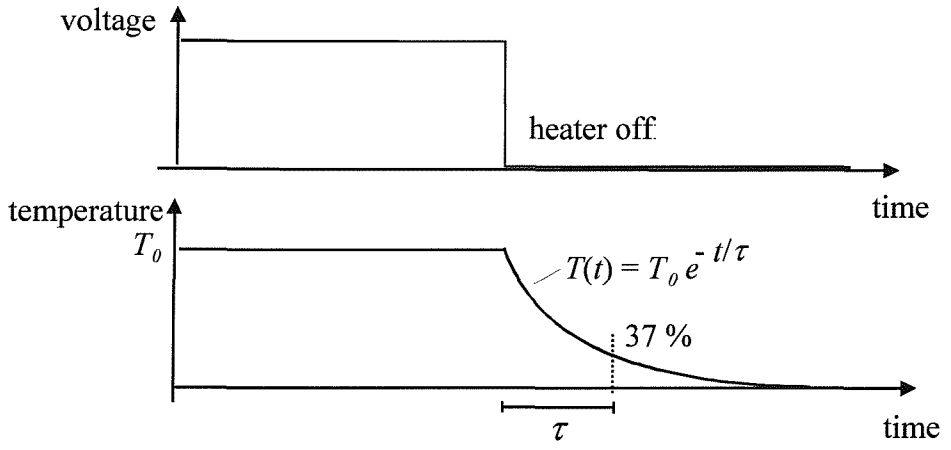

Figure 6.17: Schematic of the time constant measurement.

Table 6.2 shows the measured time constant for a PCR chip with and without water in the reaction chamber. The average time constant for the chip without water was 5.8 seconds and the average time constant for the water filled chip was 7.3 seconds. In section 6.2.1.4, the time constant for a water filled chip has been calculated to be 10.7 seconds. The difference between the calculated and measured time constant is due to heat loss to the surrounding air, which is not included in the calculation. If the heat loss to the air is included, the thermal resistance would become smaller and therefore the time constant would decrease, as seen in the measurement.

	no water	**with water**
power [W]	$\tau_{cooling}$ [sec]	$\tau_{cooling}$ [sec]
0.16	5.8	7.5
0.35	5.8	7.1
0.63	5.7	7.4
1.41	5.9	7.2

Table 6.2: Time constant for PCR chip.

6.2.4.3 Temperature cycles

Minimum and maximum temperature

To cycle the chip between the maximum and minimum temperatures used for PCR, a software controlled lab-card, built by T. E. G. Niblock and reprogrammed by D. Kunz, was used. Power was supplied to the heaters connected in parallel and the temperature was measured with the temperature sensor. When the temperature sensor reached a predetermined value, the power was switched off and when it fell to a second value, the power was switched back on. A fully packaged chip (fused silica tubing, microposit glue and silicone hose) with and without water in the chamber was used.

This two temperature cycle PCR might be used for special applications as described by Kondo [Kond99] and Nagai [Naga99].

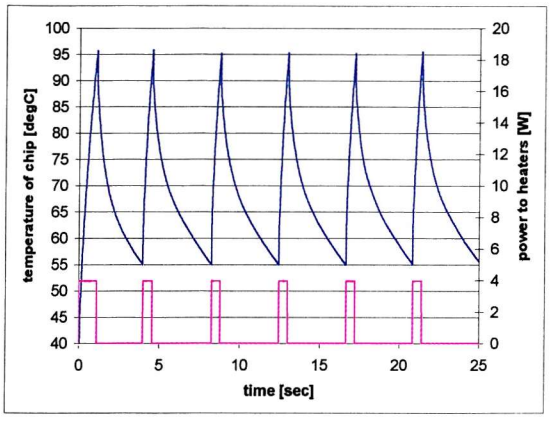

Figure 6.18: Minimum and maximum PCR cycle temperature – chip without water in chamber.

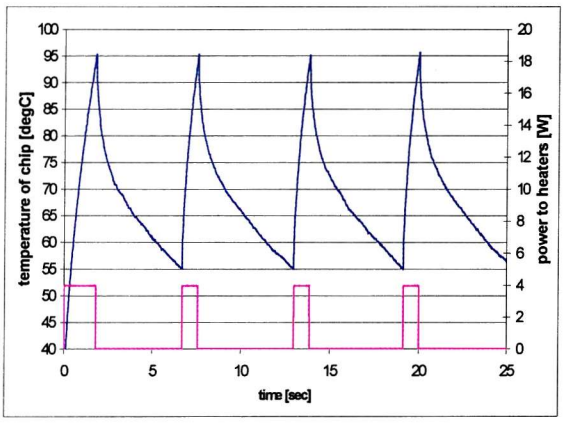

Figure 6.19: Minimum and maximum PCR cycle temperature – chip with water in chamber.

When a power of 3.9 W was applied, the chip without water heated within 0.6 sec from 55 degC to 95 degC (figure 6.18) and the chip filled with water heated within 0.9 sec (figure 6.19). When different amounts of power were applied to the heaters, the chip heated faster or slower as shown in table 6.3. The higher the power applied to the chip, the faster the heating. It was also observed, that the chip cooled faster for higher applied power. This is due to the temperature sensor being very close to the heaters. Therefore, the sensor reaches the set temperature before heat is conducted to other, more distant parts of the chip, and the control unit switches the power off. Experiments with salts melting at specific temperatures, as suggested by Poser [Pose97], can be used to calibrate the time at which the inside of the reaction chamber reaches the temperature necessary for PCR.

For the chip with water, a time of 1.8 sec was measured to heat the chip from 24 degC to 95 degC with a power of 3.9 W. Using equation 6.4 a time of 1.1 sec was calculated with a power of 3.9 W to heat the chip by 71 degC. Heat losses to the surrounding air were not included in the calculation and therefore a longer time was needed to heat the chip.

	unfilled chip			chip filled with water		
power [W]	time heating [s]	heating rate [degC/sec]	time cooling [s]	time heating [s]	heating rate [degC/sec]	time cooling [s]
1.4	1.7	24	5.3	2.6	15	7.2
2.5	0.7	57	4.0	1.2	33	6.5
3.9	0.6	67	3.8	0.9	44	5.5
5.6	0.5	80	3.7	0.7	57	4.9

Table 6.3: Heating and cooling times of PCR chip during temperature cycles from 55 degC to 95 degC.

Forced cooling

The cooling of the PCR chip can be shortened significantly as shown in figure 6.20. During the cooling phase, forced air was blown manually onto the chip shortening the time from 4.9 sec (8 degC/sec) to 1.2 seconds (33 degC/sec). This time can be reduced even further with a controlled cooler as is intended with the instrumentation box to be realised by OptiSensor Ltd.

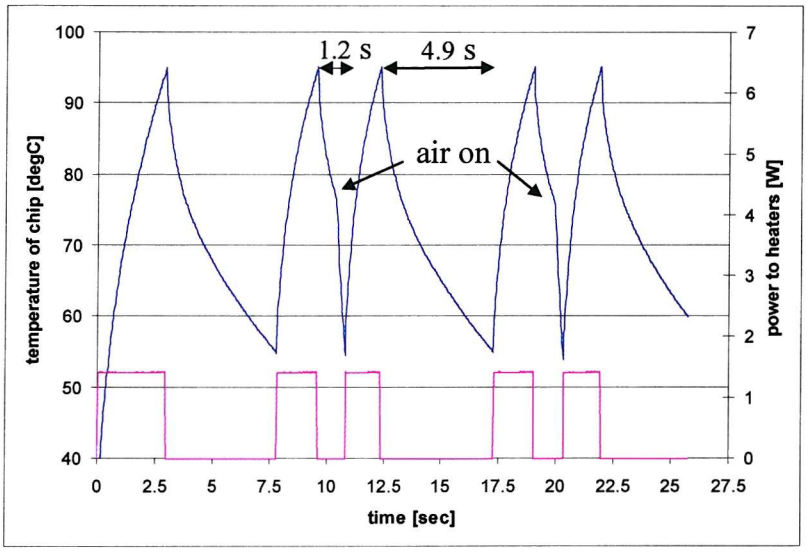

Figure 6.20: Cooling down of the PCR chip with forced air.

DNA amplification equivalent three temperature cycle

To cycle the PCR chip through the three DNA amplification temperatures, the same software controlled lab-card was used. Power was applied to the heaters connected in parallel and the temperature of the chip was measured with the sensor resistor. When the resistor temperature reached a certain value, the power was switched on or off to hold the chip at that temperature. A fully packaged chip (fused silica tubing, microposit glue and silicone hose) without water in the chamber was used for the measurements.

For the graph in figure 6.21 a power of 1.4 W was applied to the heaters. The chip was heated up to 95 degC and then held for 2.5 sec before forced cooling to 55 degC with a cooling rate of 50 degC/sec. The chip was then held at 55 degC for 2.5 sec before being heated up to 72 degC at a rate of 43 degC/sec. The temperature was held at 72 degC for 7.2 sec before the chip was heated again to 95 degC at a heating rate of 24 degC/sec starting a new cycle.

For the graph in figure 6.22 a power of 3.9 W was applied to the heaters. The chip was heated up to 95 degC and then held for 0.4 sec before cooling to 55 degC. This time, the chip was not cooled actively. The chip was then held at 55 degC for 0.4 sec before being heated up to 72 degC at a rate of 131 degC/sec. The temperature was held at 72 degC for 1.2 sec before the chip was heated again to 95 degC at a heating rate of 72 degC/sec starting a new cycle.

The instability in the measurement curves, where the temperature is held at a certain value, is due to the delay between each measurement point. In figures 6.21 the time delay between each measurement point was 25 ms and in figure 6.22 the delay was 15 ms. The power, for example, switches off at 95 degC, however, within the 25 ms/ 15 ms until the next measurement point, the chip already cools down a few degrees before the power is switched on again after the delay time. The same is true for heating. If the power switches on at a certain value, the chip heats up for some degrees before it switches off again. The lab-card is restricted to 1000 measurement points and therefore, the time delay sets the overall measurement time. The higher the power and the longer the delay between the measurement points, the greater the instability. A power of 3.9 W with a time delay of 25 ms results in an instability of 6 degC (figure 6.22). Applying the same power with a shorter delay of 5 ms reduces this to 3.5 degC as can be seen in figure 6.23. The curve at the beginning of the holding temperature at 72 degC, as can be seen in all graphs, is due to the software. The power switches on or off at a value of 72 degC. More sophisticated software and hardware is necessary to control the temperature within the 2 degC required for successful DNA amplification. This is intended to be implemented in the instrumentation box from OptiSense Ltd.

During actual DNA amplification using the PCR, the temperature of the chip would only touch the 95 degC and the 55 degC marks, whereas it is left at the 72 degC mark for two seconds to allow the enzyme to extend the new DNA strand. This time of two seconds is for the short DNA strands this chip is intended to be used for. For longer strands, the time needs to be extended accordingly. The graph in figure 6.24 shows the results for a measurement with 3.9 W applied to the heaters connected in parallel. The chip was fully packaged without water in the chamber. The time delay between the measurement points was 25 ms. The chip was actively cooled by forced air from an air duster can. The holding time at 72 degC was 1.8 seconds. Heating rates of 57 degC/sec between 55 degC and 72 degC and of 71 degC/sec between 72 degC and 95 degC were achieved. The forced cooling was between 44 degC/sec and 73 degC/sec, depending on the time the air was switched on. Within the 25 seconds of measurement, seven cycles could be completed.

Taking into account the 1.5 times longer heating rate when the chip is filled with water and assuming that the forced cooling would be 1.5 times slower, the total time for 1 cycle would be approximately 4.4 seconds. Therefore, PCR with 30 cycles in 2.2 min could be facilitated.

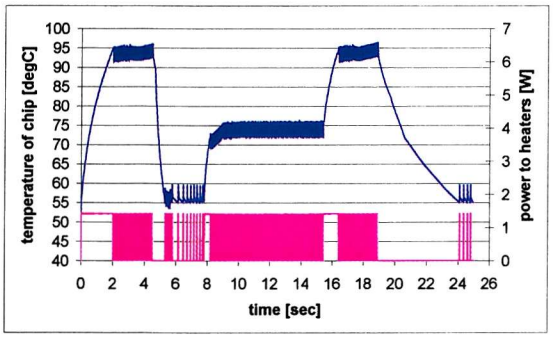

Figure 6.21: Three point temperature cycle with a power of 1.4 W and forced cooling. Delay time 25 ms.

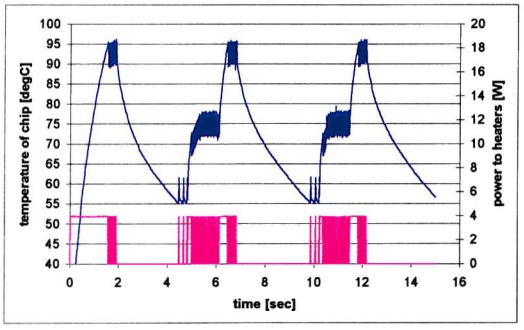

Figure 6.22: Three point temperature cycle with a power of 3.9 W and passive cooling. Delay time 15 ms.

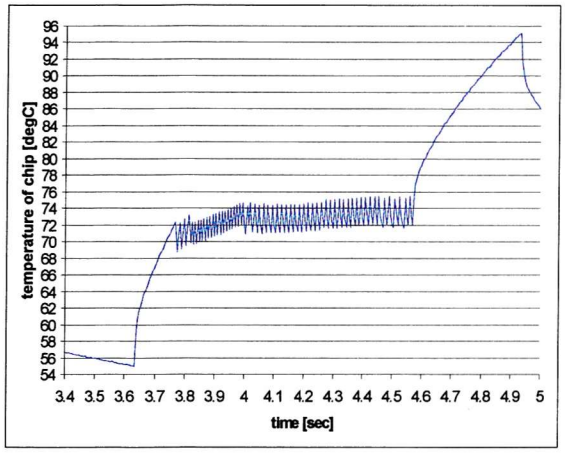

Figure 6.23: Three point temperature cycle with a power of 3.9 W and 5 ms delay time.

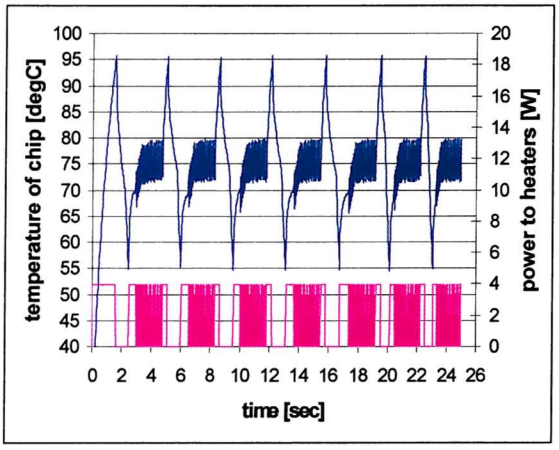

Figure 6.24: Three point temperature cycle with a power of 3.9 W and forced cooling. Delay time 25 ms.

6.2.5 Conclusion

Micromachined reaction chambers based on silicon and pyrex for the thermal cycling of DNA by the polymerase chain reaction have been fabricated and tested. The principle of amplification is explained in appendix A. Obvious advantages are the small size, the low power consumption, the possibility of using optical detection methods, the fast temperature cycling, the low cost fabrication and the portability of the device.

The PCR chip is mounted onto a 40 PIN DIL package for power connection and easy handling. The package can be placed onto a ZIF socket, which slides into the instrumentation box from OptiSense Ltd. Bio-compatibility tests have been done by DERA and none of the materials of the micromachined PCR chip in contact with the reaction cocktail showed any inhibition with the PCR.

The resistance of the evaporated platinum resistors changes linearly with temperature, although the temperature coefficient is lower than that of bulk material. It is assumed that this is due to the method of deposition and contamination. The time constant was measured to be 7.3 seconds for a packaged and water filled chip. Measurements of cycling the PCR chip between the maximum and minimum amplification temperatures have been carried out. The intended 3.9 W power from the instrumentation box applied to the heaters in parallel causes a temperature rise of 44 degC/sec for a water filled chip. Forced cooling of the chip with air from an air duster enabled a cooling rate of 33 degC/sec. Controlled cooling, as is intended with the instrumentation box by OptiSensor Ltd., would increase the rate significantly.

Cycling the PCR chip between the three distinct temperatures required for PCR was demonstrated and it was shown that the temperature could be held at fixed certain temperatures. For a water filled chip a time of 2.2 min for 30 cycles is estimated.

Nowadays the PCR is the most common method for DNA amplification in many different applications areas such as medical, forensic and environmental screening. Therefore, fast and small single shot devices, which can be taken into the field offer an enormous market potential.

Real DNA amplification using the micromachined chip could not be presented as the instrumentation box containing the necessary software and hardware was significantly delayed and therefore experiments could not be carried out.

6.3 Optical Detection Integrated into the PCR-chip

Optical detection is a powerful and important method for analyzing biological reactions. To monitor the progress of the polymerase chain reaction fluorescence detection is used, which has the great advantage of monitoring the PCR in-situ. A fluorescent dye, which must be compatible with the PCR and must not inhibit the reaction, is added at the start of the process. Several dyes have been found to be suitable for this purpose [Witt97], including fluorescein, which is excited at a wavelength near 480 nm, and Cy5.5, which may be excited near 633 nm. An overview of optical reporting chemistries for real-time quantitative PCR, based on an internal DERA report by M. Lee, is given in appendix B.

To enhance the micromachined PCR chip further, optical fibres and a pn-diode have been integrated into it, thereby avoiding bulk-optical components. Two major designs have been fabricated and tested. The first design uses two optical fibres, one for the projection of light into the chamber and the other for the collection of the light emitted by a fluorescent dye out of the reaction chamber. The second design employs a single optical fibre for the delivery of light into the PCR chamber, with light now being detected using a photodiode integrated into the base and walls of the reaction chamber within the PCR chip. Both attempts would allow a silicon lid to replace the present transparent pyrex lid, rendering the detection system immune from ambient light. The filling of the chamber in this case could be done through fused silica capillary tubes, which are available in very small diameter, placed in V-grooves on the side of the silicon chip instead of the sawn trench in the pyrex.

The feasibility of using an LED or a HeNe laser as the system light source has been assessed. Using a HeNe laser as the light source, the scattering of light within the chamber has been investigated. Basic I-V characteristics for the photodiode under blue light illumination have also been obtained. Finally, the effect on the photodiode performance of the anodic bonding of a pyrex lid at an elevated temperature has been examined.

6.3.1 Design

The fluorophore dye fluorescein to be used for the PCR analysis requires an excitation light source to emit in the wavelength region of 460 – 480 nm. An ultra bright blue LED emitting at 470 nm (Marl Optosource Ltd.) was chosen as the light source due to its low cost, high output power, small size and simple operation. Graded index multimode fibres with a numerical aperture of 0.2, a core diameter of 50 μm and a cladding diameter of 125 μm were used, allowing effective collection of light from the LED and from fluorophores.

V-grooves (270 μm wide and 190 μm deep) were included in the design layouts of the PCR chip (figure 6.25) to hold the optical fibres. The input and output fibres were placed perpendicular to each other to prevent direct illumination of the output fibre by the input light, while allowing sufficient capture of the fluorescent emission. For the KOH etching, compensation structures as described in section 6.2.1.2 were added as depicted in figure 6.25.

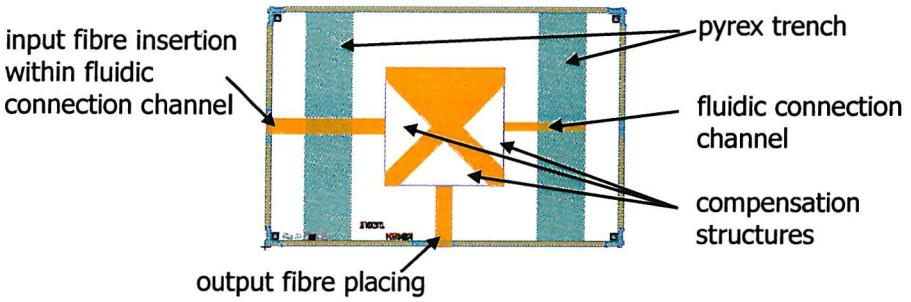

Figure 6.25: Schematic of the chip design: added V-grooves and compensation structures for KOH etching.

For the cell with the integrated diode detector only one optical fibre is used (figure 6.27) and the fluorescent emission is detected by an implanted pn-junction. The dimensions of this photodiode are 2 mm x 2 mm. Electrical contact to the diode is made via the base of the chip and the metal track and pad on the top of the chip. Contact to the top metal pad is made via the end of the pyrex trench, as shown in figure 6.27, the opposite side of which is used for the external fluidic connection with a glued hypodermic needle.

Three conventionally-sized photodiodes (60 μm x 60 μm) have been included for reference measurements (see figure 6.27).

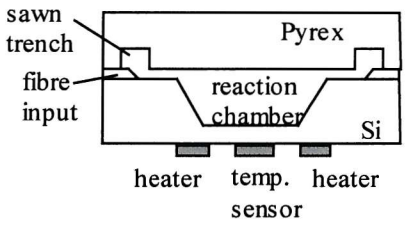

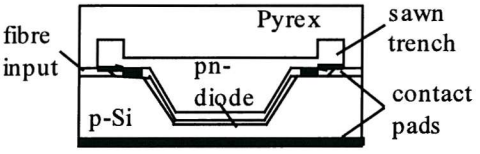

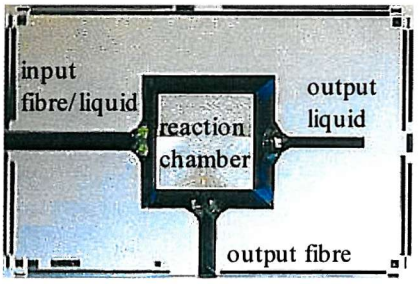

Figure 6.26: Schematic and photograph of the cell layout prior to lid bonding. Chip size: 6 mm x 4 mm.

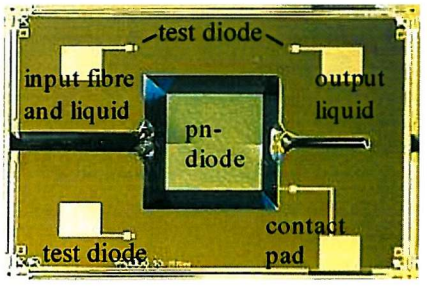

Figure 6.27: Schematic and photograph of the diode detector prior to lid bonding. Chip size: 6 mm x 4 mm.

Fluorescein has an emission wavelength of 520 nm. The penetration depth in silicon of light with λ = 520 nm is ≈ 0.75 μm [Wils89]. To maximise the efficiency of the diode, the junction depth needs to be as shallow as possible. This minimises the incidence of recombination. For ion implanted layers, the implanted profile is Gaussian [Sze88] (figure 6.28).

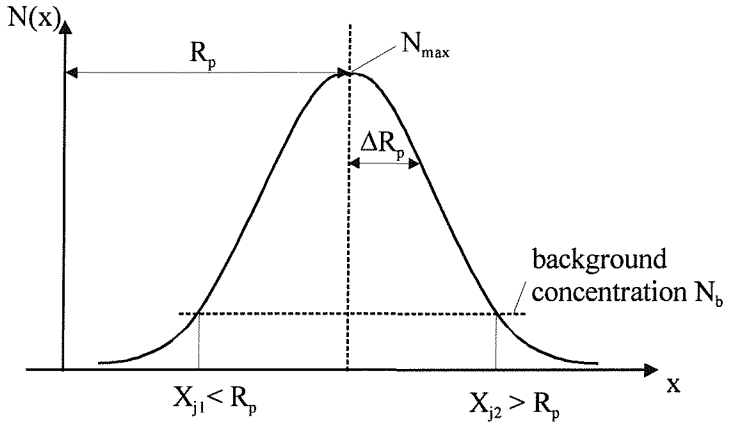

Figure 6.28: Gaussian distribution.

Hence, the profiles are of the form [Sze88]:

$$N(x) = N_{max} \cdot e^{-\frac{\Psi^2}{2}} \tag{6.10}$$

where $N(x)$ is the bulk doping concentration at a depth x from the surface. Ψ is defined as:

$$\Psi = \frac{|(x - R_p)|}{\Delta R_p} \tag{6.11}$$

N_{max} is the peak value of the bulk doping concentration and can be evaluated using:

$$N_{max} = \frac{C_s}{\Delta R_p \cdot \sqrt{2\pi}} \tag{6.12}$$

R_p is the projected ion range, ΔR_p is the standard deviation in this parameter and C_s = $1 \cdot 10^{16}$ cm^{-2} is the number of ions impinging on the unit area of the surface. Values of 0.032 µm for R_p and 0.014 µm for ΔR_p, for a given implantation energy of 50 keV, when implanting arsenic into silicon have been obtained from range data tables [Smit79]. The junction depth is where $N(x)$ equals the background concentration N_b = $1 \cdot 10^{15}$ cm^{-3} of the p-type silicon wafer. Dividing N_b by N_{max}, using equation 6.12 to calculate N_{max}, enables a value for Ψ = 5.4 to be found using the Gaussian distribution table [Smit79]. The value of the junction depth x is then calculated using equation 6.11. The ions are implanted through a 40 nm thick oxide layer where the projected range R_{pox} = 0.043 µm. Therefore, N_{max} is at the surface between the oxide and silicon. Hence the junction depth is calculated by $x = \Psi \cdot \Delta R_p$ = 75.6 nm. After the implantation, the oxide is stripped off and a new 80 nm thick oxide layer is grown. A layer of $0.44 \cdot d_o$ of silicon is consumed when an oxide layer of thickness d_o is formed [Sze88], thus bringing the junction depth closer to the surface. However, at the same time, the high temperature (950 degC) during the oxidation causes the arsenic to diffuse.

To obtain a more accurate result for the junction depth, ATHENA simulations have been carried out. Within the computer program, a 40 nm thick oxide is grown and arsenic is implanted under the same conditions as used for the calculation into a p-type silicon wafer as

can be seen in figure 6.29a. N_{max} is at the oxide/silicon interface as predicted. The concentration difference of the dopants at the oxide/silicon interface is due to segregation. After the ion implantation, the junction depth is at 101 nm.

Then the oxide is stripped off (figure 6.29b) and a new oxide is grown causing diffusion of the dopants and silicon consumption (figure 6.29c). The junction depth is at 53 nm. The tip within the boron line is typical for boron-arsenic combinations [Will78]. The simulation program, however, is not calibrated for oxide and therefore, the results are not accurate within the oxide layer. However, the tendency is shown and the difference at the oxide/silicon interface is also due to segregation.

The simulation shows that the junction depth will be close to the surface and hence light of λ = 520 nm can be detected (silicon dioxide is transparent for this wavelength).

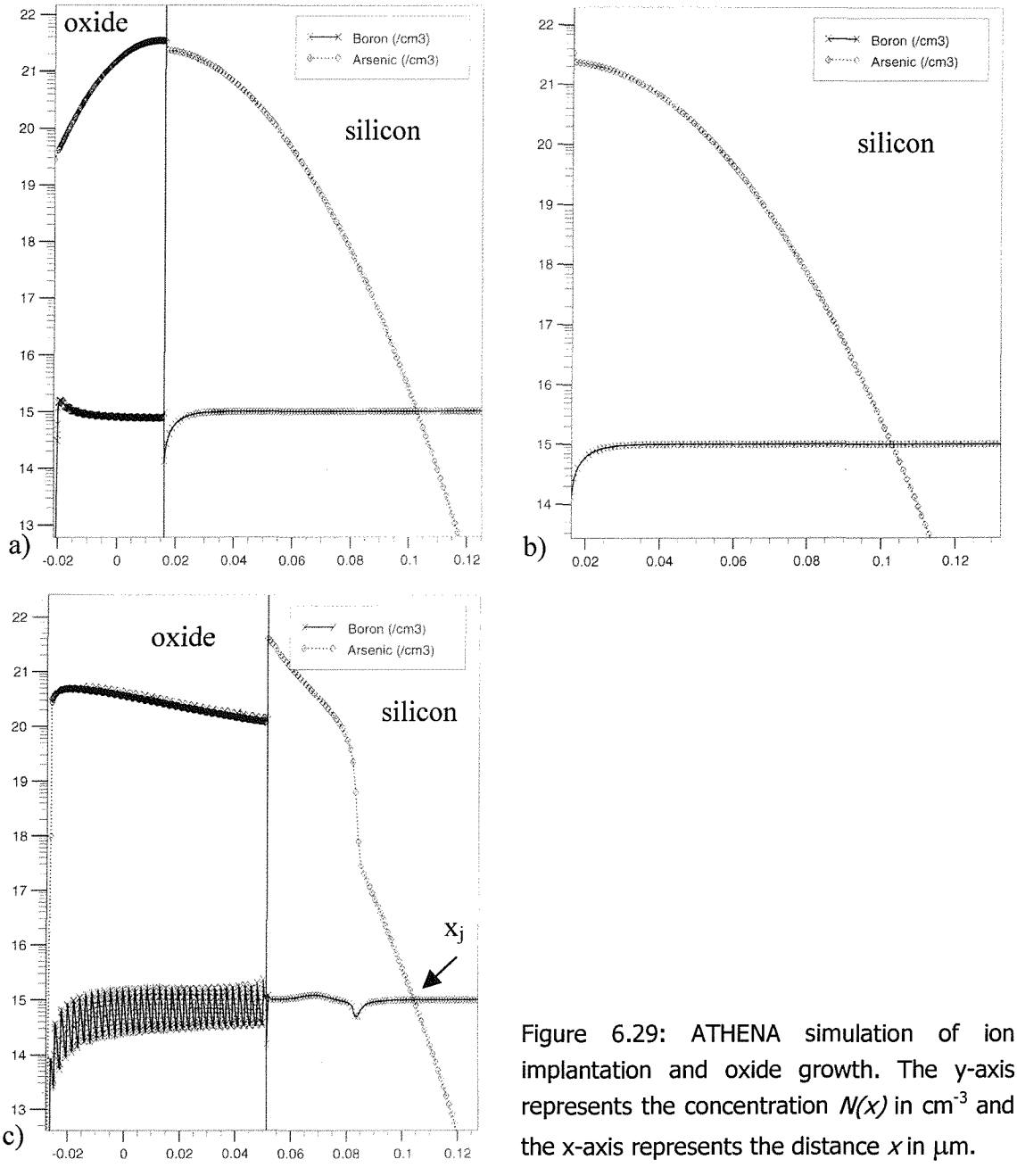

Figure 6.29: ATHENA simulation of ion implantation and oxide growth. The y-axis represents the concentration $N(x)$ in cm^{-3} and the x-axis represents the distance x in µm.

6.3.2 Fabrication

For the fabrication of the PCR chip with pigtailed fibres, the wafer was covered with an oxide and nitride layer. Patterning photo resist and dry etching the nitride/oxide layers left the mask for etching the reaction chamber and the connections for fluids and fibres. With the aid of compensation structures and the (111) planes of the silicon lattice the structures were etched into the wafer with KOH. The nitride and oxide films were then stripped from the wafer and a 80 nm thick thermal oxide was deposited as an insulation layer for the resistors on the back surface. Platinum, with titanium as an adhesion layer, was used for the resistors and both metals were structured by ion beam milling.

Pyrex was used as a lid for the PCR chip. A 40 nm thick chromium layer was patterned on top of the pyrex wafer. The patterned chromium film serves two functions. First it was used as a guideline for sawing trenches into the wafer for the external fluidic connections and secondly, it enhances the anodic bonding procedure in creating an electrode mesh. Compared to a single-point contact, anodic bonding can be completed in a significantly shorter time [Ito95].

The fabrication process for the device incorporating an integrated diode required additional steps. A p-type silicon wafer was used. A boron implantation onto the back ($5 \cdot 10^{15}$ cm^{-2}, 50 keV) was implemented to assist the ohmic contact to the metal at a later stage. After the creation of the reaction chamber and the fluid/fibre channels using KOH, arsenic was implanted ($1 \cdot 10^{16}$ cm^{-2}, 50 keV) through an oxide layer of 40 nm thickness to form the pn-diode. This oxide was then stripped off and a new oxide of 80 nm thickness was thermally grown to isolate the metal tracks for the diode connection and to act as an anti-reflection coating. The oxide was patterned with buffered hydrofluoric acid to create contact windows to the silicon. Layers of titanium and aluminium/silicon were then sputtered on the front and back of the wafer and patterned on the front to produce the metal tracks. The pyrex lid was fabricated and bonded to the silicon as described above.

6.3.3 Assembly

The assembly procedures for the designs with and without the diode detector were essentially the same. The protective polymer coating was removed from the ends of the optical fibres, which were then glued into the V-grooves on the sides of the silicon chip. Modified hypodermic needles were glued in the trenches sawn into the Pyrex glass lid. The glue used was RS quick set epoxy, which has proved to be biocompatible. The chip was then placed on a DIL package to ensure easy handling. A photograph of an assembled device is shown in figure 6.30.

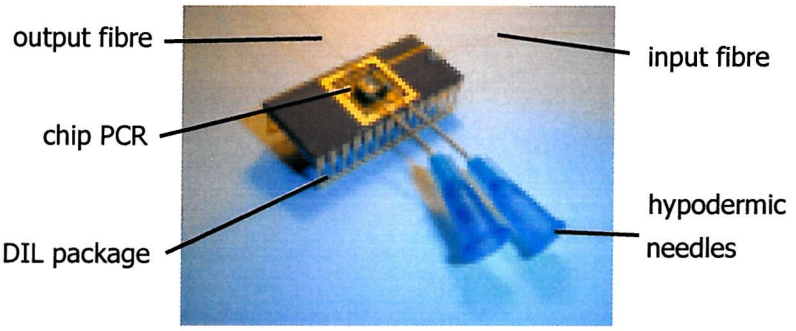

Figure 6.30: Photograph of an assembled device with two pigtailed optical fibres.

6.3.4 Test Procedures and Results

6.3.4.1 Pigtailed optical fibres

Initial tests on the chamber were carried out to characterise the optical performance. First the power emitted by the LED coupled to the optical fibre was measured over a range of drive voltages and the results are shown in table 6.4.

5V	4.5V	4V	3.5V	3V	2.5V
0.587 μW	0.445 μW	0.305 μW	0.167 μW	35.1 nW	5 nW

Table 6.4: Relationship between applied voltage at the LED driver circuit and emitted light at the end of the optical fibre.

Connection between the input fibre and the LED was carried out by drilling a small hole in the LED's lens housing as close as possible to the emissive area and gluing the fibre in place using an index matching glue. With 5 Volts applied to the LED driver circuit, the power emitted from the uncoupled LED was 6.86 mW and the light emerging from the end of the LED coupled to the fibre was 0.587 μW, representing a coupling efficiency of 0.009%. Tests using a microscope objective lens enabled 10 μW (0.15 %) of light to be coupled into the fibre.

Tests of the design were carried out with full fat milk in the chamber. The milk was intended to scatter the light effectively throughout the chamber and thereby enable some of the light to enter the collection cone of the output fibre. Light was observed visually entering the reaction chamber (figure 6.31), however, no light was measured at the end of the output fibre with a photodiode connected to an oscilloscope.

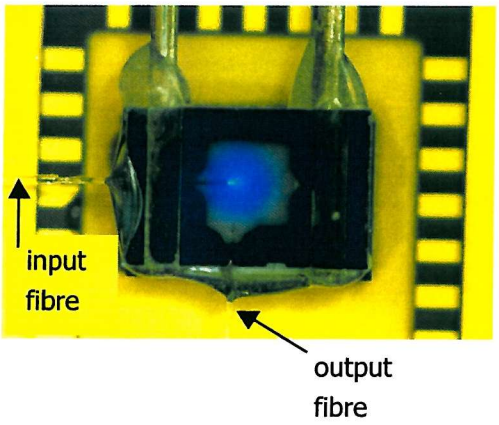

Figure 6.31: Scattering of blue light in milk.

The level of excitation power was insufficient to obtain a measurable signal at the output fibre, so an HeNe laser emitting 4.1 mW at λ = 633 nm after coupling the light into the fibre, was used for further experiments, allowing accurate measurements to be made. The benefits of using the laser include the high coupling efficiency of 66 % into the optical fibre, using lenses, and the ready availability of the fluorescent dye Nile Blue A Perchlorate whose absorption spectrum closely matches the operating wavelength of the laser. This dye has a maximum excitation wavelength of 628 nm and an emission wavelength of 670 nm.

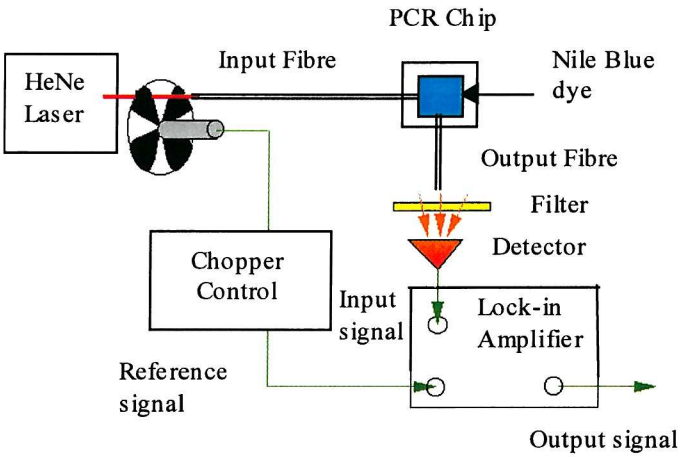

Figure 6.32: Schematic of the measurement apparatus.

Tests were conducted using the experimental apparatus shown in figure 6.32, which was set up during a final year project by J. Pollard. The output of the laser was chopped at about 1kHz before being coupled into the input fibre with a lens. The light emitted from the output fibre was passed through a wavelength filter to remove scattered pump radiation at 633 nm and detected using a silicon photodetector with the aid of a lock-in amplifier to improve the signal-to-noise ratio. The aim of the first test, for which the filter was removed, was to check the capture of scattered light within the reaction chamber filled with diluted milk of varying dilution. Particles in the milk scatter the input radiation, allowing confirmation of system operation before carrying out tests with fluorescent dyes. The results in figure 6.33 show that with concentrations above 60 %, the milk scattered measurable power into the acceptance

cone of the output fibre. It may then be concluded that if fluorophores in the collection volume of the output fibre absorb pump radiation and emit fluorescence isotropically this will be detected, assuming sufficient signal-to-noise ratio.

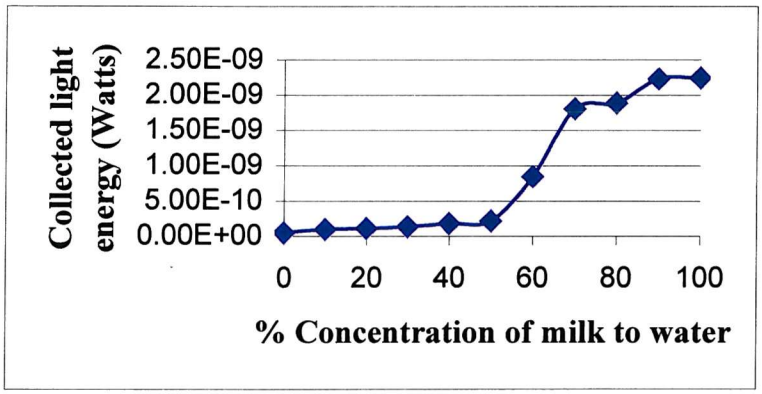

Figure 6.33: Detected scattered power against concentration

Tests were then carried out using a 5 mM solution of Nile Blue A Perchlorate in water. In this experiment an input power from the laser of 4.135 mW yielded an output power from the fluorescent dye of 0.55 nW. Pump radiation at 633 nm entering the external photodetector was eliminated by the filter and by the perpendicular arrangement of the fibres. A range of dye solutions showed that this concentration gave the maximum fluorescent signal. It is believed that the collected power does not increase with higher concentrations of the dye as the pump radiation is absorbed strongly before reaching the collection cone of the output fibre. This result shows that monitoring the PCR reaction using optical fibres inserted into the cell is feasible.

6.3.4.2 Diode detector

The chamber photodiode was tested using the multimode fibre connected to the ultra bright blue LED described above. As the purpose of these experiments was to confirm the correct operation of the photodiodes and to obtain their characteristic curves, they were carried out with direct illumination from the LED. I-V characteristic curves for the diodes were obtained using a Hewlett Packard 4155A four-probe analyser. The characteristics of the three conventionally-sized test diodes were measured to provide valuable information in the comparison of the chamber photodiode characteristics and performance. Measurements of the bare diodes, and of the diodes after anodic bonding of the lid, were taken. The bonding conditions were 400 V at 400° C for 45 min. First, the characteristic of the large chamber photodiode (2 mm x 2 mm) was compared to a test diode characteristic. The results can be seen in figure 6.34, which show a softer breakdown knee for the large photodiode. However, the diode has low reverse leakage and can be readily used for light detection.

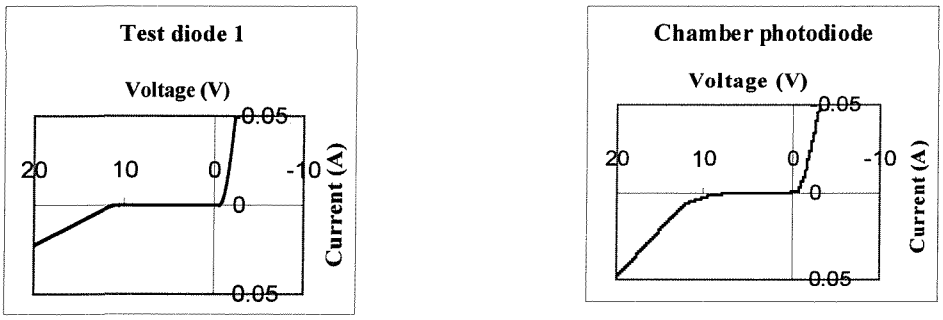

Figure 6.34: Dark current I-V characteristics for chamber photodiode and test diode 1.

The measured leakage current density of the large 2 mm x 2 mm camber diode is $2 \cdot 10^{-8}$ A cm^{-2}, which is close to the current density of 10^{-9} stated for a good diode [Sze81].

The total current in forward bias for small voltages ($U < 1$ Volt) is a combination of the depletion region recombination component and the neutral region recombination component as depicted in figure 6.35 [Pulf89]. For an ideal current-voltage relation in the forward direction, the rate of rise of the depletion region current at 300 Kelvin is 119 mV for every decade change of current. The rate of rise of the neutral region current at 300 Kelvin is 59.5 mV for every decade change of current [Sze81]. The measured change per decade for the large 2 mm x 2 mm intra-cell diode was 110 mV below 0.3 V (figure 6.37). It might be assumed that the depletion region recombination component is dominant for voltages below 0.3 V. For higher voltages, the curve flattens, which is due to series resistance as depicted in figure 6.36 [Pulf89]. The measured series resistance of 117 Ohm above 0.8 Volt (figure 6.37) can be due to the thickness of the silicon wafer (~ 4 Ohms with ρ_r = 15 Ohm·cm), as the diode is contacted from the back, or contact resistance to the diode (~ 110 Ohms).

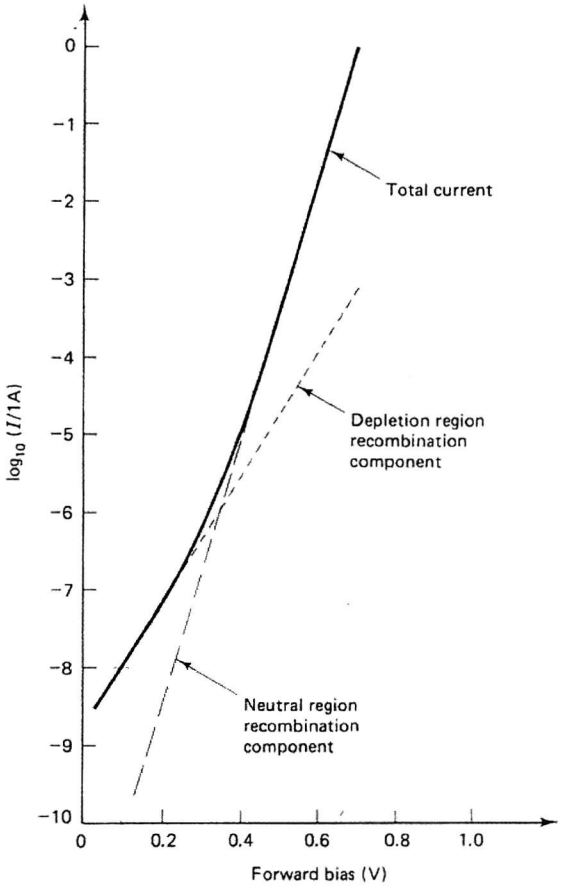

Figure 6.35: Computed forward-bias characteristic for n^+p diodes [Pulf89].

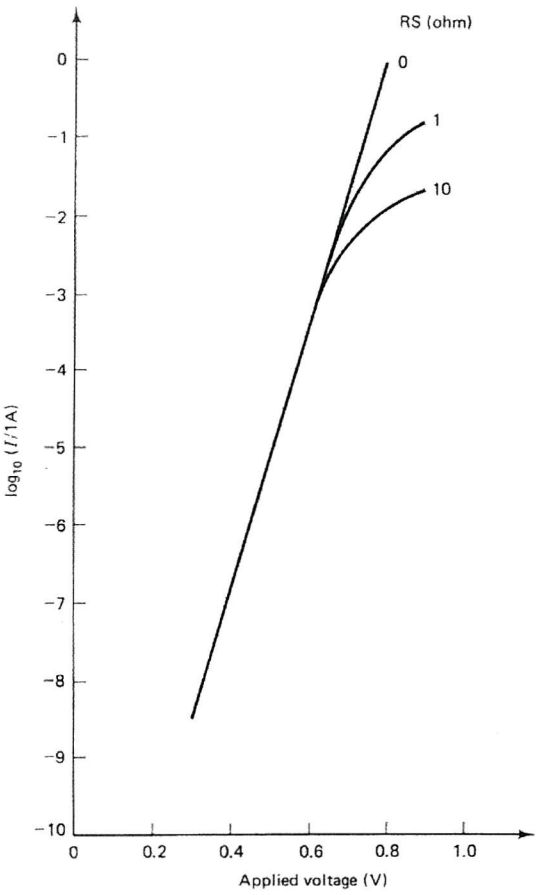

Figure 6.36: Computed forward-bias characteristic illustrating the effect of series resistance [Pulf89].

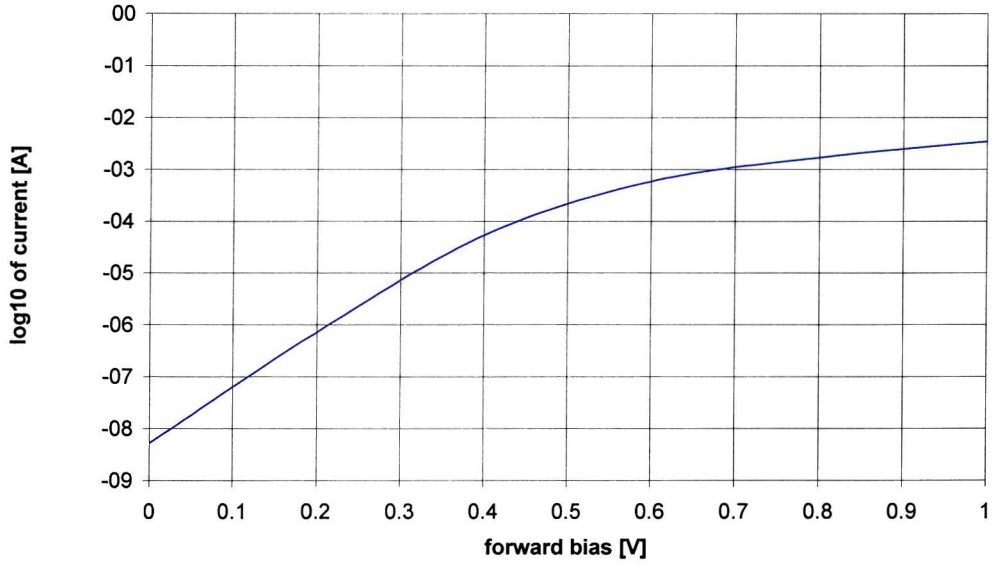

Figure 6.37: Measured forward-bias characteristic for 2 mm x 2 mm chamber diode.

The change in the photocurrent produced by the chamber photodiode generated by different light levels emitted from the fibre-coupled LED was then measured. As stated above, due to the poor coupling efficiency of the LED to the fibre, the light levels are very low. Nevertheless, these low light levels are comparable to the rather low light levels expected from fluorescent emission in the final systems and simulate the proposed application well. The low light levels emitted from the fibre-coupled LED were strong enough to generate a small change in the photocurrent produced by the chamber photodiode, as shown in figure 6.38. The voltage indicated in the legend is the voltage applied to the LED driver circuit, and the respective LED power at the fibre end is given in table 6.4.

A general characteristic of a photodiode is its quantum efficiency η, which is the number of electron-hole pairs generated per incident photon and is given by [Sze81]:

$$\eta = (I_P / q) / (P_{opt} / h \cdot v) \tag{6.13}$$

where I_p is the photogenerated current by the absorption of the incident optical power P_{opt} at a wavelength λ, h = $6.63 \cdot 10^{-34}$ J·s is the Planck constant, q = $1.602 \cdot 10^{-19}$ C is the elementary charge and $v = c/\lambda$ is the photon frequency, with $c = 3 \cdot 10^8$ m s^{-1}.

Using the results from the measurements shown in figure 6.38, an optical power of P_{opt} = 0.587 nW (λ = 470 nm) gives a photocurrent of I_p = 90 nA, which results in a quantum efficiency of η = 0.41. An ideal photodiode has a quantum efficiency of η = 1. However, in a real photodiode, not every photon generates a measurable electron-hole pair as recombination occurs within the depletion region.

A characteristic of commercial photodiodes is the sensitivity $S = I_p / P_{opt}$. The measurement with the values given above results in a sensitivity of S = 0.15 A W^{-1}. A commercially available silicon photodiode from Hamamatsu (S1336 series) has a sensitivity of S = 0.24 A W^{-1} at a wavelength of λ = 470 nm. In table 6.5 the photocurrent, the optical power, the quantum efficiency and the sensitivity are given for the various LED driver voltages used for the experiment.

It can be concluded that the chamber photodiode is of good quality. However, the results for the measurements using the 2.5 V and 3 V LED drive voltage settings are above the theoretical possible limit. This might be due to a slightly different setting on the voltage supply to the LED resulting in a higher optical power than that listed in table 6.4, which were used for the above calculations. Also possible is an error from the optical power meter at these low light levels.

LED driver voltage [V]	2.5	3	3.5	4	4.5	5
I_p [nA]	46	49	54	71	78	90
P_{opt} [nW]	5	35	167	305	445	587
η	24.3	3.7	0.855	0.615	0.463	0.405
S [A W^{-1}]	9.2	1.4	0.32	0.23	0.18	0.15

Table 6.5: Characteristic parameter of the photodiode.

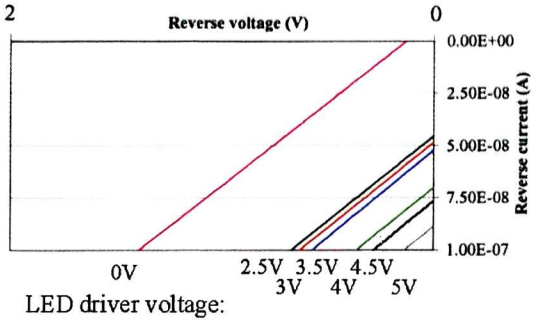

Figure 6.38: Photocurrent from the chamber photodiode.

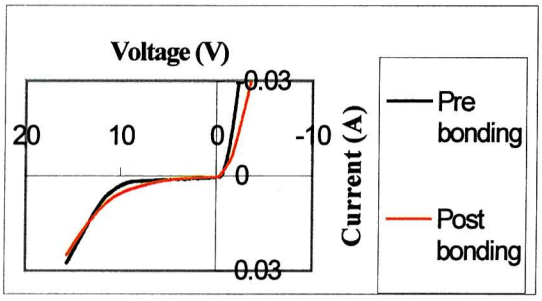

Figure 6.39: Effect of anodic bonding upon the performance of the illuminated photodiode.

Finally, the influence of anodic bonding upon photodetector performance was investigated. Figure 6.39 shows the photocurrent before and after bonding. The results indicate that the anodic bonding process degrades the diode's I-V characteristic. A marked increase in the diode series resistance was observed, as was a noticeable softening of the breakdown knee. Nevertheless, it is anticipated that the diode can still be used for light detection.

6.3.5 Conclusion

Two methods using pigtailed optical fibres and a diode detector for the direct detection of PCR amplified DNA have been presented. An LED and a HeNe laser were assessed as light sources for the PCR micro system. If the blue LED is to be used, a high light coupling efficiency, as offered by specialist companies, to the optical fibre needs to be implemented.

The feasibility of using optical fibres for intra-cell excitation and collection of fluorescent light has been demonstrated. The scattering and capture of light within a chamber containing diluted milk as a scattering source was evaluated. Further tests have been carried out collecting fluorescent light from a dye within the reaction chamber excited by a HeNe laser.
The diode detector integrated within the PCR reaction chamber has been tested with a blue LED coupled to a multimode optical fibre. Successful operation of a large-area intra-cell diode has been demonstrated and the influence of anodic bonding of the pyrex lid has been studied.

It has been demonstrated that optical fibres and a photodiode can both be successfully integrated within the micromachined PCR system and detection of fluorescent emission is feasible.

CHAPTER 7

Conclusions and Suggestions for Further Work

7.1 Conclusions

The aim of the work was to realise microfluidic devices for integrated bio/chemical systems. Such systems have the potential to be an important part of the booming bio/chemical industry and market. Several discrete microfluidic devices were developed with the focus on integration along with an interconnection method to form versatile fluidic systems.

Only a few silicon micropumps tolerant towards gas bubbles, which severely deteriorate the pump's performance, have been presented so far. For a reliable microfluidic system, such a pump is very desirable. None of the published pumps have the potential to be mass-fabricated. In this thesis, an improved pump able to pump gases and liquids is presented. The pump is also tolerant towards gas bubbles of up to three times the pump chamber volume [Scha01a]. The pump is designed so that it is possible to apply the mass-fabrication technique developed by Koch [Koch97b]. Another novel feature of the pump is the self-alignment of the valve wafer to the membrane wafer. The size of the pump is 12 mm x 12 mm with a height of 0.85 mm and it employs dynamic diffuser/nozzle valves. This is the first time that a gas/liquid micropump has been presented, which is tolerant towards gas bubbles, is self-aligning and has the possibility of employing mass fabrication of the piezoelectric membrane actuator.

In order to achieve gas pumping, the compression ratio within the pump chamber has been increased from ε = 1:373 for the previous design [Koch98b] to ε = 1:6. This has been achieved by manufacturing the valve wafer so that it slides into the membrane wafer, thus decreasing the dead volume within the pump chamber. Furthermore, the stroke volume of the PZT actuator was increased by changing the shape of the membrane. A pump rate of 1500 µl/min for ethanol as liquid was obtained at a frequency of 2.5 kHz and a voltage of 190 V_{pp}. Under the same conditions, a backpressure of 1000 Pa was achieved. The pump showed tolerance towards gas bubbles of approximately 14 µl in size for a chamber volume of 4.3 µl. Gas pumping was achieved at a frequency of 3.4 kHz and an actuation voltage of 300 V_{pp} resulting in a pump rate of around 700

µl/min. The measurement technique used for gas pumping can be improved to obtain more accurate results for the pump rate and to measure the backpressure. Suggestions are made in section 3.5.3.2.

For controlling the output of the micropump a flow sensor is necessary and would lead to integrated microfluidic systems. A flow sensor based on the thermal principle has been fabricated. The sensing elements of the flow sensor are suspended on a nitride bridge over a flow channel. As standard LPCVD silicon-nitride has high tensile stress, a method of depositing low stress nitride was desirable. Several methods for depositing silicon-nitride were investigated. The various deposited silicon-nitride films were characterised using an ellipsometer and the data were compared to data found in the literature. Tests showed that silicon-rich-nitride films gave the best results. The flow ratio for the silicon-rich-nitride film used for the realisation of the flow sensors was dichlorsilane to ammonia of 8.6:1 compared to a flow rate of 1:4 for standard nitride. The size of the flow sensor is 4 mm x 7.5 mm with a height of 1 mm. The flow measurement channel is 2.1 mm long, 280 µm/580 µm wide and 100 µm high. Initial measurements show the successful fabrication of the flow sensor. Complete calibration requires further work and investigation into electronic control circuitry for the flow sensing.

With the initial measurements it was shown that a flow rate of up to 30 µl/min could be measured in the constant current mode. When used in a dosing system, the pump developed by Koch [Koch98b] has an output flow rate of 350 µl/min. This is much larger than the maximum measurable flow rate from the experiments of 30 µl/min. However, measuring higher flow rates has not been investigated and might be possible. The other intended use of the flow sensor is within a micro chemical reaction system, where a mixing chamber is used. The flow rate to achieve perfect mixing within the chamber is 1.7 µl/min [Koch97b]. Thus, the flow sensor can be used for this application.

Achieving integrated microfluidic systems, e.g. chemical microplants, drug delivery systems and particle analysis systems is of great interest because of the possibility of developing automated chemical analysis or (bio)chemical production on the micron scale. A very common method in electronics is the integration of discrete devices on an electrical circuitboard. In order to adapt this technique in microfluidics, a novel microfluidic circuitboard has been successfully developed [Scha99]. It consists of a pyrex wafer in which channels and connection holes have been etched and a silicon backplate to seal the channels. The size of the board varies with the number of devices mounted on top. Channels having a width of 2-3 mm, a length of 3-6 mm and a height of 250 µm have been fabricated. The pressure losses have been calculated to be less than 5 Pa within a channel for a flow rate of 100 µl/min.

The functionality of the fluidic circuitboard has been verified by mounting a diaphragm pump and measuring the pump rate. Another test comprised two pumps, two flow sensors and a mixing chamber mounted onto the board with liquid passing through all the devices [Scha98].

Micromachined reaction chambers based on silicon and pyrex for the thermal cycling of DNA by the polymerase chain reaction have been designed and fabricated [Scha00], thus combining microfluidics with biotechnology. Silicon was used because of its thermal properties and because of the mass-fabrication methods available. The heating and cooling rates possible with silicon cannot be achieved by any glass or plastic device. Fast thermal cycling was required by the initiator of the project, DERA Porton Down, due to the intended application of field-sampling. The size of the chip is 4 mm x 6 mm with a height of 1.5 mm. The reaction chamber volume is 1 µl. With a power input of 3.9 W, heating rates of 44 degC/sec were achieved. Cooling with forced air enabled rates of 33 degC/sec.

Tests showed that for a water filled chip a time of 2.2 min for 30 three-step-temperature cycles was feasible, which makes it the smallest and fastest single shot silicon based PCR device presented to date. Furthermore, the chip enables optical detection through a transparent window.

For enhancing and integrating the PCR chip even further, novel methods to improve the optical detection have been investigated [Scha01b]. One method used two optical fibres, one for light input and the other for detection of fluorescent light. Tests were carried out with 5mM solution of Nile Blue A Perchlorant in water. An input power from a HeNe laser of 4.135 mW yielded an output power from the fluorescent dye of 0.55 nW, which proves that the system functions. The second method used an optical fibre for light input and an intra-cell pn-diode for the detection of light. The chamber photodiode was tested using a multimode fibre connected to an ultra bright blue LED. I-V characteristic curves were obtained and show that the intra-cell photodiode can be used for detection of light in the nW range.

Tests with both systems gave promising results and show that for future PCR systems, bulk optical components like mirrors and lenses can be avoided and that the system can be made immune to the influence of ambient light. This would improve the chip handling enormously as large boxes, containing and protecting heavy bulk optics can be avoided and also measures to protect the chip from ambient light, which can lead to spurious results, would no longer be necessary.

7.2 Suggestions for Further Work

7.2.1 Microfluidic Systems

After developing and enhancing several microfluidc devices and fabricating an interconnection method to combine several devices, systems could be characterised as a next step.

First, the flow sensor could be mounted together with a pump onto the fluidic circuitboard to create a dosing system with the sensor measuring and controlling the pump's output (figure 7.1). The liquid only micropump could be replaced by the new bubble tolerant gas/liquid micropump to make the system easier to fill. Before, the system had to be filled by external pressure giving careful attention not to entrap any gas bubbles. The flow sensor could be calibrated for gases enabling the dosing system to be used for gases and liquids.

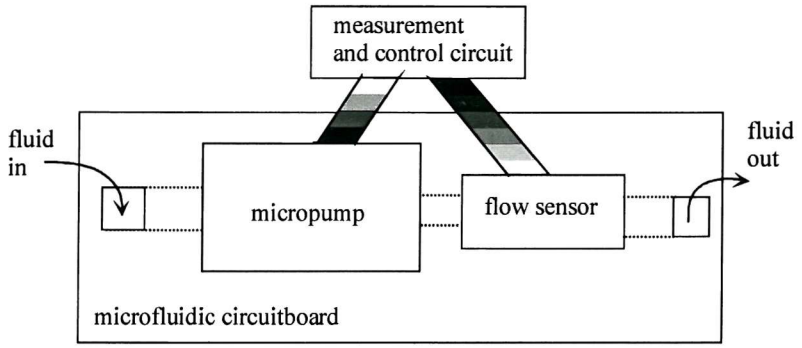

Figure 7.1: Schematic of a dosing system.

Characterising the dosing system would lead to the next step of creating a chemical reaction system. Two dosing systems can be combined with a mixing/reacting device. Several applications for such a system are given in section 5.4.2.

Going 'micro' for oceanographic sampling has clear advantages as strong interest from oceanographic experts in the work presented above shows. The collaboration with the SOC could be extended reaching ocean compatible systems. A specific example of an ammonia detection system is also given in section 5.4.2.

It has been proven that the PCR chip can be heat cycled fast. The next step is to perform a real DNA amplification within the chip using the integrated heaters and the temperature sensor. Also, the optical fibres and the pn-diode implemented into the PCR chip can be tested under 'real' conditions.

With the existing devices and the development of a micromachined lysis chamber [Lee99] a microfluidic system can be created to extract DNA from sample cells, mix them with the primers, enzymes, buffers and probes and amplify them within the PCR chip and detect the reaction product optically. Cell lysing is defined as disrupting cells by physical, chemical, mechanical or enzymatic means in order to obtain intracellular materials, like DNA. An overview of the different lysing methods is given by [Lee99].

A schematic of such a 'DNA evaluation system' is shown in figure 7.2. For this application, the dead volume within the channels connecting the discrete devices needs to be minimised.

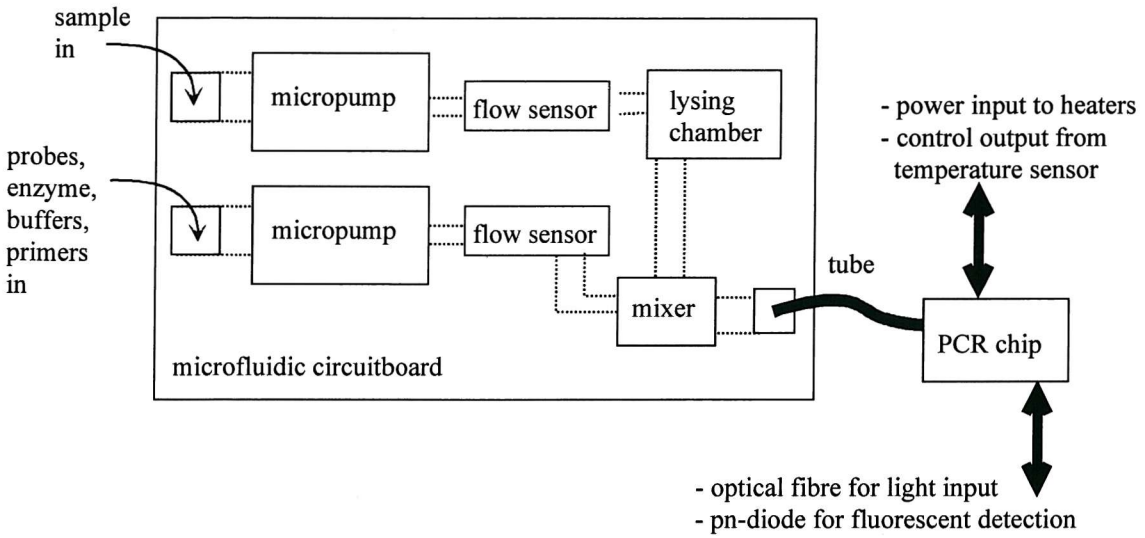

Figure 7.2: Schematic of a microfluidic system for DNA extraction, amplification and detection.

7.2.2 X-ray Microdetector

The photodiode described in chapter 6 can be used as an x-ray micro detector. A collaboration has been established with Delft University of Technology, The Netherlands, and the University of Minho, Portugal, with Dr. Wolffenbuttel as project supervisor.

The principle of the x-ray micro detector is shown in figure 7.3. The cavity is filled with a scintillator material (CsI:Tl). When the scintillator absorbs x-rays, green light with a wavelength of 560 nm is emitted, which is then detected by the photo diode. The photo current has been measured by Gerardo Rocha from the University of Minho over a set of wave lengths as shown in figure 7.4. The diode has a good response above a wavelength of 450 nm, which makes it usable for the proposed application. Currently work is being carried out by the University of Minho on the adhesion of the scintillator to the cavity walls. The next step is to measure the light emitted by the scintillator with the photo diode after x-ray illumination.

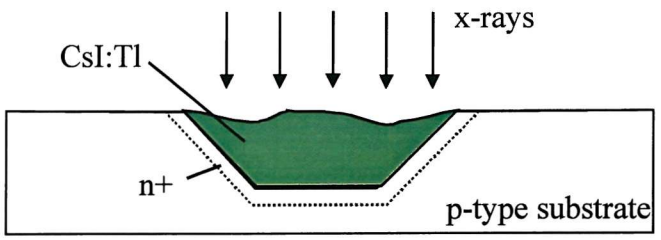

Figure 7.3: Silicon device with a photodiode inside a cavity filled with a scintillator material.

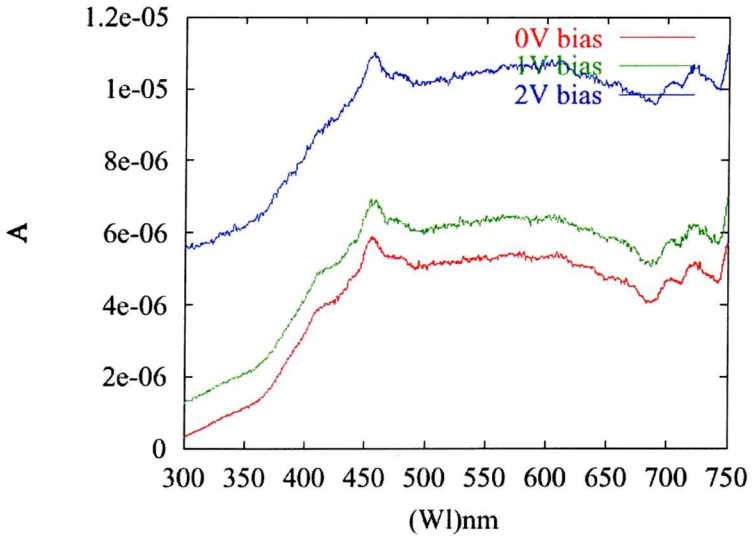

Figure 7.4: Photo current versus wavelength of light.

7.2.3 Valve PCR-chip

A PCR chip with an integrated valve would be very desirable as the reaction chamber could be sealed without the need of a crimping tool. The description of this valve PCR chip is in this further work chapter as the device is not fully characterised. It has been designed and fabricated, however, only preliminary results were obtained in time before finishing this thesis. Investigations about a suitable valve actuation principle were carried out as described in the next section followed by schematics of the process flow and pictures of the finished chip. For further work, the closure of the valve by the electrostatic force between the pyrex and the silicon needs to be studied. It needs to be investigated if the electrostatic force can hold the valve closed despite the pressure generated inside the reaction chamber by heating the liquid (water) up to the 95 degC required for the polymerase chain reaction.

A first test on the valve PCR chips showed that the anodic bonding procedure damaged the insulating oxide between the silicon and the pyrex. As an alternative method, the silicon was bonded to the pyrex with SU-8 epoxy resist by brushing and spinning the resist onto the silicon and long time exposure to polymerase the resist (~ 200 sec) through the transparent pyrex. This has been done on single chips and not on the wafer level.

The reaction chamber was filled by inserting hypodermic needles into trenches sawn into the pyrex similar to the procedure described in section 6.2.3. Essential for the filling with water was the preliminary flushing of the chip with CO_2 for two minutes. CO_2 dissolves in water, thus allowing the water to fill the chamber. According to DERA Porton Down, the CO_2 does not inhibit the PCR reaction.

Four different chip sizes (7.1 x 7.7 mm^2, 9.2 x 9.8 mm^2, 12 x 13 mm^2 and 14 x 15 mm^2) have been fabricated with varying membrane dimensions (5.5 mm, 7.1 mm, 9.4 mm, 11.4 mm) to ensure to obtain a moving valve seat. The valve is closed by applying a voltage between the pyrex and the silicon. Contact to the silicon is made from the back (figure 7.5) and the pyrex is contacted via an electrode deposited onto the pyrex. This electrode is made accessible by cutting or breaking a part of the silicon wafer as indicated in figure 7.7 and 7.9. At the same time the metal electrode used for closing the valve on the pyrex part (figure 7.8) was used to avoid the anodic bonding of the silicon valve seat to the pyrex.

A very similar approach towards a valve has recently been described by Schaible [Scha01c]. An electrostatically activated 2-way valve is realised in silicon. The chip size is 6 mm x 6 mm x 1 mm. A voltage amplifier with input voltage between 3 and 12 Volt is used to gain an output voltage of 200 Volt needed for closing the valve. The distance between the outlet and the valve plate was 5 µm.

7.2.3.1 Valve actuation principles

Investigation has been made into the principles of active valves. Those actuation principles are described in the following:

- thermal: Large forces and movements up to 50 µm can be achieved. The actuation is relatively slow and a large amount of power is necessary. Although this actuation principle is most popular at the moment the undesirable heating of the chip is the biggest drawback for the specific application in micro PCR chips.
  Thermal bimorphs and shape memory alloys have the same advantages and disadvantages.
- microcombustion: Very high forces can be achieved but the temperature will be higher than 300 degC.
- piezoelectric: Very high forces but very small movements (7 µm with a stacked piezo) are the characteristics of this principle. High voltages would be necessary.
- pneumatic: This avoids the local generation of the force but external fluidic connections are necessary.
- electromagnetic: Actuators are difficult to micromachine and an external coil would be required.
- electrostatic: High forces and large movements with reasonable low voltages can be achieved.

Comparing all actuation principles the electrostatic drive of our valve seemed to be the most promising. Therefore further investigations were concentrated on the electrostatic actuation of the valve for the PCR chip. According to DERA Porton Down, the electrostatic force does not inhibit the PCR reaction.

7.2.3.2 Fabrication of the valve PCR-chip

In the following, the process steps for the microfabrication of silicon (figure 7.5), pyrex (figure 7.6) and the bonding of both parts (figure 7.7) are described along with schematic drawings for easier understanding. Photographs of the chip are shown in figure 7.8 and 7.9 indicating the various parts of the chip. SEM photographs show the valve seat of the chip (figure 7.10), the distance between the silicon and the pyrex (figure 7.11) and the thickness of the SU-8 resist (figure 7.12), which is increasing the intended distance for the valve movement from ~5 µm to ~7 µm.

SILICON:

- deposit oxide 600 nm
- deposit nitride 160 nm

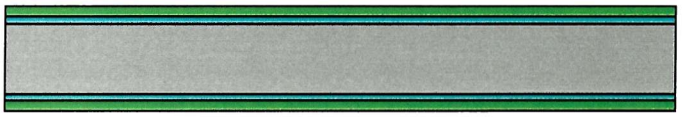

- photolithography
- dry etch nitride and oxide
- strip resist

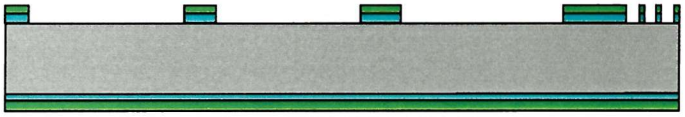

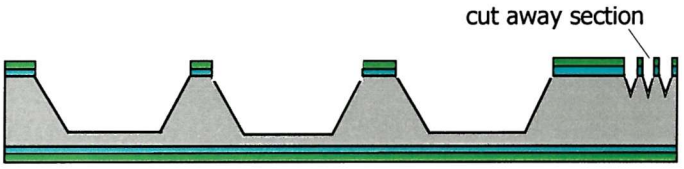

- KOH etch 440 µm deep

- strip nitride and oxide
- deposit oxide 100 nm
- photolithography on back for bulk contact (open oxide)
- evaporate Titanium 20 nm and Platinum 200 nm
- photolithography on back to pattern the resitors and the contact pads by ion-beam milling
- strip resist

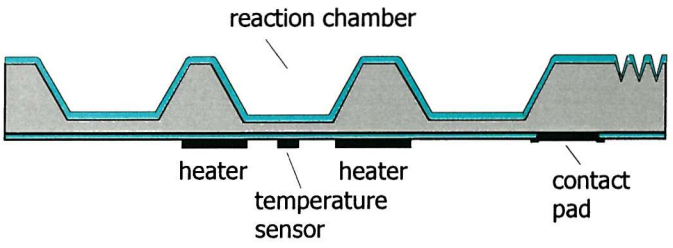

Figure 7.5: Process flow of the valve PCR-chip: silicon part.

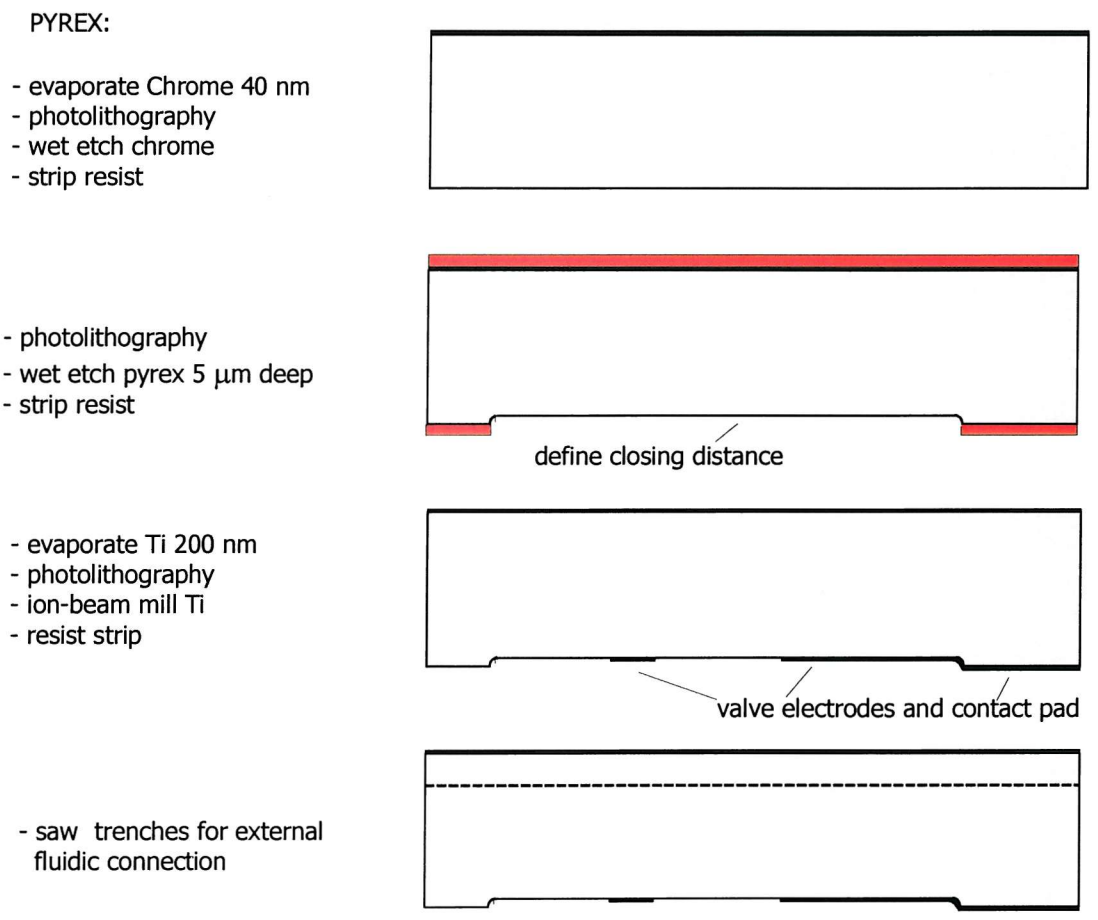

Figure 7.6: Process flow of the valve PCR-chip: pyrex part.

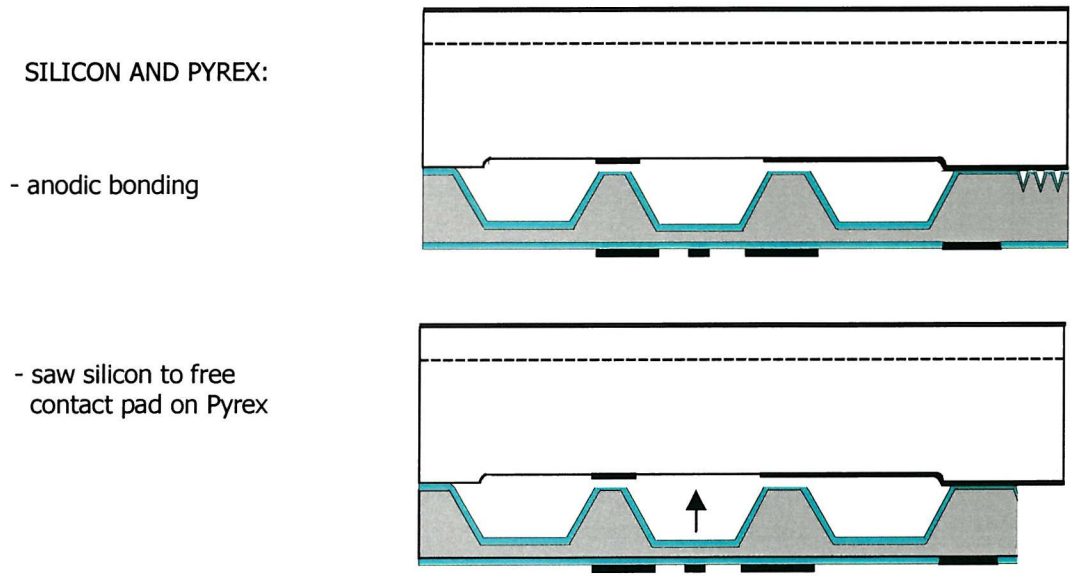

Figure 7.7: Process flow of the valve PCR-chip: bonding.

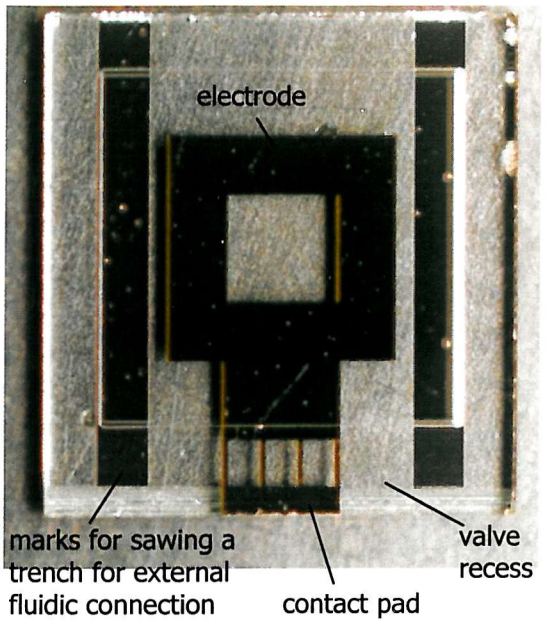

Figure 7.8: Valve PCR-chip: pyrex part – 7.1 mm x 7.7 mm.

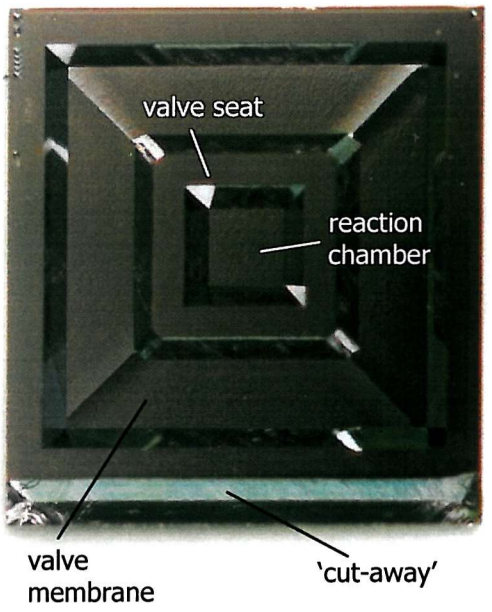

Figure 7.9: Valve PCR-chip: silicon part – 7.1 mm x 7.1 mm.

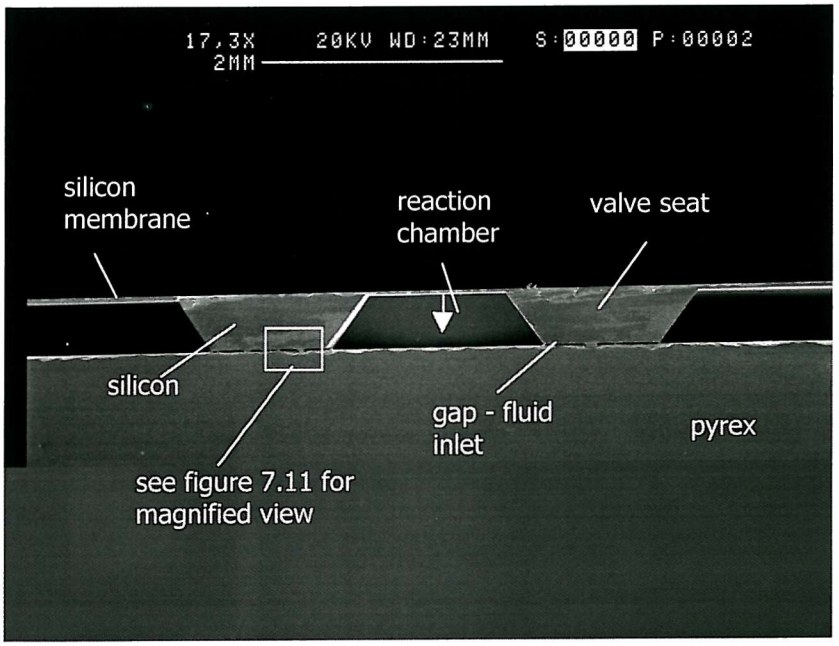

Figure 7.10: SEM of valve PCR-chip.

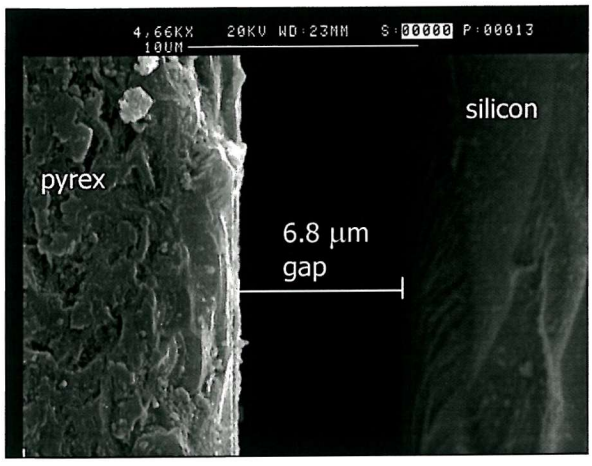

Figure 7.11: Gap for fluidic connection.

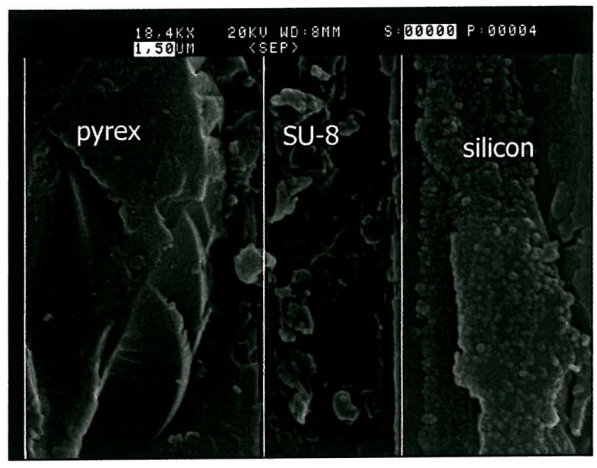

Figure 7.12: SU-8 epoxy resist bonding.

APPENDIX A

Introduction to DNA Amplification using the Polymerase Chain Reaction (PCR)

Two important innovations were responsible for automating PCR. First, a heat-stable DNA polymerase was isolated from the bacterium 'Thermus aquaticus', which inhabits hot springs. This enzyme, called the 'Taq DNA polymerase', remains active despite repeated heating during many cycles of amplification. Second, DNA thermal cyclers have been designed in which a computer controls the repetitive temperature changes required for PCR.

To perform a PCR reaction, a small quantity of target DNA is added to a buffered solution containing Taq DNA polymerase, short oligonucleotide primers, the four deoxynucleotide building blocks of DNA and the cofactor $MgCl_2$. Primers are artificially made sequences of single stranded DNA (ssDNA) of usually 20 to 30 nucleotides. The primers are engineered to fit to complementary sequences on the target DNA strand. The deoxynucleotide building blocks are Cytosine (C), Guanine (G), Adenine (A) and Thymine (T), whereupon C binds to G and A binds to T. They are termed base-pairs. The buffers, including the cofactor $MgCl_2$, are to maintain the right ion concentration and ph level during the reaction. The PCR mixture is then taken through replication cycles.

Figure A.1 depicts the principle of DNA multiplication and figure A.2 shows the temperature progression during one replication cycle. The sample is heated to 94-96 degC to denature the target DNA (separate into single strands). The temperature is then lowered to 50-65 degC permitting the primers to anneal to their complementary sequences. The temperature is now raised to 72 degC, allowing the *Taq DNA polymerase* to attach at each priming site (where primers have annealed) and extend (synthesize) a new DNA strand. As amplification proceeds, the DNA sequence between the primers doubles after each cycle. Following thirty such cycles, a theoretical amplification factor of one billion is attained.

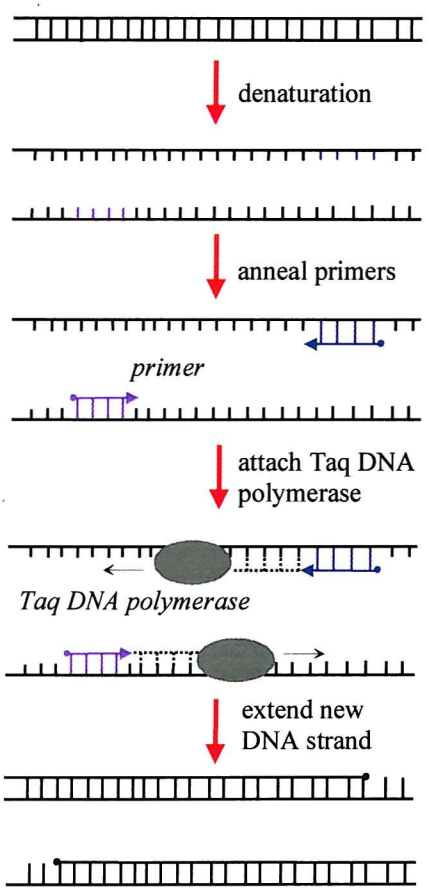

Figure A.1: Principle of DNA amplification using the polymerase chain reaction.

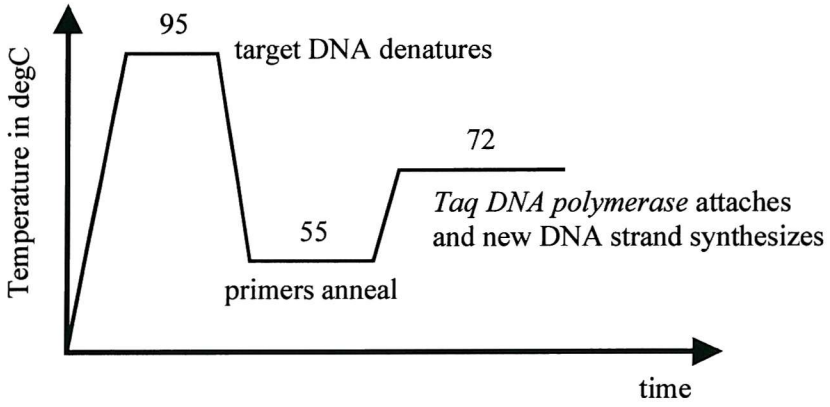

Figure A.2: Temperature progression during one replication cycle.

APPENDIX B

Optical Detection for Real-Time Quantitative PCR

The background of homogeneous reporting chemistries for the polymerase chain reaction (PCR) is discussed. Homogeneous chemistry implies that all necessary parts for the amplification and detection are within the reaction mixture. These chemistries use fluorescence detection and fluorimeters are used for detection. Fluorimeters are relatively simple optical arrangements that collect signal from the whole sample rather than at a specialised surface. The only requirement is that an optical window is available into the PCR chamber to allow the passage of visible light in and out of the reaction mixture. The ability to detect extremely low numbers of nucleic acid species using these approaches is derived from the performance of the PCR. These assays also provide a kinetic closed tube approach to quantification that covers the whole range of PCR amplification. Kinetic approach means that the detection takes place during the amplification cycles and not, as in end point analysis techniques such as gel electrophoresis, after the completed amplification process. Therefore, optical detection allows both, qualitative and quantitative assay of the PCR product.

Homogeneous fluorescent assays are modifications to current PCR chemistries that showed several improvements in the automation and analysis of PCR such as real-time monitoring and observing, for the first time possible, the kinetics of the reaction. These modifications involve the addition of a fluorescent reaction reagent(s) to the assay. The reagents can be broadly grouped into two types.

The first type of reagent is one that simply reports the generation of nucleic acid amplification in the reaction. The reagents are intercalating dyes and the type of monitoring the reaction is termed *non-strand specific detection*. The second reagent types are nucleic acid probes that are specific for the non-primer sequence of the amplicon. The sequence of a nucleic acid that a PCR is designed to amplify is termed *amplicon*. The reagents interact with the amplicon at the sequence level, generating a signal that is highly specific for the desired PCR amplification product. The term for this type of monitoring the reaction is called *strand specific detection*.

The non-strand specific and strand specific assay formats will now be discussed in more detail and a summary of both probe systems is given in Table B.1. This table includes schematic diagrams that show the mechanism of detection.

B.1 DNA intercalators, non-strand specific detection

Fluorescent DNA intercalators include dyes that bind to double stranded DNA (dsDNA) with enhanced fluorescence [Higu92, Higu93, Ishi95, Witt97, Rasm98, Morr98]. These include dyes such as ethidium bromide [Higu93] that is used routinely for DNA electrophoresis gels. Other dyes such as the YO-PRO® dyes, YoYo® dyes [Ogur94] and the SYBR® dyes can be used effectively in PCR because they exhibit significantly more fluorescence when bound to dsDNA than to single stranded DNA (ssDNA). This effect is poorly understood until now. It has been proposed that the dye molecule when tightly bound within the double stranded DNA helix is fluorescent because non-radiative decay of the excited state via proton transfer to the water molecules is not possible. Molecular probe's SYBR® dyes, particularly SYBR®Green-1 and SYBR®Gold, are now used routinely because their fluorescent emission spectrum closely matches that of fluorescein. This is convenient as fluorimeter designs are often optimised for fluorescein. These dyes are simply added as a reagent to the PCR cocktail of standard reactions (table B.1).

DNA melting point analysis is a methodology that can be applied to this assay type and may be used at the end of PCR to characterise amplification products [Riri97]. This allows DNA intercalators to be used to generate quasi-strand specific data on amplification products. As the dsDNA duplex melts apart DNA becomes ssDNA and the intercalator dye fluorescence drops. Different PCR products (amplified dsDNA) and artefacts (unwanted by-products such as forward and backward primer bound together) melt at different temperatures. Their melting points are dependent upon a number of factors including their GC basepair content and length. However, the discriminatory power of this is limited because melting point analysis does not have the resolution of a separation analysis such as agarose or capillary gel electrophoresis (agarose: melted sea-weed extract).

B.2 Strand specific analysis

Strand specific analysis requires the design and synthesis of a bespoke fluorescent nucleic acid probe(s) for each PCR assay. This probe(s) interacts with the product reporting an increase after each cycle on amplification. Probes may also be used in melting point experimentation to provide additional identification of the amplified product as it is discussed in B.1.

This type of reporting system utilises Fluorescent Resonance Energy Transfer (FRET) [Selv95] between two fluorescent dyes as the basis of detection. One dye, the donor, is excited with an incidence light source that has a defined spectrum. When excited, the donor emits light at longer fluorescent emission wavelengths. When a second dye, the acceptor, is in close

proximity, it will accept the emission light of the donor provided that the wavelength of light falls within the range of the acceptors excitation spectrum. This interaction is often termed fluorescent quenching. A schematic can be seen in figure B.1. The FRET efficiency is spatially constrained. When the donor is separated from the acceptor during the PCR, the light emitted by the donor can be detected instead of the acceptor's light.

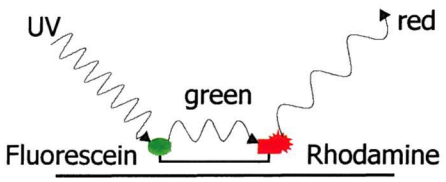

Figure B.1: Schematic of the FRET-effect using a TaqMan® probe. In this case, fluorescein and rhodamine are used as donor and acceptor, respectively.

The types of dyes used for these probes include fluorescein, rhodamine, and cyanine dyes. The chemistries for label incorporation into nucleic acid probes is well developed since they are used in other molecular biology procedures such as DNA sequencing. Other non-fluorescent dyes such as DABCYL® and methyl-red, often termed 'dark quenchers' are also used frequently as the acceptor dye. These emit light energy in the infrared region of the electromagnetic spectrum and are therefore not true fluorescent dyes.

The strand-specific probes fall into two categories based on how they report amplification. The first category is the hydrolysis probes. These are probes designed to be consumed during the course of the reaction, separating the donor dye from acceptor. The second type are hybridisation probes. These either separate or bring together the acceptor and donor dyes by hybridisation events.

B.2.1 Hydrolysis Probes

The most common hydrolysis probe is an oligonucleotide (sequence of ssDNA) labelled terminally with a donor and acceptor dye at the 5′ and 3′ end [Gelm97, Holl92, Lee93, Youn96]. The 3′ end is protected with a phosphate group so that it will not act as an amplimer in the PCR. The probe sequence is designed such that it hybridises upstream on an amplimer and is concomitantly hydrolysed by the 5′-3′ exonuclease activity of the polymerase during Palmer extension each cycle. The previously quenched acceptor is separated from donor as the basis of detection. Each cycle the signal accumulates. These types of probes are known commercially as TaqMan™ probes (table B.1).

B.2.2 Hybridisation Probes

There are several types of hybridisation probes. They differ in the hybridisation mechanism that they use to report amplification. The main difference between hybridisation probes and hydrolysis probes is in their design. These types of probes are designed not to be consumed

during the reaction. Each cycle probe must hybridise to products to report the increase in amplification. An outline of known types will now be given.

Dual-hybe probes are pairs of fluorescent-labelled oligonucleotide probes that hybridise to the internal sequence of an amplification product [Card88, Witt97]. One probe is labelled terminally at the 3′ end with either a donor or acceptor dye. The other probe is labelled terminally at the 5′ end with either a donor or acceptor dye. The probes are designed such that they hybridise adjacently on a complementary strand bringing the 3′ of the first probe spatially close to the 5′ of the second, thus allowing efficient fluorescent quenching by FRET as the basis of detection (table B.1).

Molecular beacons are oligonucleotide probes that have looped hairpin structures [Tyag96]. This is achieved by the addition of extra complementary sequences at the 5′ and 3′ termini that is not complimentary to the sequence to be detected. The molecular beacon has donor and acceptor dyes at the 5′ and 3′ ends. In the absence of target these terminal sequences hybridise bringing donor and acceptor together, and thus, efficient fluorescent quenching. When the probe binds to the specific target the energetics favour a linear duplex structure such that the donor is separated from acceptor, reducing FRET, as the basis of detection (table B.1).

Sunrise® or Amplifluor® is a probe system that uses a molecular beacon attached to the 5′ end of an amplimer [Naza97]. This molecular beacon has no specificity for the target PCR product and a generic molecular beacon may be used for all reactions. During the amplification the complement sequence of the molecular beacon is generated such that when product and probe anneal the beacon structure is no longer formed. The donor is separated from the quencher (acceptor) as the basis of detection (table B.1). Since the probe has no specificity for the reaction this is not a true strand specific approach.

Scorpions® is also an oligonucleotide probe system that has a molecular beacon joined to the 5′ end of an amplimer. However, the probe has a linker between the amplimer and the molecular beacon that stops the enzyme from reading, and thus generating the molecular beacon compliment [Whit99]. This molecular beacon does have specificity for the strand that is generated by the amplimer it is attached to. During the cooling of the PCR (after the extended dsDNA has been denatured), when the energetics are favourable, the molecular beacon structure destabilises and anneals to the complementary strand. This hybridisation event separates the acceptor from the quencher (donor) with a resulting reduction in FRET as the basis of detection (table B.1).

Assay	Specificity	Mechanism	Schematic of reporting mechanism
SYBR® Dyes	Non-strand Specific	Intercalator	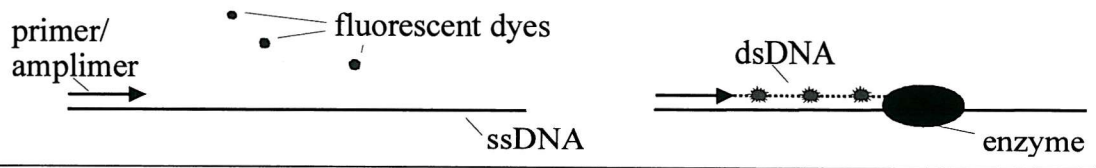
TaqMan®	Strand Specific	Hydrolysis/ FRET	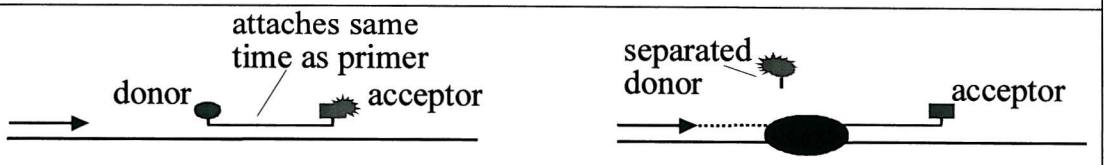
Dual Hybe Probes	Strand Specific	Hybridisation/ FRET	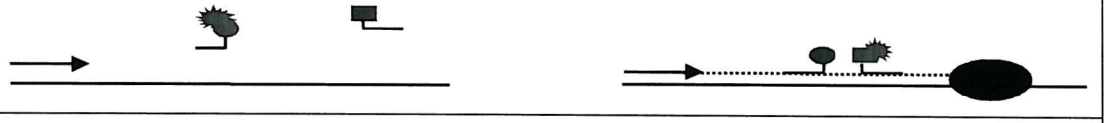
Molecular Beacons	Strand Specific	Hybridisation/ FRET	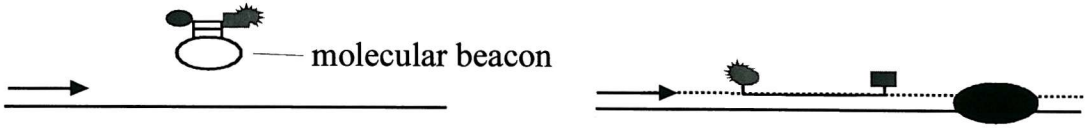
Sunrise®/ Amplifluor®	Non-strand Specific	PCR only/FRET	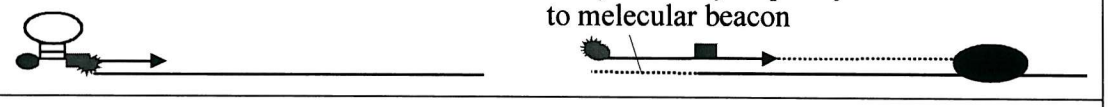
Scorpions®	Strand Specific	Hybridisation/ FRET	

Table B.1: Summary of the current approaches for homogeneous fluorescent PCR detection showing the reporting mechanism of each probe system.

APPENDIX C

List of Publications and Presentations

C.1 Journal Publications

[1] C. G. J. Schabmueller, M. Koch, A. G. R. Evans, A. Brunnschweiler, "Design and Fabrication of a Microfluidic Circuitboard", Journal of Micromechanics and Microengeneering, Vol. 9, No. 2, pp. 176-179, 1999.

[2] M. Koch, C. G. J. Schabmueller, A. G. R. Evans, A. Brunnschweiler, "Micromachined Chemical Reaction System", Sensors and Actuators A, Vol. 74, pp. 207-210, 1999.

[3] C. G. J. Schabmueller, A. G. R. Evans, A. Brunnschweiler, G. J. Ensell, D. L. Leslie, M. A. Lee, "Packaging of closed chamber PCR-chips for DNA amplification", Microelectronics International, Vol. 17, No. 2, pp. 11–14, 2000.

[4] C. G. J. Schabmueller, A. G. R. Evans, A. Brunnschweiler, G. J. Ensell, D. L. Leslie, M. A. Lee, "Closed Chamber PCR-Chips for DNA Amplification", Engineering Science and Education Journal, IEE, Vol. 9, No. 6, pp. 259-264, 2000.

[5] C. G. J. Schabmueller, J. R. Pollard, A. G. R. Evans, J. S. Wilkinson, G. Ensell, A. Brunnschweiler, "Integrated Diode Detector and Optical Fibres for In-Situ Detection within Micromachined Polymerase Chain Reaction Chips", Journal of Micromechanics and Microengeneering, Vol. 11, No. 4, pp. 329-333, 2001.

C.2 Keynote Papers

[1] C. G. J. Schabmueller, M. Koch, A. G. R. Evans, A. Brunnschweiler, "Micromachined chemical reaction system realized on a microfluidic circuitboard", Eurosensors XII, Vol. 1, Institute of Physic Publishing, Bristol, UK, pp. 571-574, 1998. Presented at Eurosensors XII (1998), Southampton, United Kingdom, 1998.

C.3 Conference Publications

[1] C. G. J. Schabmueller, M. Koch, A. G. R. Evans, A. Brunnschweiler, "Design and Fabrication of a Microfluidic Circuitboard", Proceedings of Micromechanics Europe '98 (MME), Ulvik, Norway, pp. 218-221, 1998.

[2] M. Koch, C. G. J. Schabmueller, A. G. R. Evans, A. Brunnschweiler, "Micromachined Chemical Reaction System", Book of Abstracts of European Materials Research Society '98 (E-MRS), Strasbourg, France, Symposium H-3, 1998.

[3] M. Koch, C. Schabmueller, A. G. R. Evans, A. Brunnschweiler, "A Micromachined Particle Sorter: Principle and Technology", Eurosensors XII, Vol. 1, Institute of Physics Publishing, Bristol, UK, pp. 595-598, 1998. Presented at Eurosensors XII (1998), Southampton, United Kingdom, 1998.

[4] C. G. J. Schabmueller, A. G. R. Evans, A. Brunnschweiler, G. J. Ensell, D. L. Leslie, M. A. Lee, "Packaging of closed chamber PCR-chips for DNA amplification", Proceedings of IMAPS-UK European Microsystems Packaging Conference, London, UK, 2000.

[5] C. G. J. Schabmueller, A. G. R. Evans, A. Brunnschweiler, G. J. Ensell, D. L. Leslie, M. A. Lee, "Design, Fabrication and Packaging of Closed Chamber PCR-Chips for DNA Amplification", Proceedings of Design, Test, Integration, and Packaging of MEMS/MOEMS (DTIP), Paris, France, SPIE Proceedings Series Volume 4019, pp. 362-369, 2000.

[6] C. G. J. Schabmueller, M. Koch, A. G. R. Evans, A. Brunnschweiler, M. Kraft, "Design and Fabrication of a Self-Aligning Gas/Liquid Micropump", Proceedings of SPIE Micromachining and Microfabrication, Microfluidic Devices and Systems III Conference, Santa Clara, USA, SPIE Proceedings Series Volume 4177, pp. 282-290, 2000.

[7] C. G. J. Schabmueller, J. R. Pollard, A. G. R. Evans, J. S. Wilkinson, G. Ensell, A. Brunnschweiler, "Integrated Diode Detector and Optical Fibres for In-Situ Detection of DNA Amplification within Micromachined PCR Chips", Proceedings of Micromechanics Europe (MME) 2000, Uppsala, Sweden, pp. A12, 2000.

[8] C. G. J. Schabmueller, M. Koch, M. E. Mokhtari, A. G. R. Evans, Brunnschweiler, H. Sehr, "Mass-Producible, Bubble Tolerant Gas/Liquid Micropump with Self-Aligning Feature", Proceedings of Micromechanics Europe (MME) 2001, Cork, Ireland, pp. 183-186, 2001.

[9] M. Paine, C. G. J. Schabmueller, A. G. R. Evans, S. Gabriel, "Design and Fabrication of Microthrusters for Space Application", Proceedings of Micromechanics Europe (MME) 2001, Cork, Ireland, pp. 179-182, 2001.

[10] H. Sehr, I. S. Tomlin, S. P. Beeby, A. G. R. Evans, A. Brunnschweiler, G. J. Ensell, C. G. J. Schabmueller, T. E. G. Niblock, "Dynamic Characterisation of Thermal Vertical Bimorph Actuators", Proceedings of Micromechanics Europe (MME) 2001, Cork, Ireland, pp. 159-162, 2001.

[11] C. G. J. Schabmueller, M. A. Lee, A. G. R. Evans, J. S. Wilkinson, G. J. Ensell, D. L. Leslie and A. Brunnschweiler, "Silicon micromachined PCR-chips with integrated fibre optic light coupling and in-situ pn-diode for fluorescent detection", Proceedings of Homogeneous Fluorescent Reporting Systems for Real-Time Quantitative PCR Conference, Winchester, United Kingdom, 2001.

C.4 Presentations

[1] C. G. J. Schabmueller, A. G. R. Evans, A. Brunnschweiler, G. J. Ensell, D. L. Leslie, M. A. Lee, "Closed Chamber PCR-Chips for DNA Amplification", Seminar Proceedings of Demonstrated Micromachining Techniques for Industry, IEE Seminar, Birmingham, UK, pp. 4/1-4/5, 2000.

REFERENCES

[Abra99] S. Abramowitz, 'DNA Analysis in Microfabricated Formats', Journal of Biomedical Microdevices, Vol. 1, No. 2, pp. 107-112, 1999.

[Akah00] K. Akahori, S. Kondo, E. Shinohara, K. Tashiro, S. Shoji, 'Multi Micro Reactors Consits of Individually Temperature Controlled Silicon Well Arrays Realizing Efficient Biochemical Reactions', Proceedings Micro Total Analysis Systems (μTAS), Enschede, The Netherlands, pp. 493-496, 2000.

[Baba99] Y. Baba, 'DNA Analysis and Diagnostics with Integrated Micro Sensors', Proceedings Transducers, Sendai, Japan, pp. 1B3.1, 1999.

[Bada00] M. Y. Badal, T. T. Tang, W. E. Lee, T. Dickinson-Lang, D. E. Bader, D. J. Harrison, 'An Integrated System for Gene Detection Using Cycling Probe Technology', Proceedings Micro Total Analysis Systems (μTAS), Enschede, The Netherlands, pp. 423-426, 2000.

[Bark00] S. L. R. Barker, M. J. Tarlov, M. Branham, J. Xu, W. MacCrehan, M. Gaitan, L. E. Locascio, 'Derivatization of Plastic Microfluidic Devices with Polyelectrolyte Multilayers', Proceedings Micro Total Analysis Systems (μTAS), Enschede, The Netherlands, pp. 67-70, 2000.

[Bart00] M. Bartek, Z. Xiao, C. van Mullem, R. F. Wolffenbuttel, 'Bulk-micromachined electrostatic RMS-to-DC converter: Design and fabrication', Proceedings Micromechanics Europe, Uppsala, Sweden, pp. A14, 2000.

[Bart90] S. F. Bart, L. S. Tavrov, M. Mehregany, J. H. Lang, 'Microfabricated electrohydrodynamic pumps', Sensors and Actuators, Vol. A21-23, pp. 193-197, 1990.

[Bass77] E. Bassous, H. H. Taub, L. Kuhn 'Ink jet printing nozzle arrays etched in silicon', Applied Physics Letters, Vol. 31, pp. 135-137, 1977.

[Beeb00] D. J. Beebe, J. S. Moore, Q. Yu, R. H. Liu, M. L. Kraft, B.-H. Jo, C. Devadoss, 'Microfluidic tectonics: A comprehensive construction platform for microfluidic systems', Nature Medicine, Vol. 97, No. 25, pp. 13488-13493, 2000.

[Bena97] W. L. Benard, H. Kahn, A. H. Heuer, M. A. Huff, 'A Titanium-Nickel shape memory alloy actuated micropump', Proceedings Transducers, Chicago, USA, pp. 361-364, 1997.

[Blac99] J. P. Black, R. M. White, 'Microfluidic Applications of Ultrasonic Flexural Plate Waves', Proceedings Transducers, Sendai, Japan, pp. 4C1.4, 1999.

[Boeh00] S. Boehm, B. Timmer, W. Olthuis, P. Bergveld, 'A closed-loop controlled electrochemically actuated micro-dosing system', Journal of Micromechanics and Microengineering, No. 10, pp. 498-504, 2000.

[Boeh99a] S. Boehm, W. Olthuis, P. Bergveld, 'An Electrochemically Actuated Micropump for use in a 'Push-Pull' Microdialysis Based In-Vitro Monitoring System', Proceedings Transducers, Sendai, Japan, pp. 3B1.3, 1999.

[Boeh99b] S. Boehm, W. Olthuis, P. Bergveld, 'A plastic micropump constructed with conventional techniques and materials', Sensors and Actuators, Vol. A77, pp. 223-228, 1999.

[Boon00] T. D. Boone, A. J. Ricco, P. Gooding, T. O. Bjoernson, S. Singh, V. Xiao, I. Gibbons, S. J. Williams, H. Tan, 'Sub-Microliter Assays and DNA Analysis on Plastic Microfluidics', Proceedings Micro Total Analysis Systems (μTAS), Enschede, The Netherlands, pp. 541-544, 2000.

[Bosc93] D. Bosch, B. Heimhofer, G. Mueck, H. Seidel, U. Thumser, W. Welser, 'A silicon microvalve with combined electromagnetic/electrostatic actuation', Sensors and Actuators, Vol. A37-38, pp. 684 – 692, 1993.

[Bous97] L. Bousse, A. Kopf-Sill, J. W. Parce, 'An Electrophoretic Serial to Parallel Converter', Proceedings Transducers, Chicago, USA, pp. 499-502, 1997.

[Buet94] S. Buettgenbach, 'Mikromechanik', Teubner Studienbuecher, Stuttgart, Germany, 1994.

[Buri98] E. Burian, D. Pogany, T. Lalinsky, N. Seliger, E. Gornik, 'Thermal simulation and characterisation of GaAs micromachined power-sensor microsystems', Sensors and Actuators, Vol. A68, pp. 372-377, 1998.

[Card88] R. A. Cardullo, S. Agrawal, C. Flores,P. C. Zamecnik, D. E. Wolf, 'Detection of nucleic acid hybridisation by nonradiative fluorescence resonance energy transfer', Proceedings National Academy of Science USA, Vol. 85, pp. 8790-8794, 1988.

[Cho91] S. T. Cho, K. D. Wise, 'A High-Performance Microflowmeter with Built-In Self Test', Proceedings Transducers, San Francisco, USA, pp. 400-403, 1991.

[Claa85] W. A. P. Claassen, W. G. J. N. Valkenburg, M. F. C. Willemsen, W. M. v. d. Wijgert, 'Influence of Deposition Temperature, Gas Pressure, Gas Phase Composition, and RF Frequency on Composition and Mechanical Stress of Plasma Silicon Nitride Layers', Journal of the Electrochemical Society: Solid-State Science and Technology, Vol. 132, No. 4, pp. 893-898, 1985.

[Corm97] T. Corman, P. Enoksson, G. Stemme, 'Deep Wet Etching of Borosilicate Glass using an Anodically Bonded Silicon Substrate as Mask', Proceedings Micromechaniks Europe, Southampton, England, pp. 55-58, 1997.

[Dani98] J. H. Daniel, S. Iqbal, R. B. Millington, D. F. Moore, C. R. Lowe, D. L. Lelsie, M. A. Lee, M. J. Pearce, 'Silicon microchambers for DNA amplification', Sensors and Actuators, Vol. A71, pp. 81-88, 1998.

[Dari00] P. Dario, M. C. Carrozza, A. Benvenuto, A. Menciassi, 'Micro-systems in biomedical applications', Journal of Micromechanics and Microengineering, Vol. 10, No. 2, pp. 235-244, 2000.

[Dewa97] A. S. Dewa, K. Deng, D. C. Ritter, C. Bonham, 'Development of LIGA-fabricated self-priming in-line gear pumps', Proceedings Transducers, Chicago, USA, pp. 757-760, 1997.

[Doep97] J. Doepper, M. Clemens, W. Ehrfeld, S. Jung, K.-P. Kaemper, H. Lehr, 'Micro gear pumps for dosing of viscous fluids', Journal of Micromechanics and Microengineering, No. 7, pp. 230-232, 1997.

[Ecke00] A. Eckersten et. al., 'High-Throughput SNP Scoring in a Disposable Microfabricated CD Device', Proceedings Micro Total Analysis Systems (μTAS), Enschede, The Netherlands, pp. 521-524, 2000.

[Ekst00] G. Ekstrand, C. Holmquist, A. E. Oerlefors, B. Hellman, A. Larsson, P. Andersson, 'Microfluidics in a Rotating CD', Proceedings Micro Total Analysis Systems (μTAS), Enschede, The Netherlands, pp. 311-314, 2000.

[Elwe94] M. Elwenspoek, T. S. J. Lammerink, R. Miyake, J. H. J. Fluitman, 'Towards integrated microliquid handling systems', Journal of Micromechanics and Microengineering, Vol. 4, No. 4, pp. 227-245, 1994.

[Elwe98] M. Elwenspoek, H. V. Jansen, 'Silicon Micromachining', Cambridge University Press, Cambridge, England, 1998.

[Erli89] H. A. Erlich editor, 'PCR technology: principles and applications for DNA amplification', Stockton Press, 1989.

[Esas89] M. Esashi, S. Shoji, A. Nakano, 'Normally closed microvalve and micropump fabricated on al silicon wafer', Sensors and Actuators, Vol. 20, No. 1-2, pp. 163 – 169, 1989.

[Flui94] J. H. Fluitman, A. van den Berg, T. S. Lammerink, 'Micromechanical components for μTAS', Proceedings Micro Total Analysis Systems, Twente, The Netherlands, pp. 73-83, 1994.

[Gard96] J. G. E. Gardeniers, H. A. C. Tilmans, C. C. G. Visser, 'LPCVD silicon-rich silicon nitride films for applications in micromechanics, studied with statistical experimental design', Journal of Vacuum Science Technology A, Vol. 14, No. 5, pp. 2879-2892, 1996.

[Gass93a] V. Gass, B. H. van der Schoot, N. F. de Rooij, 'Nanofluid handling by microflow sensor based on drag force measurement', Proceedings IEEE Micro Electro Mechanical Systems, Fort Lauderdale (FL), USA, pp. 167-172, 1993.

[Gass93b] V. Gass, B. H. van der Schoot, S. Jeanneret, N. F. De Rooij, 'Integrated Flow-Regulated Silicon Micropump', Proceedings Transducers, Yokohama, Japan, pp. 1048-1051, 1993.

[Gelm97] S. Gelmini, C. Orlando, R. Sestini, G. Vona, P. Pinzani, L. Ruocco, M. Pazzagli, 'Quantitative polymerase chain reaction-based homogeneous assay with fluorogenic probes to measure c-erbB-2 oncogene amplification', Clinical Chemistry, Vol. 43, No. 5, pp. 752-758, 1997.

[Gerl97] T. Gerlach, 'Pumping Gases by a Silicon Micro Pump with Dynamic Passive Valves', Proceedings Transducers, Chicago, USA, pp. 357-360, 1997.

[Gong99] Q. Gong, Z. Zhou, 'Design, Optimization and Simulation of Micro Electromagnetic Pump', Proceedings Transducers, Sendai, Japan, pp. 2P1.13, 1999.

[Gonz98a] C. Gonzalez, S. D. Collins, R. L. Smith, 'Fluidic interconnects for modular assembly of chemical microsystems', Sensors and Actuators, Vol. B49, pp. 40-45, 1998.

[Gonz98b] C. Gonzalez, R. L. Smith, D. G. Howitt, S. D. Collins, 'MicroJoinery: concept, definition, and application to microsystem development', Sensors and Actuators, Vol. A66, pp. 315-332, 1998.

[Grav93] P. Gravesen, J. Branebjerg, O. S. Jensen, 'Microfluidics – a review', Journal of Micromechanics and Microengineering, Vol. 3, No. 4, pp. 168-182, 1993.

[Gray99] B. L. Gray, D. Jaeggi, N. J. Mourlas, B. P. van Drieenhuizen, K. R. Williams, N. I. Maluf, G. T. A. Kovacs, 'Novel interconnection technologies for integrated microfluidic systems', Sensors and Actuators, Vol. A77, pp. 57-65, 1999.

[Gros99] C. Grosjean, Y.-C. Tai, 'A Thermopneumatic Peristaltic Micropump', Proceedings Transducers, Sendai, Japan, pp. 3P5.10, 1999.

[Guen99] O. T. Guenat, D. Ghiglione, V. Pasquier, B. H. van der Schoot, W. E. Morf, N. F. de Rooij, 'An electro-osmotically driven nanopump for volumetric nanotitration applications', Proceedings Eurosensors XIII, The Hague, The Netherlands, pp. 681-682, 1999.

[Harr00] D. J. Harrison, C. Wang, P. Thibeault, F. Ouchen, S. B. Cheng, 'The Decade's Search for the Killer Ap in μ-TAS', Proceedings Micro Total Analysis Systems (μTAS), Enschede, The Netherlands, pp. 195-204, 2000.

[Harr99] D. J. Harrison, C. Skinner, S. B. Cheng, G. Ocvirk, S. Attiya, N. Bings, C. Wang, J. Li, P. Thibault, W. Lee, 'From Micro-Motors to Micro-Fluidics: The Blossoming of Micromachining Technologies in Chemistry, Biochemistry and Biology', Proceedings Transducers, Sendai, Japan, pp. 1A2.2, 1999.

[Hedi00] S. Hediger, A. Sayah, W. Hunziker, M. A. M. Gijs, 'Biosystem for the culture and characterisation of epithelial cell tissues', Proceedings Micro Total Analysis Systems (μTAS), Enschede, The Netherlands, pp. 99-102, 2000.

[Higu92] R. Higuchi, G. Dollinger, P. S. Walsh, R. Griffith, 'Simultaneous amplification and detection of specific DNA sequences', Bio/Technology, Vol. 10, pp. 413-417, 1992.

[Higu93] R. Higuchi, C. Fockler, G. Dollinger, R. Watson, 'Kinetic PCR analysis: real-time monitoring of DNA amplification reactions', Bio/Technology, Vol. 11, pp. 1026-1030, 1993.

[Holl92] P. M. Holland, R. D. Abramson, R. Watson, S. Will, R. K. Saiki, D. H. Gelfand, 'Detection of specific polymerase chain reaction product by utilising the 5'→3' exonuclease activity of Thermus aquaticus DNA polymerase', Clinical Chemistry, Vol. 38, No. 3, pp. 462-463, 1992.

[Holm99] R. M. Holmes, A. Aminot, R. Kerouel, B. A. Hooker, B. J. Peterson, 'A simple and precise method for measuring ammonium in marine and freshwater ecosystems', Canadian Journal of Fisheries and Aquatic Science, Vol. 56, No. 10, pp. 1801-1808, 1999.

[Ishi95] T. Ishiguro, J. Saitoh, H. Yawata, H. Yamagishi, S. Iwasaki, Y. Mitoma, 'Homogeneous quantitative assay of Hepatitis C virus RNA by polymerase chain reaction in the presence of a fluorescent intercalater', Analytical Biochemistry, Vol. 229, pp. 207-213, 1995.

[Ito95] N. Ito, 'A rapid and selective anodic bonding method', Proceedings Transducers, Stockholm, Sweden, pp. 277-280, 1995.

[Jaco94] S. C. Jacobsen, R. Hergenroeder, L. B. Koutny, J. M. Ramsey, 'Open channel electrochromatography on a microchip', Analytical Chemistry, Vol. 66, No. 14, pp. 2369-2373, 1994.

[Kaem98] K.-P. Kaemper, J. Doepper, W. Ehrfeld, S. Oberbeck, 'A Self-Filling Low-Cost Membrane Micropump', Proceedings Micro Electro Mechanical Systems (MEMS), Heidelberg, Germany, pp. 432-437, 1998.

[Kell00] G. J. Kellogg, T. E. Arnold, B. L. Carvalho, D. C. Duffy, N. F. Sheppard jr, 'Centrifugal Microfluidics: Applications', Proceedings Micro Total Analysis Systems (μTAS), Enschede, The Netherlands, pp. 239-242, 2000.

[Koch00] M. Koch, A. Evans, A. Brunnschweiler, 'Microfluidic Technology and Applications', Research Studies Press Ltd., Baldock, England, 2000.

[Koch97a] M. Koch, N. Harris, R. Maas, A. G. R. Evans, N. M. White, A. Brunnschweiler, 'A novel micropump design with thick-film piezoelectric actuation', Measurements Science and Technology, Vol. 8, pp. 49 – 57, 1997.

[Koch97b] M. Koch, 'Silicon Micromachined Pumps Employing Piezoelectric Membrane Actuation For Microfluidic Systems', PhD Thesis, Southampton University, Department of Electronics and Computer Science, Southampton, England, 1997.

[Koch98a] M. Koch, N. Harris, A. G. R. Evans, N. M. White, A. Brunnschweiler, 'A novel micromachined pump based on thick-film piezoelectric actuation', Sensors and Actuators, Vol. A70, pp. 98-103, 1998.

[Koch98b] M. Koch, A. G. R. Evans, A. Brunnschweiler, 'The dynamic micropump driven with a screen printed PZT actuator', Journal of Micromechanics and Microengineering, Vol. 8, No. 2, pp. 119-122, 1998.

[Koch98c] M. Koch, D. Chatelain, A. G. R. Evans, A. Brunnschweiler, 'Two simple micromixers based on silicon', Journal of Micromechanics and Microengineering, Vol. 8, No. 2, pp. 123-126, 1998.

[Koch99] M. Koch, H. Witt, A. G. R. Evans, A. Brunnschweiler, 'Improved characterization technique for micromixers', Journal of Micromechanics and Microengineering, Vol. 9, No. 2, pp. 156-158, 1999.

[Koeh98] J. M. Koehler, U. Dillner, A. Mokansky, S. Poser, T. Schulz, 'Micro Channel Reactors for Fast Thermocycling', 2nd International Conference on Microreaction Technology, New Orleans, USA, pp. 241-247, 1998.

[Kohl94] F. Kohl, A. Jachimowicz, J. Steurer, R. Glatz, J. Kuttner, D. Biacovsky, F. Olacaytug, G. Urban, 'A micromachined flow sensor for liquid and gaseous fluids', Sensors and Actuators, Vol. A41-42, pp. 293-299, 1994.

[Kond99] S. Kondo, K. Kano, E. Shinohara, 'Reaction Chamber for PCR made by Microfabrication Technologies', Proceedings Transducers, Sendai, Japan, pp. 3P4.4, 1999.

[Kopp98] M. U. Kopp, A. J. deMello, A. Manz, 'Chemical Amplification: Continuous-Flow PCR on a Chip', Science, Vol. 280, pp. 1046-1048, 1998.

[Kova98] G. T. A. Kovacs, 'Micromachined Transducers – Sourcebook', McGraw-Hill, NY, USA, 1998.

[Krog00] J. P. Krog et al., 'Realization of a Prototype Industrial On-Line Sensing System for Ammonium Based on Micro System Technology: Results and Future Perspectives', Proceedings Micro Total Analysis Systems (μTAS), Enschede, The Netherlands, pp. 419-422, 2000.

[Laga00] E. T. Lagally, P. C. Simpson, R. A. Mathies, 'Monolithic integrated microfluidic amplification and capillary electrophoresis analysis system', Sensors and Actuators, Vol. B63, pp. 138-146, 2000.

[Lali00] T. Lalinsky, E. Burian, M. Drzik, S. Hascik, Z. Mozolova, J. Kuzmik, Z. Hatzopoulos, 'Performance of GaAs micromachined microactuator', Sensors and Actuators, Vol. A85, pp. 365-370, 2000.

[Lamm93] T. S. J. Lammerink, N. R. Tas, M. Elwenspoek, J. H. J. Fluitman, 'Micro-liquid flow sensor', Sensors and Actuators, Vol. A37-38, pp. 45-50, 1993.

[Lamm96] T. S. J. Lammerink, V. L. Spiering, M. Elwenspoek, A. van den Berg, 'Modular concept for fluid handling system', Proceedings IEEE Micro Electro Mechanical Systems, San Diego (CA), USA, pp. 389-394, 1996.

[Lang99] W. Lang, 'Reflexions on the future of microsystems', Sensors and Actuators, Vol. A72, pp. 1-15, 1999.

[Lao00] A. I. K. Lao, T. M. H. Lee, M. C. Carles, I.-M. Hsing, 'Thermal Management and Surface Passivation of a Miniaturized PCR Device for Traditional Chinese Medicine', Proceedings Micro Total Analysis Systems (μTAS), Enschede, The Netherlands, pp. 139-142, 2000.

[Lee93] L. G. Lee, C. R. Connell, W. Bloch, 'Allelic discrimination by nick-translation PCR with fluorogenic probes', Nucleic Acids Research, Vol. 21, No. 16, pp. 3761-3766, 1993.

[Lee99] S.-W. Lee, Y.-C. Tai, 'A micro cell lysis device', Sensors and Actuators A, Vol. 73, pp. 74-79, 1999.

[Lemo00] A. V. Lemoff, A. P. Lee, 'An AC Magnetohydrodynamic Microfluidic Switch', Proceedings Micro Total Analysis Systems (μTAS), Enschede, The Netherlands, pp. 571-574, 2000.

[Lemo99] A. V. Lemoff, A. P. Lee, R. R. Miles, C. F. McConaghy, 'An AC Magnetohydrodynamic Micropump: Towards a True Integrated Microfluidic System', Proceedings Transducers, Sendai, Japan, pp. 4C1.2, 1999.

[Leu97] T.-S. Leu, A.-M. Lanzillotto, M. Amabile, R. Wildes, 'Analysis of Fluidic and Mechanical Motion in MEMS by Using High Speed X-Ray Micro-Imaging Techniques', Proceedings Transducers, Chicago, USA, pp. 149-150, 1997.

[Li99] B. Li, B. Xiong, L. Jiang. Y. Zohar, M. Wong, 'Germanium as a Versatile Material for Low-Temperature Micromachining', Journal of Microelectromechanical Systems, Vol. 8, No. 4, pp. 366-372, 1999.

[Lin00a] Y.-C. Lin, M.-Y. Huang, K.-C. Young, T.-T. Chang, C.-Y. Wu, 'A rapid micro-polymerase chain reaction system for hepatitis C virus amplification', Sensors and Actuators, Vol. B71, pp. 2-8, 2000.

[Lin00b] Y.-C. Lin, C.-C. Yang, M.-Y. Huang, 'Simulation and experimental validation of micro polymerase chain reaction chips', Sensors and Actuators, Vol. B71, pp. 127-133, 2000.

[Lind00] H. van der Linden, W. Olthuis, P. Bergveld, 'Finding a good hydrogel composition for hydrogel based microvalves', Proceedings Micro Total Analysis Systems (μTAS), Enschede, The Netherlands, pp. 175-178, 2000.

[Linn98] R. Linnemann. P. Woias, C.-D. Senfft, J. A. Ditterich, 'A Self-Priming and Bubble-Tolerant Piezoelectric Silicon Micropump for Liquids and Gasses', Proceedings Micro Electro Mechanical Systems (MEMS), Heidelberg, Germany, pp. 532-537, 1998.

[Liu00] R. H. Liu, Q. Y. Yu, J. M. Bauer, B.-H. Jo, J. S. Moore, D. J. Beebe, 'In-Channel Processing to Create Autonomous Hydrogel Microvalves', Proceedings Micro Total Analysis Systems (μTAS), Enschede, The Netherlands, pp. 45-48, 2000.

[Maas97] R. Maas, M. Koch, N. R. Harris, N. M. White, A. G. R. Evans, "Thick-film printing of PZT onto silicon", Materials Letters, Vol. 31, pp. 109 – 112, 1997.

[Mado00] M. J. Madou, K.-Q. He, A. Shenderova, 'Fabrication of Artificial Muscle Based Valves for Controlled Drug Deleivery', Proceedings Micro Total Analysis Systems (μTAS), Enschede, The Netherlands, pp. 147-150, 2000.

[Malu00] N. Maluf, 'An Introduction to Microelectromechanical Systems Engineering', Artech House, Norwood, USA, 2000.

[Manz91] A. Manz, D. J. Harrison, J. C. Verpoorte, H. Ludi, H. M. Widmer, 'Integrated electroosmotic pumps and flow manifolds for total chemical analysis systems', Proceedings Transducers, San Francisco, USA, pp. 939-941, 1991.

[Manz97] A. Manz, H. Becker, 'Parallel Capillaries for High Throughput in Electrophoretic Separations and Electroosmotic Drug Discovery Systems', Proceedings Transducers, Chicago, USA, pp. 915-918, 1997.

[Menz97] W. Menz, J. Mohr, 'Mikrosystemtechnik fuer Ingenieure', VCH Verlagsgesellschaft, Weinheim, Germany, 1997.

[Morr98] T. B. Morrison, J. J. Weis, C. T. Wittwer, 'Quantification of low-copy transcripts by continous SYBR Green I monitoring during amplification', BioTechniques, Vol. 24, No. 6, pp. 954-962, 1998.

[Mull95] M. A. Mullins, A. F. P. van Putten, R. Bayford, J. B. Butcher, 'Potential for a smart sensor based on integrated silicon anemometer', Sensors and Actuators A, Vol. 46-47, pp. 342-348, 1995.

[Naga99] H. Nagai, Y. Murakami, E. Tamiya, 'Development of high integrated pico-liter PCR device', Proceedings Transducers, Sendai, Japan, pp. 3P4.3, 1999.

[Naza97] I. A. Nazarenko, S. K. Bhatnagar, R. J. Hohman, 'A closed tube format for amplification and detection of DNA based on energy transfer', Nucleic Acids Research, Vol. 25, No. 12, pp. 2516-2521, 1997.

[Nguy98] N. T. Nguyen, S. Schubert, S. Richter, W. Doetzel, 'Hybrid-assembled micro dosing system using silicon-based micropump/valve and mass flow sensor', Sensors and Actuators, Vol. A69, pp. 85-91, 1998.

[Nish94] T. Nishimoto, S. Shoji, M. Esashi, 'Buried piezoresistive sensor by means of MeV ion implantation', Sensors and Actuators, Vol. A43, pp. 249-253, 1994.

[Norl98] P. Norlin, O. Oehman, B. Ekstroem, L. Forssen, 'A chemical micro analysis system for the measurement of pressure, flow rate, temperature, conductivity, UV-absorption and fluorescence', Sensors and Actuators, Vol. B49, pp. 34-39, 1998.

[Nort93] M. A. Northrup, M. T. Ching, R. M. White, R. T. Watson, 'DNA Amplification with a Microfabricated Reaction Chamber', Proceedings Transducers, Yokohama, Japan, pp. 924-926, 1993.

[Nort95] M. A. Northrup, C. Gonzalez, D. Hadley, R. F. Hills, P. Landre, S. Lehew, R. Saiki, J. J. Sninsky, R. T. Watson, R. Watson Jr., 'A MEMS-Based Miniature DNA Analysis System', Proceedings Transducers, Stockholm, Sweden, pp. 764-767, 1995.

[Ogur94] M. Ogura, M. Mitsuhashi, 'Screening method for a large quantity of polymerase chain reaction products by measuring YOYO-1 fluorescence on 96-well polypropylene plates', Analytical Biochemistry, Vol. 218, pp. 458-459, 1994.

[Olss95] A. Olsson, P. Enoksson, G. Stemme, E. Stemme, 'A valveless planar pump isotropically etched in silicon', Proceedings Micromechanics Europe, Copenhagen, Denmark, pp. 120-123, 1995.

[Oost97] R. E. Oosterbroek, T. S. J. Lammerink, J. W. Berenschot, A. van den Berg, M. C. Elwenspoek, 'Designing, realization and characterization of a novel capacitive pressure/flow sensor', Proceedings Transducers, Chicago, USA, pp. 151-154, 1997.

[Oost99] R. E. Oosterbroek, T. S. J. Lammerink, J. W. Berenschot, G. J. M. Krijnen, M. C. Elwenspoek, A. van den Berg, 'A micromachined pressure/flow sensor', Sensors and Actuators, Vol. A77, pp. 167-177, 1999.

[Pali85] E. D. Palik editor, 'Handbook of Optical Constants of Solids', Academic Press, Orlando, USA, 1985.

[Pete79] K. E. Petersen 'Fabrication of an integrated planar silicon ink-jet structure', IEEE Trans. Electron Devices, ED-26, pp 1918-1920, 1979.

[Pol90] F. C. M. vande Pol, H. T. G. van Lintel, M. Elwenspoek, J. H. J. Fluitman, 'Thermopneumatic micropump based on micro-engineering techniques', Sensors and Actuators, Vol. A21, No. 1-3, pp. 198 – 202, 1990.

[Pose97] S. Poser, T. Schulz, U. Dillner, V. Baier, J. M. Koehler, D. Schimkat, G. Mayer, A. Siebert, 'Chip elements for fast thermocycling', Sensors and Actuators, Vol. A62, pp. 672-675, 1997.

[Pulf89] D. L. Pulfrey, N. G. Tarr, 'Introduction to Microelectronic Devices', Prentice-Hall, Englewood Cliffs, USA, 1989.

[Rapp94] R. Rapp, W. K. Schomburg, D. Maas, J. Schulz, W. Stark, 'LIGA micropump for gases and liquids', Sensors and Actuators, Vol. A40, pp. 57-61, 1994.

[Rasm98] R. Rasmussen, T. Morrison, M. Herrmann, C. Wittwer, 'Quantitative PCR by Continuous Fluorescence Monitoring of a Double Strand DNA Specific Binding Dye', Biochemica, No. 2, pp. 8-11, 1998.

[Rich91a] A. Richter, A. Plettner, K. A. Hofmann, H. Sandmaier, 'Electrohydrodynamic Pumping and Flow Measurement', Proceedings Transducers, San Francisco, USA, pp. 271-276, 1991.

[Rich91b] A. Richter, K. A. Hofmann, A. Plettner, H. Sandmaier, 'The Electrohydrodynamic Micro Flow Meter', Proceedings Transducers, San Francisco, USA, pp. 935-938, 1991.

[Rich97] M. Richter, A. Prak, J. Naundorf, M. Eberl, H. Leeuwis, P. Woias, A. Steckenborn, 'A Chemical Microanalysis System as a Microfluid System Demonstrator', Proceedings Transducers, Chicago, USA, pp. 303-306, 1997.

[Riri97] K. M. Ririe, R. P. Rasmussen, C. T. Wittwer, 'Product Differentiation by Analysis of DNA Melting Curves during Polymerase Chain Reaction', Analytical Biochemistry, Vol. 245, pp. 154-160, 1997.

[Rong99] W. Rong, R. Havsteen, U. D. Larsen, P. Telleman, 'Silicon and Polymer Microfabricated Devices for Flow-Injection Analysis of Sacharides', Proceedings Eurosensors, The Hague, The Netherlands, pp. 33-36, 1999.

[Sand91] H. Sandmaier, H. L. Offereins, K. Kuehl, W. Lang, 'Corner compensation techniques in anisotropic etching of (100)-silicon using aqueous KOH', Proceedings Transducers, San Francisco, USA, pp. 456-459, 1991.

[Sant99] J. T. Santini jr., R. Langer, M. J. Cima, 'A Microfabricated Controlled Release Device', Proceedings Transducers, Sendai, Japan, pp. 2P5.12, 1999.

[Scha00] C. G. J. Schabmueller, A. G. R. Evans, A. Brunnschweiler, G. J. Ensell, D. L. Leslie, M. A. Lee, 'Design, Fabrication and Packaging of Closed Chamber PCR-Chips for DNA Amplification', Proceedings of Design, Test, Integration, and Packaging of MEMS/MOEMS (DTIP), Paris, France, SPIE Proceedings Series Volume 4019, pp. 362-369, 2000.

[Scha01a] C. G. J. Schabmueller, M. Koch, M. E. Mokhtari, A. G. R. Evans, Brunnschweiler, H. Sehr, 'Mass-Producible, Bubble Tolerant Gas/Liquid Micropump with Self-Aligning Feature', accepted for publication at Micromechanics Europe (MME), Cork, Ireland, September 2001.

[Scha01b] C. G. J. Schabmueller, J. R. Pollard, A. G. R. Evans, J. S. Wilkinson, G. Ensell, A. Brunnschweiler, 'Integrated Diode Detector and Optical Fibres for In-Situ Detection within Micromachined Polymerase Chain Reaction Chips', Journal of Micromechanics and Microengeneering, Vol. 11, No. 4, pp. 329-333, 2001.

[Scha01c] J. Schaible, J. Vollmer, R. Zengerle, H. Sandmaier, T. Strobelt, 'Electrostatic microvalves in silicon with 2-way-function for industrial applications', Proceedings Transducers, Munich, Germany, 2001.

[Scha98] C. G. J. Schabmueller, M. Koch, A. G. R. Evans, A. Brunnschweiler, 'Micromachined chemical reaction system realized on a microfluidic circuitboard', Eurosensors XII, Vol. 1, Institute of Physic Publishing, Bristol, UK, pp. 571-574, 1998. Presented at Eurosensors XII, Southampton, United Kingdom, 1998.

[Scha99] C. G. J. Schabmueller, M. Koch, A. G. R. Evans, A. Brunnschweiler, 'Design and Fabrication of a Microfluidic Circuitboard', Journal of Micromechanics and Microengeneering, Vol. 9, No. 2, pp.176-179, 1999.

[Scho93] B. H. van der Schoot, S. Jeanneret, A. van den Berg, N. F. de Rooji, 'Modular setup for a miniaturized chemical analysis system', Sensors and Actuators, Vol. B15, pp. 211-213, 1993.

[Scho94] W. K. Schomburg, J. Vollmer, B. Buestgens, J. Fahrenberg, H. Hein, W. Menz, 'Microfluidic components in LIGA technique', Journal of Micromechanics and Microengineering, Vol. 4, No. 4, pp. 186-191, 1994.

[Seid90] H. Seidel, L. Csepregi, A. Heuberger, H. Baumgaertel, 'Anisotropic etching of crystalline silicon in alkaline solutions: I. Orientation dependence and behaviour of passivation layers', Journal of the Electochemical Society, Vol. 137, No. 11, pp. 3612-3626, 1990.

[Selv95] P. R. Selvin, 'Fluorescence Resonance Energy Transfer', Methods in Enzymology, Vol. 246, pp. 300-334, 1995.

[Shoj94] S. Shoji, M. Esashi, 'Microflow devices and systems', Journal of Micromechanics and Microengineering, Vol. 4, No. 4, pp. 157-171, 1994.

[Smit79] B. J. Smith, J. Stephen, 'Handbook of ion implantation data for silicon device fabrication', Atomic Energy Research Establishment, Harwell, Oxfordshire, England, 1979.

[Smit90] J. G. Smits, "Piezoelectric micropump with three valves working peristatically", Sensors and Actuators, Vol. A21-23, pp. 203 – 206, 1990.

[Steh96] M. Stehr, S. Messner, H. Sandmaier, R. Zengerle, 'A New Micropump with Bidirectional Fluid Transport and Selfblocking Effect', Proceedings Micro Electro Mechanical Systems (MEMS), San Diego, USA, pp. 485-490, 1996.

[Stem86] G. Stemme, 'A monolithic gas flow sensor with polyimide as thermal insulator, 'IEEE Transactions on Electron Devices, Vol. 33, No. 10, pp. 1470-1474, 1986.

[Stoe93] H. Stoecker, 'Taschenbuch der Physik', Verlag Harri Deutsch, Frankfurt am Main, Germany, 1993.

[Su96] Y. Su, A. G. R. Evans, A. Brunnschweiler, 'Micromachined silicon cantilever paddles with piezoresistive readout for flow sensing', Journal of Micromechanics and Microengineering, No. 6, pp. 69-72, 1996.

[Sved97] N. Svedin, E. Stemme, G. Stemme, 'A New Bi-Directional Gas-Flow Sensor Based on Lift Force', Proceedings Transducers, Chicago, USA, pp. 145-148, 1997.

[Sze81] S. M. Sze, 'Physics of Semiconductor Devices', 2nd edition, Wiley-Interscience Publication, New York, USA, 1981.

[Sze88] S. M. Sze, 'VLSI Technology', McGraw-Hill, Singapore, 1988.

[Terr79] S. C. Terry, J. H. Jerman, J. B. Angell 'A gas chromatographic air analyzer fabricated on a silicon wafer', IEEE Trans. Electron Devices, ED-26, pp. 1880-1886, 1979.

[Tuft62] O. N. Tufte, P. W. Chapman, D. Long, 'Silicon diffused-element piezoresistive diaphragms', Journal of Applied Physics, Vol. 33, pp. 3322-3327, 1962.

[Tyag96] S. Tyagi, F. R. Kramer, 'Molecular Beacons: Probes that Fluoresce upon Hybridization', Nature Biotechnology, Vol. 14, pp. 303-308, 1996.

[Urba99] G. Urban, 'Microstructuring of organic layers for microsystems', Sensors and Actuators, Vol. A74, pp. 219-224, 1999.

[Veen00] T. T. Veenstra, J. W. Berenschot, R. G. P. Sanders, J. G. E. Gardeniers, M. C. Elwenspoek, A. van den Berg, 'A Simple Selfpriming Bubble-Tolerant Peristaltic MicroPump', Proceedings Eurosensors, Copenhagen, Denmark, pp. 671-672, 2000.

[Weas89] R. C. Weast editor, 'Handbook of Chemistry and Physics', CRC Press, Boca Raton, Florida, USA, 69th edition, 1989.

[Whit99] D. Whitcombe, J. Theaker, S. P. Guy, T. Brown, S. Little, 'Detection of PCR products using self-probing amplicons and fluorescence', Nature Biotechnology, Vol. 17, pp. 804-807, 1999.

[Will78] A. F, W. Willoughby, 'Atomic diffusion in semiconductors', Rep. Prog. Phys., Vol. 41, pp. 1665-1705, 1978.

[Wils89] J. Wilson, 'Optoelectronics, An Introduction', Prentice Hall International, UK, 1989.

[Witt97] C. T. Wittwer, M. G. Herrmann, A. A. Moss, R. P. Rasmussen, 'Continuous fluorescence monitoring of rapid cycle DNA amplification', BioTechniques, Vol. 22, pp. 130-138, 1997.

[Wool96] A. T. Woolley, D. Hadley, P. Landre, A. deMello, R. Mathies, M. A. Northrup, 'Functional Integration of PCR Amplification and Capillary Electrophoresis in a Microfabricated DNA Analysis Device', Analytical Chemistry, Vol. 68, No. 23, pp. 4081-4086, 1996.

[Yang96] E. H. Yang, S. W. Han, S. S. Yang, 'Fabrication and testing of a pair of passive bivalvular microvalves composed of p+ diaphragms', Sensors and Actuators, Vol. A57, No. 1, pp. 75 – 78, 1996.

[Youn96] D. Young, 'Viral load quantitation: An integral part of future health management', Australasian Biotechnology, Vol. 6, No. 5, pp. 295-300, 1996.

[Yu00] H. Yu, P. Sethu, T. Chan, N. Kroutchinina, J. Blackwell, C. H. Mastrangelo, P. Grodzinski, 'A Miniaturized and Integrated Plastic Thermal Chemical Reactor for Genetic Analysis', Proceedings Micro Total Analysis Systems (μTAS), Enschede, The Netherlands, pp. 545-548, 2000.

[Zeng92] R. Zengerle, A. Richter, H. Sandmaier, 'A micro membrane pump with electrostatic actuation', Proceedings of IEEE Micro Electro Mechanical Systems '92, Travemuende, Germany, pp. 19 – 24, 1992.

[Zeng94] R. Zengerle, M. Richter, 'Simulation of microfluidic systems', Journal of Micromechanics and Microengineering, Vol. 4, No. 4, pp. 192-204, 1994.

[Zeng95] R. Zengerle, J. Ulrich, S. Kluge, M. Richter, A. Richter, 'Bidirectional silicon micropump', Sensors and Actuators, Vol. A50, pp. 81-86, 1995.

[Zhan96] G. Zhan, T. Lo, L. Liu, P. Tsien, 'A silicon membrane micropump with integrated bimetallic actuator', Chinese Journal of Electronics, Vol. 5, No. 2, pp. 29-35, 1996.